Development and investigation of novel models in computational medicine

Salma Chabbar

Université Mohammed V de Rabat

THESE DE DOCTORAT

Pour obtenir le grade de:

Docteur en sciences et techniques de l'ingénieur de l'école Mohammadia d'ingénieurs

Discipline: Mathématiques appliquées et informatique

Spécialité: Calcul scientifique et modélisation mathématique

Présentée par: Salma CHABBAR

Développement et investigation de nouveaux modèles en médecine computationnelle

---

Thèse dirigée par: Pr. Rajae ABOULAICH

présentée le 20 Septembre 2022

Devant le jury composé de:

Pr. Mounia El Kadiri	EMI, Rabat	Présidente
Pr. Soumaya Boujena	FSAC, Casablanca	Rapporteur
Pr. Rachid Ellaia	EMI, Rabat	Rapporteur
Pr. Vitaly Volpert	UCBL 1, Lyon	Rapporteur
Pr. Jean-Baptiste Caillau	UCA, Nice	Examinateur
Pr.Dr. Nabil Ismaili	UM6SS, Casablanca	Invité
Pr.Dr. Sanaa El Majjaoui	INO, Rabat	Invitée
Pr. Rajae Aboulaich	EMI, Rabat	Directrice de thèse
Pr. Abderrahmane Habbal	UCA, Nice	Co-directeur

Résumé

Dans cette thèse, notre objectif est de contribuer au développement d'outils d'aide à la décision dans le domaine de la santé, en nous basant sur la modélisation mathématique et la modélisation à base d'agents.
Les deux sujets auxquels nous nous intéressons dans ce travail, sont l'évolution du cancer et la propagation du coronavirus. Les deux phénomènes biologiques peuvent être modélisés par des équations différentielles d'une part et par les multi-agents d'autre part et la simulation numérique par les deux approches fournit des outils d'aide à la décision intéressants dans les deux cas.

Dans une première partie de ce mémoire, nous nous intéressons, à l'étude du développement d'une tumeur cancéreuse non encore traitée. Pour ce faire, deux différentes approches sont adoptées. Dans la première approche le suivi de l'évolution de la masse tumorale se fait au niveau macroscopique. La tumeur est modélisée en tant qu'amas de cellules disposant d'une densité et d'une forme évoluant suivant le développement de la tumeur. La modélisation utilisant un système d'équations aux dérivées partielles, nous permet dans ce cas de calculer les densités des différents types de cellules composant la tumeur et de simuler l'évolution de la forme de la tumeur. Le suivi du contour de la tumeur est fait à l'aide de la méthode des lignes de niveaux pour laquelle la vitesse normale est calculée de deux façons différentes. La première en utilisant la vitesse de Darcy pour transporter les valeurs de la fonction level-set et la deuxième en utilisant l'optimisation de forme pour calculer la vitesse de déformation en passant par un problème adjoint. La seconde approche se fait au niveau microscopique. Chaque cellule est modélisée individuellement en tant qu'agent en interaction continue avec son environnement ainsi qu'avec les autres cellules. La modélisation utilise dans ce cas la simulation multi-agents pour décrire le comportement des différents types de cellules ainsi qu'une équation aux dérivées partielles pour décrire la diffusion du nutriment dans leur environnement. Une étude de la sensibilité de ce modèle à chacun de ses paramètres est ensuite menée pour mieux analyser le modèle et le comprendre. Nous étudions par la suite le cas spécifique du cancer de la prostate sous traitements combinés d'hormonothérapie et curiethérapie à bas débit de dose. Nous utilisons un système d'équations aux dérivées partielles pour décrire le comportement des cellules de la prostate et leur réponse aux différents traitements. Les simulations numériques permettent de définir une stratégie thérapeutique pour combiner au mieux les effets des deux traitements sur la tumeur mais aussi sur la qualité de vie des patients qui se dégrade à cause des effets secondaires de chaque thérapie. Les résultats obtenus ont été discuté avec des oncologues. La résolution numérique des équations aux dérivées partielles est faite sous le logiciel FreeFem++ en utilisant la méthode des éléments finis. Dans le cas du modèle hybride de croissance tumorale, l'équation de diffusion du nutriment est résolue sous Matlab en utilisant la méthode des différences finies et reliée à Netlogo pour les simulations à base d'agents.

Dans la deuxième partie du travail, en utilisant la simulation multi-agents, nous avons simulé la propagation du Covid-19 à l'aide des modèles compartimentaux. Nous avons étudié l'impact de différentes mesures sanitaires sur l'évolution de la pandémie et mis en place un outil d'aide à la décision et de surveillance épidémiologique pour le suivi de la crise sanitaire engendrée par la maladie du Covid-19. Les simulations utilisant les multi-agents sont implémentées sous le logiciel Netlogo.

Mots clés: Croissance Tumorale; Prostate; Covid-19; Modèles EDP; Modèles Multi-agents.

Abstract

In this thesis, our objective is to contribute to the development of decision support tools in healthcare, through mathematical and agent-based modeling.
The two topics we are interested in in this work are the evolution of cancer and the spread of the coronavirus. Both biological phenomena can be modeled by differential equations on the one hand and by multi-agents on the other hand and the numerical simulation by both approaches provides interesting decision support tools in both cases.

In the first part of this thesis, we are interested in the study of the development of an untreated cancerous tumor. To do so, two different approaches are adopted. In the first approach, the evolution of the tumor mass is followed at the macroscopic level. The tumor is modeled as a cluster of cells evolving with time according to the development of the tumor. Modeling using a system of partial differential equations, allows us in this case to calculate the densities of the different cells composing the tumor as well as to simulate the tumor shape evolution. The tracking of the tumor contour is done using the level-set method for which the normal velocity is calculated in two different ways. The first one by using Darcy law to transport the level-set function values and the second one by using shape optimization to compute the deformation velocity through an adjoint problem. The second approach is at the microscopic level. Each cell is modeled individually as an agent in continuous interaction with its environment and with other cells. The modeling uses in this case multi-agent simulation to describe the behavior of the different types of cells and a partial differential equation to describe the diffusion of the nutrient in their environment. A study of the sensitivity of this model to each of its parameters is then conducted to better analyze and understand the hybrid model. We then study the specific case of prostate cancer under combined hormone therapy and low dose rate brachytherapy. We use a system of partial differential equations to describe the behavior of prostate cells and their response to different treatments. The findings were discussed with oncologists. Numerical simulations allow to define a treatment strategy to best combine the effects of the two treatments on the tumor but also on the quality of life of the patients, which deteriorates due to the side effects of each therapy. The numerical resolution of the partial differential equations is done under FreeFem++ software using a finite element method. In the case of the hybrid tumor growth model, the nutrient diffusion equation is solved in Matlab using a finite difference method and coupled to Netlogo for the agent-based simulations.

In the second part of the work, using multi-agent modeling, we simulated the spread of the coronavirus 2019 disease using compartmental models. We studied the impact of different sanitary measures on the evolution of the pandemic and implemented a decision support and epidemiological surveillance tool for the monitoring of the sanitary crisis caused by Covid-19. The multi-agent simulations are implemented under the Netlogo

software.

Key words: Tumor growth; Prostate; Covid-19; PDE models; Multi-agent models.

Contents

List of Figures

List of Tables

Chapter 1

Introduction

Biomathematics cover all the mathematical, numerical and computer science methods and tools dedicated to study and model biological phenomena. Biology offers an inexhaustible source of problems to model and mathematics provides a set of tools to help do so. In the present thesis, we aim to model two different phenomena. The first one is the development of cancerous tumors as one of the leading causes of death in the world according to the World Health Organization (WHO). The second is the spread of the coronavirus 19 disease that afflicted the world in late 2019. In this first introductory chapter, we present a state of the art of the two topics discussed in this thesis.

1.1 A state of the art in cancer modeling

Cancer is the world's second leading cause of death. Cancerous cells are able to ignore signals that usually instruct normal cells to stop dividing or to initiate the process of planned cell death, known as apoptosis, which the body uses to get rid of unneeded cells. As a result, the unhealthy cells grow out of control and begin to proliferate anarchically forming a solid malignant tumor [1]. In order to survive and multiply, the cancerous cells need enough nutrients to fuel their high rate of proliferation. As the tumor grows larger, the cells furthest from the supplies of nutrient stop proliferating and become quiescent in a dormant state where they reduce their nutrient requirements to survive the unfavorable environment. When the supply of nutrient are no longer sufficient for their survival, they die and become necrotic cells [2,3]. As the surrounding capillary network becomes insufficient for the development of the tumor, cancer cells induce the body to produce new blood vessels to directly supply the tumor in a process called angiogenesis. The tumor then evolves from the avascular stage to the vascular one [4–17]. The tumor tissue is thus composed of four types of cells: healthy cells, cancer cells, quiescent cells and dead cells. Different approaches are used in tumor growth modeling. Most models fall into three categories: continuum mathematical models for a macroscopic approach that consist of partial differential equations and ordinary differential equations where the tumor is regarded as a cell mass. Discrete cell population models for a microscopic approach that focuses on the cellular scale and introduce cell-cell interaction using agent-based modeling. The third category is a mixture of the previous two: a hybrid model combining agent-based modeling for the cell's simulation and PDE modelling of concentration or density fields. The continuum models are mostly reaction-diffusion-convection equations where the behavior and interaction of the cells, nutrients and other variables involved in tumor growth are described by a system of partial differential equations. This category

in itself contains two different types of models. In the first one the tumor is modeled as a cluster of different cell types whose growth is monitored through their respective densities [2, 18–21]. In the second type of continuous models, the tumor growth is modeled through the evolution of its nutrient's concentration [22–24]. The diffusion of the nutrient concentration within the tumor along with the expression of the pressure in the tumor tissue leads to a set of partial differential equations which describes the tumor free boundary mathematical model [25–27]. Being a complex phenomenon, tumor growth involves several parameters that usually prove to be difficult to collect. Therefore, tracking the tumor evolution in continuous modeling often leads to the resolution of inverse problems. The phenomenological parameters of the tumor are, in this case, recovered using experimental data and medical imaging [2, 28–30].
An alternative to continuum models for tumor growth modeling is discrete cell population models. In these models the cells form a system of autonomous decision-making agents interacting with their environment. The agents are subject to a set of rules derived from biology that address the tumor growth process [31–33]. One step further in agent-based modeling is to describe the agents environment through a continuum description. The resulting hybrid model allows the association of cell interactions and continuous models [34, 35]. The cells and their behavior are modeled using agent-based simulation while the nutrients evolution in the tumor environment is described using PDEs [36–39].
The purpose behind tumor growth research is to provide an improved theoretical basis for tumor growth control and therapeutic planning as pointed out by Benzekry et al. in [40]. Hence the importance of coupling tumor modeling with treatment options to study their effect and explore possible therapeutic strategies. There are different treatments for cancer such as chemotherapy [41, 42], radiation therapy [43, 44] or surgery for the removal of tumors at an early stage. These treatments can be used to treat all types of cancer. There is a third type of treatment that can only be used for hormone-sensitive cancers. Hormone therapy aims to block or at least inhibit the activity of hormones that act as a growth factor for some cancer cells. Prostate cancer is a hormone-sensitive cancer and also the second most commonly diagnosed male cancer [45]. For prostate cancer stimulation by androgen, the hormone responsible for regulating the development and maintenance of male features, is required for the survival and proliferation of both cancer and healthy prostate cells. Androgen deprivation therapy is a hormone therapy used in the treatment of prostate cancer that reduces the number of cancer cells by hindering androgen production in the prostate. However, in order to survive in an androgen- depleted environment a new mutation that affects the sensitivity to androgen occurs in the prostate cancer cells. The androgen-dependent cancer cells mutate into androgen-resistant cancer cells and they become able to maintain their growth in the unfavorable environment. Two types of cancer cells therefore characterize prostate cancer: hormone-sensitive cells and hormone-resistant ones [46].

In the next section, we introduce the second biomathematics application discussed in this thesis which is the modeling of the new coronavirus disease that emerged in late 2019.

1.2 Compartmental models for the simulation of Coronavirus 19

In November 2019, a disease caused by the coronavirus 2019 (Covid-19) appears for the first time in Wuhan, China, before spreading to the rest of the world. The virus spreads at an alarming rate and the first deaths soon start to be reported. In March 2020, WHO classifies it as a global pandemic and the governments of the different countries put in place sanitary measures to try to contain the pandemic. In this new worldwide context, mathematical modeling, through compartmental models, has played an important role in the epidemiological surveillance of this new virus and in public health policy decision-making. Compartmental models used in epidemiology divide the population into epidemiological classes according to the stage reached by the disease in an individual, and define the different rules that allow one individual to move from one class to another based on the characteristics of the disease under study. Each sub-population represents a compartment such that individuals from the same compartment share the same behavior. Compartmental models are usually studied using differential equations but they can also be analyzed using agent-based models.
Agent-based modeling helps to recreate and predict the evolution of complex phenomena through the simulation of the interactions between different autonomous agents. Since the Covid-19 outbreak, the multi-agent approach proved to be very useful in modeling the spread of the disease and studying the effect of the different measures taken by governments [47–50]. The SIR model is the reference model for Covid-19 modeling. The three compartment model divides the population into Susceptible, Infected and Recovered individuals and many papers have used this model to describe the evolution of Covid-19 [51–53]. By adjusting the parameters of the model, many case studies from different countries have been analyzed to provide valuable predictions on Covid-19 spread using the SIR model, such as Italy [52], China, South Korea, India, Australia, USA [51] and different European countries [54]. However, the SIR model, as pointed out by [55], despite providing reasonable forecast in the short term, does not accurately describe the evolution of the disease in the long term. With only three compartments, the SIR model does not fully describe the mechanisms of the Covid-19 disease. Covid-19 is characterized by an incubation period where the infected individual is not yet infectious and by the appearance of asymptomatic cases where the infected individual is infectious but does not exhibit any symptoms. Hence the relevance of adding two compartments to the basic SIR model to consider the incubation period and the asymptomatic cases. The compartment involving the individuals in the incubation period is often referred to as the Exposed or Latent compartment [56–59]. Covid-19 modeling helps analyzing the effects of different health measures and policies adopted by governments, whether it is vaccination [57], lockdown [56], social distancing [60] or restrictions on people' migration [59, 61, 62].

In the second chapter, a first tumor growth model that falls into the category of continuous models used in the macroscopic approach is presented. The model is based on the one presented by Lagaert J. B. in [2]. The evolution equations of the cell densities composing the tumor are established using conservation laws and the nutrient distribution in the tumoral tissue is modeled by a diffusion equation. The simulation of the tumor's boundary deformation leads to the resolution of a PDE-constrained optimization problem to recover the tumor shape. The partial differential equations system is solved using a finite element method in FreeFem++. The tracking of the tumor shape and boundary is

done through the level-set method, the challenge of this method lies in the construction of the normal velocity of the free boundary. The purpose of the second chapter is the comparison between two different methods of computing the level-set normal velocity with which the tumor will be deformed. The first one relies on using Darcy's law, the second draws the front velocity from the shape derivative of the tumor deformation.

In the third chapter, we present a simplified hybrid tumor growth model using multi-agent modeling and partial differential equations for a microscopic approach. The cell behavior is described using a multi-agent model in Netlogo where the nutrient is diffused through the agent environment using a continuous diffusion equation to determine whether the environment is conducive to cell survival and proliferation. We perform a sensitivity analysis of the hybrid model to its different parameters to better study the properties of tumor growth. The nutrient diffusion equation is solved using a finite difference method in Matlab and coupled to Netlogo for a hybrid modeling.

In the fourth chapter, we study the case of prostate cancer under combined hormone therapy and brachytherapy. The objective of the fourth chapter is to study the effectiveness of combining androgen deprivation therapy with brachytherapy in the treatment of prostate cancer using a system of partial differential equations that quantifies and tracks the evolution of the different densities of cells involved in prostate cancer and their response to treatments. We investigate different therapeutic strategies in combining the two treatments either by adjusting the treatment schedule of the hormone therapy or the radiation dose used in brachytherapy. The partial differential equations system is solved using a finite element method in FreeFem++ and the achieved results were discussed with oncologists.

In the fifth chapter, we develop an agent-based model based on the modified SLIAR compartmental model proposed by Arino J. et al. in [63] in order to simulate the spread of the Covid-19 pandemic in Morocco and explore different options for reducing the effective reproduction rate of the disease, the main indicator of the transmission dynamics of the virus. Our objective is to study the impact and the relevance of the sanitary measures taken by governments on the evolution of the pandemic. The software used for the simulations is the multi-agent programmable modeling environment Netlogo.

Scientific production

Publications

- Chabbar S., Aboulaich R., Habbal A., El Guarmah E.M., "Simulating tumor growth using mathematical and agent-based modeling", International Journal of Modeling, Simulation, and Scientific Computing, 2021.
- Chabbar S., Benmir M, El Karkri J., Bensaid K., Aboulaich R., Nejjari C., "Modeling and simulation of the evolution of the corona virus pandemic in a context of migration", Journal of Theoretical and Applied Information Technology, 99(2021).
- Chabbar S., Habbal A., Aboulaich R., Ismaili N., El Majjaoui S., "Combined hormone and brachy therapies for the treatment of prostate cancer", (Submitted in August 2022).

Communication in international conferences

- Chabbar S., Aboulaich R., Habbal A., "Mathematical modeling of the evolution of a cancerous tumor", MYRPAM 2019.
- Aboulaich R., Bensaid K., Chabbar S., El Karkri J., "Mathematical modeling and multi-agents approach for the evolution of the Coronavirus pandemic", IEEE ICT-MOD 2020.
- El Karkri J., Benmir M., Chabbar S., Aboulaich R., "A new Covid 19 multi-strain epidemiological model: analytical study and multi agent based simulations", CMES 2021.
- Benmir M., Chabbar S., Aboulaich R., Ismaili N., "Hybrid Model of Tumor Growth Under Chemotherapy Medicine", CARI 2022.

Chapter 2

Macroscopic tumor growth modeling and simulation

Abstract

In this chapter, we develop and implement a macroscopic approach for tumor growth modeling. We present a PDE model where the tumor is viewed as a cell mass and we use the level set method to track the tumor moving boundary. Our aim in this chapter is to compare two different method to compute the normal velocity of the level-set function. In one hand by using Darcy's law and on the other hand by using the shape optimization to draw the normal velocity of the free boundary. The numerical simulations are carried out on FreeFem++ using a 2D finite element method and the results of the two approaches are compared.

2.1 Introduction

Cells are the functional and structural biological unit of all living organisms. They divide and die in a regulated process that ensures the healthy functioning of the organ they belong to. For various reasons, a healthy cell may mutate into a cancerous one, thereby overriding the body's signals that would normally regulate its behavior. It then starts dividing in an uncontrolled and prolific way, resulting in a cancerous tumor mass as shown in Figure 2.1. The behavior of normal cells is therefore controlled by two mechanisms: the cell cycle, that results in the creation of new cells through their division, and apoptosis, the programmed cell death process that results in the destruction of old or damaged cells.

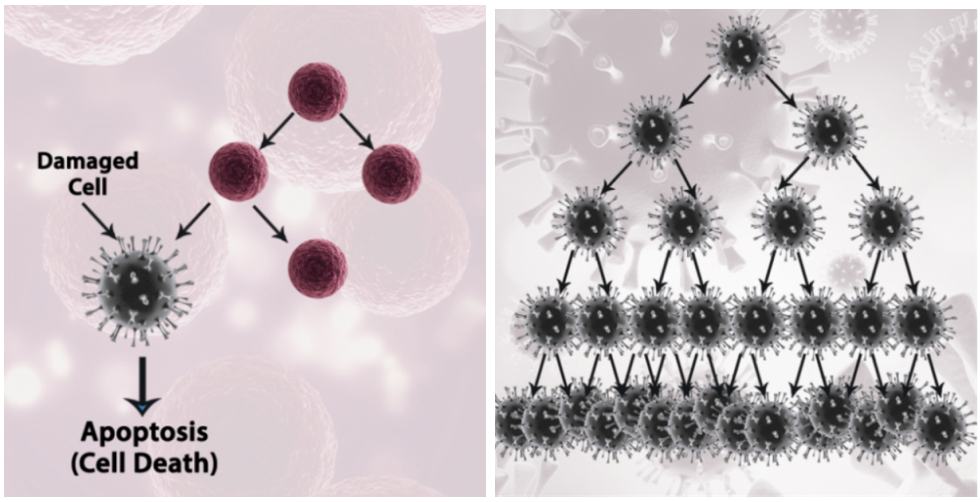

(a) Normal cell division (b) Cancer cell division

Figure 2.1: Cancer cell proliferation compared to the growth of healthy cells. Source: https ://drjockers.com/

The cell division cycle involves four phases:

- The first gap of growth (G_1) where the cell prepares to duplicate its DNA.
- The synthesis phase (S) where the cell's DNA is copied and replicated.
- The second growth phase (G_2) where the cell continues to grow and develop in preparation for division.
- The mitosis phase (M) where the cell divides into two new identical cells.

The phases G_1, S and G_2 are referred to as the interphase (I) as illustrated in Figure 2.2. The cells that are not proliferating are called quiescent cells, or cells in G_0 phase. The G_0 phase represents a resting phase where a cell in G_1 phase can transit when environmental conditions are not favorable. For instance, when the cell lacks the nutrients necessary for its multiplication [64].

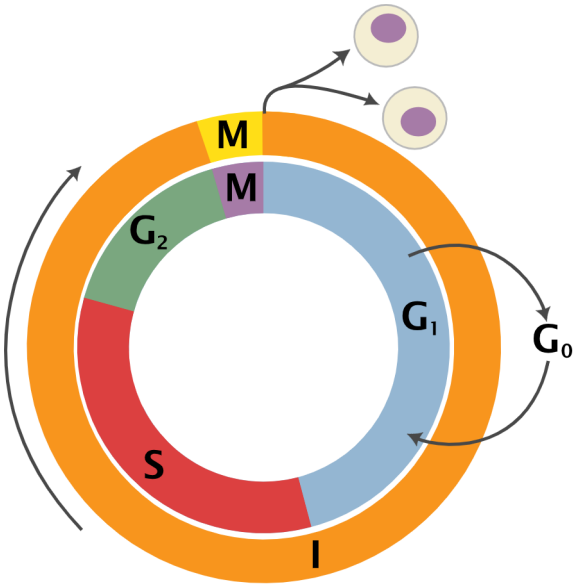

Figure 2.2: Cell cycle by Cell-Cycle-2.svg. Original uploader was Zephyris at en.wikipediaderivative work: Beaoderivative work: Histidine (talk) - Cell-Cycle-2.svg, CC BY-SA 3.0, https://commons.wikimedia.org/w/index.php?curid=12800954

Moreover, the cell cycle is regulated by checkpoints through which the cell ensures that the current process is proceeding properly. If an abnormality is identified, the cell will either initiate a corrective action or self-destruct (apoptosis). These abnormalities are genetic mutations that directly affect the DNA of the cell. If left unrepaired or undetected, they accumulate and lead to cancer [64].
The tumoral tissue is thus composed of healthy normal cells, cancer proliferative cells, quiescent cells and dead necrotic cells. In this chapter, the quiescent state is neglected. The tumor mass evolution is described through the evolution of the densities of the healthy, proliferative and necrotic cells and the cells depend on the oxygen supply to survive and multiply.

2.2 Mathematical modeling of tumor growth

The tumor growth is modeled with respect to two different levels. The first one is through the evolution of the cell densities within it. The second one is through the geometric progression of its contours.
This section develops on how these two approaches are mathematically modeled.

2.2.1 Evolution of cell densities

We consider the rescaled and nondimensionalised model proposed by Lagaert J. B. in [2] as follows :
Let $\Omega(t)$ be the tumor domain at a time t, $\mathbf{n}$ its outward normal, $[0, T]$ the time range and D a bounded domain containing the tumor.
The tumor consists of the proliferative, the necrotic and the healthy cells with their respective densities $P(x, y, t)$, $N(x, y, t)$ and $S(x, y, t)$.

The proliferative cells divide at a rate $\lambda_{mitosis}$ depending on the supply of oxygen concentration $C(x, y, t)$. Below an oxygen concentration threshold C_{thres}, the proliferative cells die at a rate μ_{death} and become necrotic cells.

$$\lambda_{mitosis}(C) = \frac{1 + \tanh(C - C_{thres})}{2}, \tag{2.1}$$

$$\mu_{death}(C) = \frac{1 - \tanh(C - C_{thres})}{2}, \tag{2.2}$$

The mitosis and death of the healthy cells are neglected since their frequency is much smaller than for the cancerous cells.
The cells are considered being incompressible, and therefore, at every point, the total quantity of mass, is conserved:

$$P + N + S = constant = 1, \tag{2.3}$$

In order to balance the mass variation due to mitosis and to keep the incompressibility of the medium, the cells move inside $\Omega(t)$ at a velocity $\mathbf{v}$. In the following we denote $\Omega(t)$ by Ω.

We can therefore write the conservation law for each density as follows on $\Omega \times [0, T]$:

$$\frac{\partial P}{\partial t} + \nabla \cdot (\mathbf{v}P) = \lambda_{mitosis}(C)P - \mu_{death}(C)P, \tag{2.4}$$

$$\frac{\partial N}{\partial t} + \nabla \cdot (\mathbf{v}N) = \mu_{death}(C)P, \tag{2.5}$$

$$\frac{\partial S}{\partial t} + \nabla \cdot (\mathbf{v}S) = 0, \tag{2.6}$$

Collecting "Eq. (2.4)", "Eq. (2.5)", "Eq. (2.6)" we obtain:

$$\nabla \cdot \mathbf{v} = \lambda_{mitosis}(C)P. \qquad on\ \Omega \times [0, T] \tag{2.7}$$

which illustrates the movement of the proliferative cells induced by mitosis.
We assume that the tissue has the structure of porous medium and we use Darcy's law as a closure equation for the velocity field of the mass balance equations [65]:

$$\mathbf{v} = -k\nabla\pi,$$

where the permeability coefficient k representing the cell mobility is assumed constant and equal to 1 as in [21] and π is the pressure in the tumor tissue:

$$\mathbf{v} = -\nabla\pi, \tag{2.8}$$

By combining "Eq. (2.7)" and "Eq. (2.8)" we can express the pressure equation :

$$-\Delta\pi = \lambda_{mitosis}(C)P, \qquad on\ \Omega \times [0, T] \tag{2.9}$$

We assume that the oxygen concentration $C(x, y, t)$ is consumed by the proliferative cells at rate μ_c and by the tissue at a rate μ. The oxygen diffusion equation is therefore written as follows on $\Omega \times [0, T]$:

$$\frac{\partial C}{\partial t} = \Delta C - \mu_c PC - \mu C. \tag{2.10}$$

Now, we summarize the model:

$$\begin{cases} -\Delta\pi = \lambda_{mitosis}(C)P, & on\ \Omega \times [0,T] \\ \partial_t P + \nabla \cdot (\mathbf{v}P) = \lambda_{mitosis}(C)P - \mu_{death}(C)P, & on\ \Omega \times [0,T] \\ \partial_t N + \nabla \cdot (\mathbf{v}N) = \mu_{death}(C)P, & on\ \Omega \times [0,T] \\ \partial_t C = \Delta C - \mu_c PC - \mu C. & on\ \Omega \times [0,T] \\ \\ \text{with boundary conditions :} \\ \partial_n \pi + \pi = 0, & on\ \partial\Omega \times [0,T] \\ C = C_0. & on\ \partial\Omega \times [0,T] \end{cases} \tag{2.11}$$

The boundary condition for C is derived from the observation that the outer medium $(D \setminus \Omega)$ is assumed to have a constant oxygen concentration. Moreover, initial conditions for P and N take into account that the outer medium $(D \setminus \Omega)$ is assumed to be healthy, thus containing neither proliferating nor necrotic cells.

The boundary condition on the pressure $\partial_n \pi + \pi = 0$ is derived from the assumption that the boundary moves proportionally to the pressure drop $\pi - \pi_0$ where π_0 is a constant external pressure :

$$\mathbf{v}.\mathbf{n} = -\nabla\pi.\mathbf{n} = \lambda(\pi - \pi_0).$$

We have taken $\pi_0 = 0$ and $\lambda = 1$ (λ accounts for the stiffness of the tumor/tissue interface).

2.2.2 Evolution of the tumor shape

In order to identify the tumor moving boundary, the following boundary identification criterion will be imposed on the pressure inside the tumor.
Assuming that the tumor is subjected to a constant external pressure π_0. The evolution of the tumor boundary is recovered by ensuring the continuity of the pressure π across its boundary $\partial\Omega$, hence by minimizing the following functional:

$$J(\Omega) = \int_{\partial\Omega} \frac{1}{2} (\pi - \pi_0)^2 \, ds \tag{2.12}$$

where π is solution of the PDE system "Eq. (2.11)".
Numerical experiments using this functional have proven to be unstable because of the difficulties in computing the normal vector to the boundary. To prevent this, and assuming that π remains equal to π_0 outside Ω we propose to use the following functional:

$$J(\Omega) = \int_{(D \setminus \Omega)} \frac{1}{2} (\pi - \pi_0)^2 \, ds \tag{2.13}$$

In order to minimize $J(\Omega)$ and capture the tumor shape, the level-set method as presented in the following section is used.

2.3 Numerical methodology and experiments

In this section, the level-set method is briefly presented in order to capture the shape of the tumor moving boundary as introduced by Sethian [66, 67].

2.3.1 Level-set method

The location of the tumor boundary $\Gamma(t) = \partial\Omega(t)$, at each time, is given by the zero-level set:

$$\Gamma(t) = \{x \mid \psi(x,t) = 0\} \tag{2.14}$$

where the level-set function ψ is defined as the signed distance to $\Gamma(t)$ as follows:

$$\begin{cases} \psi(x,t) < 0 \Longleftrightarrow x \in \Omega(t) \\ \psi(x,t) = 0 \Longleftrightarrow x \in \partial\Omega(t) \\ \psi(x,t) > 0 \Longleftrightarrow x \in (D \setminus \Omega(t)). \end{cases} \tag{2.15}$$

The outward normal $\mathbf{n}$ to the boundary of Ω is henceforth measured by:

$$\mathbf{n} = \frac{\nabla\psi}{\|\nabla\psi\|} \tag{2.16}$$

The initial location of tumor boundary $\psi(t=0)$ is known. The tumor boundary evolves, over time, with a normal velocity V.
The shape of the tumor is captured by transporting the values of the level-set function ψ by V:

$$\psi(t, x(t)) = 0 \quad \forall x(t) \in \partial\Omega(t) \tag{2.17}$$

Differentiating in t yields the evolution equation for the level-set function:

$$\frac{\partial\psi}{\partial t} + \mathbf{V} \cdot \nabla\psi = 0. \tag{2.18}$$

2.3.2 Level-set normal velocity evaluation

The shape of the tumor is identified through the minimization of $J(\Omega)$ and modeled by the zero-level-set of ψ. The challenge in this sub-section is the assessment of the normal velocity V with which the level-sets of ψ are moved.
Two different approaches are outlined in what follows for the normal velocity measurement.

First method: Darcy's law

The tumor deformation is due to the cells movement. The tumor tissue is a porous structure. The cells are in motion because of mitosis and death, which causes the deformation of the tumor boundary.
Darcy's law "Eq. (2.8)" gives the velocity characterizing this motion.
The normal velocity used in this case to move the tumor boundary is given by:

$$\mathbf{V} = (-\nabla\pi \cdot \mathbf{n}) \cdot \mathbf{n} \tag{2.19}$$

Second method: shape optimization

An implementation of the level-set method where the front velocity is computed using the shape derivatives of the classical shape optimization method is proposed in [68]. The shape derivative is computed through an adjoint-based approach and is used as the normal velocity of the free boundary. For more work on free boundary problems and shape optimization, we refer readers to [69] where a free boundary problem is transformed into a shape optimization one and the shape derivative of a cost functional is analyzed.

In this section, the tumor normal velocity is calculated using the same methodology proposed by Allaire G. et al. in [68]. The optimization problem is the combination of "Eq. (2.13)" and "Eq. (2.11)" :

$$\min_{\Omega} J(\Omega) = \int_{D \setminus \Omega} \frac{1}{2} (\pi - \pi_0)^2 \, ds \tag{2.20}$$

with π subject to the PDE system "Eq. (2.11)" over $\Omega \times [0, T]$:

$$\begin{cases} -\Delta \pi = \lambda_{mitosis}(C)P, \\ \partial_t P - \nabla \cdot (P \nabla \pi) = \lambda_{mitosis}(C)P - \mu_{death}(C)P, \\ \partial_t N - \nabla \cdot (N \nabla \pi) = \mu_{death}(C)P, \\ \partial_t C = \Delta C - \mu_c P C - \mu C. \end{cases} \tag{2.21}$$

• Method of Lagrange multipliers:

The Lagrangian L associated with the optimization problem is as follows:

$$\begin{aligned} L = J + \int_{\Omega} [\, & \phi_\pi(-\Delta \pi - \lambda_{mitosis}(C)P) + \phi_P(\partial_t P - \nabla \cdot (P \nabla \pi) - \lambda_{mitosis}(C)P + \mu_{death}(C)P) \\ & + \phi_N(\partial_t N - \nabla \cdot (N \nabla \pi) - \mu_{death}(C)P) + \phi_C(\partial_t C - \Delta C + \mu_c P C + \mu C) \,]. \end{aligned} \tag{2.22}$$

$\phi_\pi, \phi_P, \phi_N, \phi_C$ are the lagrange multipliers of π, P, N, C respectively. They represent the adjoint state.

Applying the generalized Green's formula and performing a semi-discretization of the time derivatives :

$$\begin{aligned} L = \int_{D \setminus \Omega} \frac{1}{2} (\pi - \pi_0)^2 \, ds + \int_{\Omega} [\, & \nabla \phi_\pi \cdot \nabla \pi - \phi_\pi \lambda_{mitosis}(C)P \\ & + \phi_P \frac{P - P^0}{dt} + P \nabla \phi_P \cdot \nabla \pi - \phi_P(\lambda_{mitosis}(C)P - \mu_{death}(C)P) \\ & + \phi_N \frac{N - N^0}{dt} + N \nabla \phi_N \cdot \nabla \pi - \phi_N \mu_{death}(C)P + \phi_C \frac{C - C^0}{dt} \\ & + \nabla \phi_C \cdot \nabla C + \phi_C(\mu_c P C + \mu C) \,]. \end{aligned} \tag{2.23}$$

By deriving L with respect to the state variables and writing the optimality conditions, we obtain the equations used to calculate the adjoint state.
The calculation of the directional derivative of L with respect to π in the direction φ yields the equation for ϕ_π as follows:

$$< \frac{\partial L}{\partial \pi}, \varphi >= \int_{D \setminus \Omega} (\pi - \pi_0)\varphi dx + \int_\Omega \nabla \phi_\pi \cdot \nabla \varphi + \int_\Omega P \nabla \phi_P \cdot \nabla \varphi + \int_\Omega N \nabla \phi_N \cdot \nabla \varphi = 0, \quad (2.24)$$

The calculation of the directional derivative of L with respect to P in the direction φ yields the equation for ϕ_P as follows:

$$< \frac{\partial L}{\partial P}, \varphi >= -\int_\Omega \lambda_{mitois}(C)\phi_\pi \varphi dx + \int_\Omega \phi_P \frac{\varphi}{dt} + \int_\Omega \varphi \nabla \phi_P \cdot \nabla \pi - \int_\Omega \phi_P(\lambda_{mitois}(C)\varphi - \mu_{death}(C)\varphi)dx - \int_\Omega \phi_N \mu_{death}(C)\varphi + \int_\Omega \mu_c \phi_C \varphi C dx = 0, \quad (2.25)$$

The calculation of the directional derivative of L with respect to N in the direction φ yields the equation for ϕ_N as follows:

$$< \frac{\partial L}{\partial N}, \varphi >= \int_\Omega \phi_N \frac{\varphi}{dt} + \int_\Omega \varphi \nabla \phi_N \cdot \nabla \pi = 0, \quad (2.26)$$

The calculation of the directional derivative of L with respect to C in the direction φ yields the equation for ϕ_C as follows:

$$< \frac{\partial L}{\partial C}, \varphi >= -\int_\Omega \phi_\pi \lambda'_{mitosis}(C)P\varphi dx - \int_\Omega \phi_P(\lambda'_{mitosis}(C)P\varphi - \mu'_{death}(C)P\varphi)dx - \int_\Omega \phi_N \mu'_{death}(C)P\varphi + \int_\Omega \phi_C \frac{\varphi}{dt} dx + \int_\Omega \nabla \phi_C \cdot \nabla \varphi + \int_\Omega \phi_C \mu_c P\varphi + \int_\Omega \phi_C \mu \varphi = 0. \quad (2.27)$$

• Shape derivative computation:

In order to apply a gradient method to our minimization problem, we follow the same methodology proposed in [68]. We consider domains of the following type:

$$\Omega_\theta = (Id + \theta)(\Omega). \quad \text{with} \quad \theta \in W^{1,\infty}(\mathbb{R}^d, \mathbb{R}^d) \quad (2.28)$$

Definition 1. *The shape derivative of $J(\Omega)$ at Ω is defined as the Fréchet derivative in $W^{1,\infty}(\mathbb{R}^d, \mathbb{R}^d)$ at 0 of the application $\theta \longrightarrow J((Id + \theta)(\Omega))$, i.e.*

$$J((Id + \theta)(\Omega)) = J(\Omega) + J'(\Omega)(\theta) + \circ(\theta). \quad \textit{with } lim_{\theta \to 0} \frac{|\circ(\theta)|}{\|\theta\|} = 0,$$

where $J'(\Omega)$ is a continuous linear form on $W^{1,\infty}(\mathbb{R}^d, \mathbb{R}^d)$.

In the following, we give two lemmas from [68] used for the computation of the shape derivative of the functional J.

Lemma 1. *Let Ω be a smooth bounded open set and $f(x) \in W^{1,1}(\mathbb{R}^d)$. Define $J(\Omega) = \int_\Omega f(x)dx$.*
Then J is differentiable at Ω and

$$J'(\Omega)(\theta) = \int_\Omega div(\theta(x)f(x))dx = \int_{\partial\Omega} \theta(x) \cdot n(x)f(x)ds.$$

for any $\theta \in W^{1,\infty}(\mathbb{R}^d, \mathbb{R}^d)$

Lemma 2. *Let Ω be a smooth bounded open set and $f(x) \in W^{2,1}(\mathbb{R}^d)$. Define $J(\Omega) = \int_{\partial\Omega} f(x)ds$.*
Then J is differentiable at Ω and

$$J'(\Omega)(\theta) = \int_{\partial\Omega} \theta \cdot n \left(\frac{\partial f}{\partial n} + Hf\right) ds$$

for any $\theta \in W^{1,\infty}(\mathbb{R}^d, \mathbb{R}^d)$, where H is the mean curvature of $\partial\Omega$ defined by $H = divn$.

The shape derivative is obtained by differentiating

$$J(\Omega) = L(\Omega, \pi(\Omega), P(\Omega), N(\Omega), C(\Omega), \phi_\pi(\Omega), \phi_P(\Omega), \phi_N(\Omega), \phi_C(\Omega)) \tag{2.29}$$

which, by the chain rule theorem, reduces to the partial derivative of L with respect to Ω in the direction θ:

$$J'(\Omega)(\theta) = \frac{\partial L}{\partial \Omega}(\Omega, \pi(\Omega), P(\Omega), N(\Omega), C(\Omega), \phi_\pi(\Omega), \phi_P(\Omega), \phi_N(\Omega), \phi_C(\Omega))(\theta). \tag{2.30}$$

Applying Lemma 1 and 2, the shape derivative is computed as follows :

$$\begin{aligned} J'(\Omega)(\theta) = \int_{\partial\Omega} [&-\frac{1}{2}(\pi - \pi_0)^2 ds + \nabla\phi_\pi \cdot \nabla\pi - \phi_\pi \lambda_{mitosis}(C)P \\ &+ \phi_P \frac{P - P^0}{dt} + P\nabla\phi_P \cdot \nabla\pi - \phi_P(\lambda_{mitosis}(C)P - \mu_{death}(C)P) \\ &+ \phi_N \frac{N - N^0}{dt} + N\nabla\phi_N \cdot \nabla\pi - \phi_N \mu_{death}(C)P + \phi_C \frac{C - C^0}{dt} \\ &+ \nabla\phi_C \cdot \nabla C + \phi_C(\mu_c PC + \mu C)]\theta \cdot n. \end{aligned} \tag{2.31}$$

The shape derivative is written as follows:

$$J'(\Omega)(\theta) = \int_{\partial\Omega} \nu\, \theta \cdot n$$

Ignoring smoothness issues [68], the descent direction is chosen as the vector field $\theta = -\nu \cdot \mathbf{n}$.
The shape Ω is then updated as:

$$\Omega_\rho = (Id + \rho\theta)(\Omega). \tag{2.32}$$

where $\rho > 0$ is a small descent step. Therefore:

$$J(\Omega_\rho) = J(\Omega) - \rho \int_{\partial\Omega} \nu^2 ds + \bigcirc(\rho^2). \tag{2.33}$$

which guarantees the decrease of the objective function.

• Level-set normal velocity :

To sum up, the shape derivative accounting for the tumor deformation is defined as follows:

$$J'(\Omega)(\theta) = \int_{\partial\Omega} \nu\, \theta \cdot \mathbf{n}. \tag{2.34}$$

The tumor deformation is done along the descent direction: $\theta = -\nu \cdot \mathbf{n}$.
The normal velocity used in this case to move the tumor boundary is the normal component of the descent direction θ.

$$\mathbf{V} = (\theta \cdot \mathbf{n}) \cdot \mathbf{n} = -\nu \cdot \mathbf{n}. \tag{2.35}$$

2.3.3 Algorithm

In light of the above, the following algorithm summarizes all the steps discussed throughout this chapter.

Initialization of the level-set ψ
Initialization of the state (π, P, N, C)
In case of method 2 : Initialization of the adjoint state $(\phi_\pi, \phi_P, \phi_N, \phi_C)$
Computation of the initial cost function J
Computation of the initial advection velocity $\mathbf{V}$
For $iter = 1$ to $iter_{max}$ **do** *(Loop for the time range)*
  While $J > threshold$ **do** *(Loop for the minimization)*
    Solve the level set equation
    Solve the state problem
    In case of method 2 : Solve the adjoint problem
    Computation of J
  end While
  Update of the level set
  Update of the state
  In case of method 2: Update of the adjoint state
end For

2.3.4 Numerical method

The level-set equation, the state problem and the adjoint system (method 2) are solved using the general purpose finite element package FreeFem++ [70, 71].

Level-set function

The level-set function is solved, at each time iteration k, using the characteristic Galerkin method function predefined on FreeFem++ for convection operators.
To keep the level-set equation numerically stable and regularize it, it is periodically reinitialized as in [67, 68] by solving:

$$\begin{cases} \partial_t \psi + sign(\psi_0)(\mid \nabla \psi \mid -1) = 0 & in \quad D \times [0,T] \\ \psi(t=0,x) = \psi_0(x). & in \quad D \end{cases} \tag{2.36}$$

where the *sign* function is defined as follows [67]:

$$sign(\psi_0) = \frac{\psi_0}{\sqrt{\psi_0^2 + h^2}} \tag{2.37}$$

and h is the size of the mesh used to discretize the problem.

State system

In order to solve the state problem (2.11) on FreeFem++, we need to write the weak formulation for each state variable. We consider the discretization in time:

$$t_0 = 0; t_1 = t_0 + dt = dt; ...; t_k = kdt; ...; t_K = Kdt = T.$$

We used an implicit scheme for the discretization in time of the problem. The system (2.21) is therefore discretized in time as follows:

$$\begin{cases} -\Delta \pi^{k+1} = \lambda_{mitosis}(C^k)P^k, \\ \frac{P^{k+1}-P^k}{dt} - \nabla \cdot (P^{k+1}\nabla \pi^{k+1}) = \lambda_{mitosis}(C^k)P^{k+1} - \mu_{death}(C^k)P^{k+1}, \\ \frac{N^{k+1}-N^k}{dt} - \nabla \cdot (N^{k+1}\nabla \pi^{k+1}) = \mu_{death}(C^k)P^{k+1}, \\ \frac{C^{k+1}-C^k}{dt} = \Delta C^{k+1} - \mu_c P^{k+1}C^{k+1} - \mu C^{k+1}. \end{cases} \tag{2.38}$$

In the following we denote $\Omega(t_k)$ by Ω. The weak formulations of the state problem are as follows:

$$\begin{cases} \text{Find} \quad \pi^{k+1} \in H^1(\Omega) \quad \text{such that} \quad \forall \varphi \in H^1(\Omega) \\ \int_\Omega \nabla \pi^{k+1} \nabla \varphi + \int_{\partial\Omega} \pi^{k+1}\varphi - \int_\Omega \lambda_{mitosis}(C^k)P^k = 0, \end{cases} \tag{2.39}$$

$$\begin{cases} \text{Find} \quad P^{k+1} \in H_0^1(\Omega) \quad \text{such that} \quad \forall \varphi \in H_0^1(\Omega) \\ \int_\Omega \frac{P^{k+1}-P^k}{dt}\varphi + \int_\Omega P^{k+1}\nabla \pi^{k+1} \cdot \nabla \varphi + \int_{\partial\Omega} P^{k+1}\pi^{k+1}\varphi - \int_\Omega \lambda_{mitosis}(C^k)P^{k+1}\varphi \\ + \int_\Omega \mu_{death}(C^k)P^{k+1}\varphi = 0, \end{cases} \tag{2.40}$$

$$\begin{cases} \text{Find} \quad N^{k+1} \in H_0^1(\Omega) \quad \text{such that} \quad \forall \varphi \in H_0^1(\Omega) \\ \int_\Omega \frac{N^{k+1}-N^k}{dt}\varphi + \int_\Omega N^{k+1}\nabla \pi^{k+1} \cdot \nabla \varphi + \int_{\partial\Omega} P^{k+1}\pi^{k+1}\varphi - \int_\Omega \mu_{death}(C^k)P^{k+1}\varphi = 0, \end{cases} \tag{2.41}$$

$$\begin{cases} \text{Find} \quad C^{k+1} \in H^1(\Omega) \quad \text{such that} \quad \forall \varphi \in H_0^1(\Omega) \\ \int_\Omega \frac{C^{k+1}-C^k}{dt}\varphi + \int_\Omega \nabla C^{k+1} \cdot \nabla \varphi + \int_\Omega \mu_c P^{k+1}C^{k+1}\varphi + \int_\Omega \mu C^{k+1}\varphi = 0. \end{cases} \tag{2.42}$$

Adjoint system

We recover the weak formulations of the adjoint state from Eq. (2.24) - (2.27).

$$\begin{cases} \text{Find} \quad \phi_\pi^{k+1} \in H^1(\Omega) \quad \text{such that} \quad \forall \varphi \in H^1(\Omega) \\ \int_{D \setminus \Omega} (\pi^{k+1} - \pi_0)\varphi dx + \int_\Omega \nabla \phi_\pi^{k+1} \cdot \nabla \varphi + \int_\Omega P^{k+1} \nabla \phi_P^k \cdot \nabla \varphi + \int_\Omega N^{k+1} \nabla \phi_N^k \cdot \nabla \varphi = 0, \end{cases} \tag{2.43}$$

$$\begin{cases} \text{Find} \quad \phi_P^{k+1} \in H_0^1(\Omega) \quad \text{such that} \quad \forall \varphi \in H_0^1(\Omega) \\ -\int_\Omega \lambda_{mitois}(C^{k+1})\phi_\pi^{k+1}\varphi dx + \int_\Omega \phi_P^{k+1}\frac{\varphi}{dt} + \int_\Omega \varphi \nabla \phi_P^{k+1} \cdot \nabla \pi^{k+1} - \int_\Omega \phi_P^{k+1}(\lambda_{mitois}(C^{k+1})\varphi \\ -\mu_{death}(C^{k+1})\varphi)dx - \int_\Omega \phi_N^k \mu_{death}(C^{k+1})\varphi + \int_\Omega \mu_c \phi_C^k \varphi C^{k+1} dx = 0, \end{cases} \tag{2.44}$$

$$\begin{cases} \text{Find} \quad \phi_N^{k+1} \in H_0^1(\Omega) \quad \text{such that} \quad \forall \varphi \in H_0^1(\Omega) \\ \int_\Omega \phi_N^{k+1}\frac{\varphi}{dt} + \int_\Omega \varphi \nabla \phi_N^{k+1} \cdot \nabla \pi^{k+1} = 0, \end{cases} \tag{2.45}$$

$$\begin{cases} \text{Find} \quad \phi_C^{k+1} \in H^1(\Omega) \quad \text{such that} \quad \forall \varphi \in H_0^1(\Omega) \\ -\int_\Omega \phi_\pi^{k+1}\lambda'_{mitosis}(C^{k+1})P^{k+1}\varphi dx - \int_\Omega \phi_P^{k+1}(\lambda'_{mitosis}(C^{k+1})P^{k+1}\varphi - \mu'_{death}(C^{k+1})P^{k+1}\varphi)dx \\ -\int_\Omega \phi_N^{k+1}\mu'_{death}(C^{k+1})P^{k+1}\varphi + \int_\Omega \phi_C^{k+1}\frac{\varphi}{dt}dx + \int_\Omega \nabla \phi_C^{k+1} \cdot \nabla \varphi + \int_\Omega \phi_C^{k+1}\mu_c P^{k+1}\varphi \\ +\int_\Omega \phi_C^{k+1}\mu\varphi = 0. \end{cases} \tag{2.46}$$

Results

The numerical results are shown in Fig. 2.3. and Fig. 2.4 and the numerical values of the parameters are given in the Table 2.1.

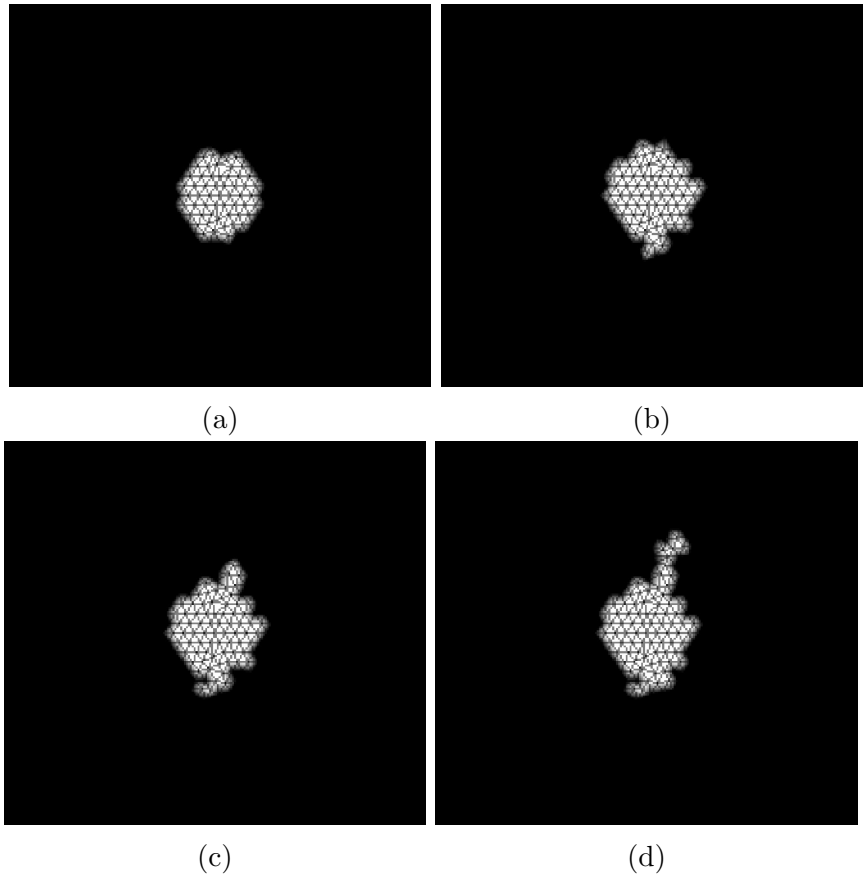

Figure 2.3: Tumor growth evolution using Darcy's law to compute the front velocity

The simulation results for the two velocity calculation methods differ in these three aspects:

- The tumor volume evolution is different: slight volume evolution can be observed in the first method Fig. 2.3. versus a more important one in the second Fig. 2.4.
- The shape optimization method takes substantially more computational time. On 2.2 GHz intel Core i7-8750H with 16 Go of Ram, one iteration of the algorithm needs:
  a) 17s of CPU time for the first method.
  b) 60s of CPU time for the shape optimization method.
- The deformation for an initial spherical shape of the tumor is different: the tumor is distorted in the first case but keeps its spherical shape in the second.

The second method is time-consuming and the tumor keeps its spherical shape because of the shape optimization. Whereas, Darcy's law helps reduce 3.5 times the processing duration and the tumor boundary evolution is more realistic.

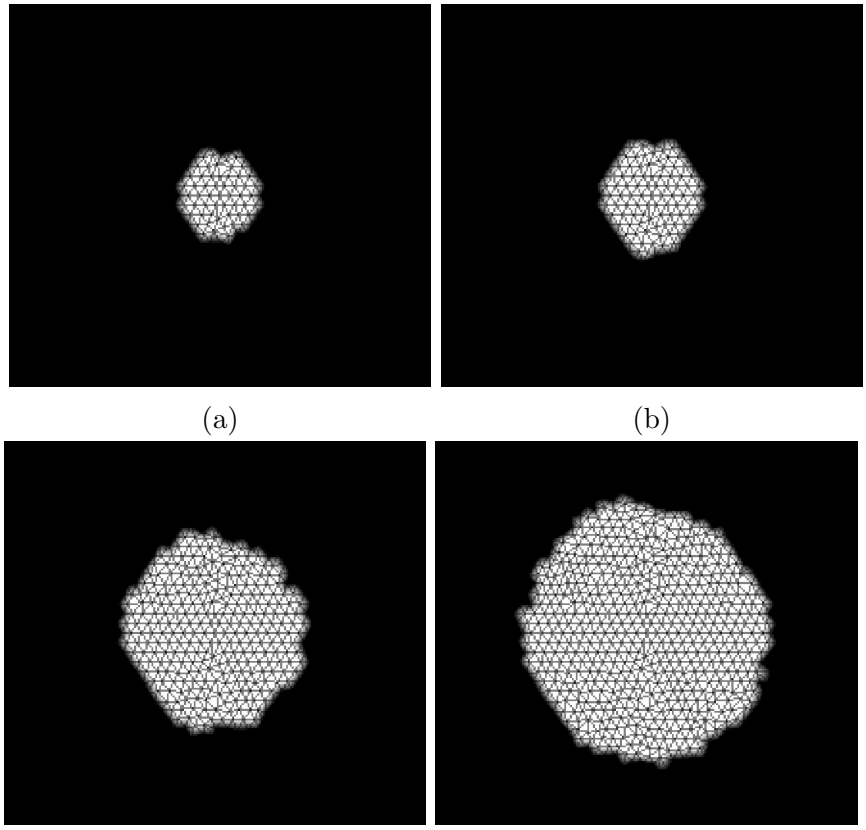

Figure 2.4: Tumor growth evolution using shape optimization to compute the front velocity

Table 2.1: Tumor growth macroscopic model parameters values.

μ_c	μ	π_0	C_{thres}	C_0
0.05	0.1	0	0.3	0.11

2.4 Conclusion

In this chapter, a macroscopic study of tumor growth was performed. The tumor progression was monitored through the evolution of the different cell densities composing it and also through the evolution of its contour using two different approaches to assess the tumor's deformation velocity. The results of the two velocity assessments were compared and even though the tumor evolution using Darcy's law seems more realistic and helps shorting the execution's time, the validation of the achieved results cannot be concluded from a biological standpoint. The macroscopic model is based on theoretical mathematical parameters that do not necessarily have a straightforward interpretation in the clinical field, besides, it overlooks the cell's behavior and interactions at the cellular scale.

For the two approaches presented in this chapter, the one related to Darcy's compares to a previously published work by Sethian and al. referenced in [67]. The tumor boundary is tracked using the level set method where the normal velocity matches Darcy's on

the tumor boundary. However, the tumor is modeled through the nutrient concentration in the medium and not through the cell densities. The results show that according to the type of vascularization the shape of the tumor evolves differently: in low vascularization regime, the shape of the tumor is distorted while it keeps its spherical shape in a high vascularization regime. To our knowledge, there are no publications related to the shape optimization approach in a setting close enough to ours to allow comparative study.

In the next chapter, a microscopic approach using agent-based modeling is presented. A discrete cell population model where the cell's behavior is described using agent-based modeling is combined with a PDE to describe the operating environment of the cells. The resulting hybrid model takes into consideration cellular interactions for a microscopic modeling of tumor growth.

Chapter 3

Hybrid ABM/PDE tumor growth modeling and simulation

Abstract

In this chapter, we develop and implement a microscopic approach which focuses on the cellular scale of tumor growth. A hybrid model using agent-based modeling for the cell behavior and a PDE for the description of the tumor environment is presented. A sensitivity analysis is performed on the hybrid model for a better understanding of its impact on the tumor growth. Agent-based numerical simulations are provided on Netlogo and coupled with Matlab for the resolution of the diffusion equation of the nutrient in the cell environment.

3.1 Introduction

Agent-based models are used to simulate the actions and interactions of autonomous agents in order to study and understand the behavior of a complex system. The agents are the active entities that interact with the system of interest. In agent-based modeling, the first step is to identify the entities that are relevant to the system and then to define their behavior. The connections between the agents are then established through rules that govern their behavior. The system dynamics then emerge from the interactions between the individual behaviors of the agents. In tumor growth modeling, agent-based models are used for a cellular modeling of the tumor's behavior [31–33]. For example, healthy cells and cancerous cells can be modeled as opposing teams of agents as modeled by Brown M. et al. in [72] or the cell behavior can be modeled using artificial neural networks as done by Gerlee P. et al. in [73].
In this chapter, a simplified hybrid model for tumor growth that combine discrete cell population models with a continuous description of the cell's environment is presented. The governing rules for cell behavior are modeled using Netlogo: a programming language and modeling environment for agent-based systems. The oxygen diffusion in the cell environment is done through a diffusion equation and solved using a finite difference method with Matlab. The communication between Matlab and Netlogo is ensured by an interface in Netlogo which allows the exchange of data between the two programs.

3.2 Hybrid modeling of tumor growth

The tumoral tissue is composed of four different types of cells. Normal cells which are healthy cells, proliferating cancer cells that appear as a result of a mutation in a healthy cell or following the proliferation of a cancerous cell, quiescent cancer cells that are proliferating cells in a dormant state due to the lack of oxygen and the dead necrotic cells. In the following section the Netlogo environment where the cells evolve is described along with the biological rules which dictate the cells behavior.

3.2.1 Agent-based model

The tumor environment $\Omega(t)$ in Netlogo is modeled as a square grid divided into patches where the agents move: $\Omega = \bigcup_k Patch_k$. The tumor's evolution is monitored within a time range [0,T].
The agents are the tumor cells. Three different cell states are defined: the healthy state (S), the proliferative cancerous state (P) and the quiescent cancerous one (Q). The necrotic dead cells are automatically removed. The oxygen is diffused through Ω, each $Patch_k$ has its own oxygen concentration level C_k^t.
The cells move in the patches and interact in accordance with biological criteria that govern the tumor's evolution.
The biological set of rules governing the agents -the cells- actions are derived from biological considerations in order to replicate the tumor microscopic features and are listed in the paragraph below.

Cellular automata rules

The model features three types of cells, the healthy the proliferative and the quiescent cells. The movement of the cells is defined by two parameters: the direction the cell is facing which is a number greater than or equal to 0 and less than 360 (0 is north, 90 is east, and so on) and the step ds by which the cells advance. At each time iteration, two random numbers p_1 and p_2 in $[0, 1]$ are generated and the following rules are applied to each cell:

- Contact inhibition enables healthy cells to cease proliferation and growth when they contact each other. Therefore, a healthy cell inspects its surrounding to assess the distance between it and the other cells. If there is a risk of collision, the healthy cell moves in the opposite direction to the cell it is likely to collide with. Otherwise, the healthy cell moves in a random direction and can multiply if the mitosis condition is met.

- A healthy cell is a normal cell that can divide with a propability λ_S if there is enough oxygen and space in the patch and $p_1 < \lambda_S$.

- Healthy cells mitosis spawns a new healthy cell with the same characteristics including its location.

- A healthy cell can mutate into a proliferating cell with a probability $P_{Mutation}$ if $p_2 < P_{Mutation}$.
  Its mitosis propability then increases to emphasize the uncontrolled proliferation of cancer cells.

- Proliferative cells mitosis spawns a new proliferative cell regardless of contact inhibition.

- Each of the healthy and proliferating cells consume a level of oxygen $C_{S,P}$ in order to survive and proliferate. When the level of oxygen in the patch is insufficient for the survival of the cell:

  a) If it is a healthy cell: the cell dies and it will be destroyed.

  b) If it is a proliferative cell: the cell becomes quiescent, in a dormant state, and its oxygen requirement is reduced to enable it to survive in the unfavorable environment $C_Q < C_{S,P}$.

- A quiescent cell can revert to being proliferative if the environment becomes favorable again.

- A cell that remains quiescent for more than $dtmax$ iterations in a row will die of necrosis and will be destroyed.

The oxygen concentration in the patches is a determining factor in the cell's behavior and thus in the tumor's growth.
Supplying oxygen to the tumor environment and diffusing it through the patches is done using a diffusion equation as presented in the following section.

3.2.2 Oxygen diffusion equation

The equation for the diffusion of the oxygen concentration is based on the nutrient diffusion equation as proposed by Friedman A. et al. in [26].

$$\begin{cases} \partial_t C - \Delta C = \alpha(C_B - C) - \alpha_{cons} C & in \quad \Omega \times [0,T] \\ \partial_n C = 0 & in \quad \partial\Omega \times [0,T] \\ C(t=0,x,y) = C_0(x,y). & in \quad \Omega \end{cases} \tag{3.1}$$

where C_B is the oxygen concentration in the vascular system, $\alpha(C_B - C)$ is the rate of oxygen concentration supplied by the vascular system and α_{cons} is the consumption rate of oxygen by the cells, which depends on the cell type.

3.2.3 Hybrid Model

The hybrid model makes use of the results of the oxygen diffusion equation in the agent-based model defined through the cellular automata rules.
The model runs as follows :

- The first step is the initialization of the model on Netlogo:
  a) N healthy cells are created in the environment.
  b) Each $Patch_k$ is supplied with its initial oxygen concentration C_k^0.
  c) A specific $Patch_B$ is selected to hold the blood vessel supplying oxygen to the environment.
- At each time iteration t :
  a) The oxygen concentrations C_k^t are collected from the patches and sent to Matlab as the initial condition.
  b) $\partial_t C - \Delta C = 0$ is solved in Matlab using a finite difference method.
  c) The new oxygen concentrations level C_k^{t+1} are sent back to NETLOGO and redistributed to the patches.
  d) The environment is supplied with oxygen (C_B) from the vascular system through $Patch_B$.
  e) The cells interact with their environment according to the cellular automata rules.
  f) The oxygen level in each patch is reduced by the amount of oxygen consumed by the cells ($\alpha_{cons} C$) : depending on the cell type, $C_{S,P}$ or C_Q will be subtracted for every living cell.

3.2.4 Simulation and results

For the simulations, the healthy cells are in a light gray tone, the proliferative cells are in a darker gray and the quiescent ones are black. In order to follow the evolution of the oxygen level in the patches, the background color of the patches will vary according to their oxygen level. Each patch will have a shade of gray proportional to its oxygen concentration. The extremes being white (patch full of oxygen) and black (no more oxygen

in the patch). The numerical results are shown in Fig. 3.1.

Initialization :

- 700 Healthy light gray cells (S) are created
- $P_{Mutation} = 0.01$
- $\lambda_S = 0.001$
- The environment is full of oxygen (Background color is White)

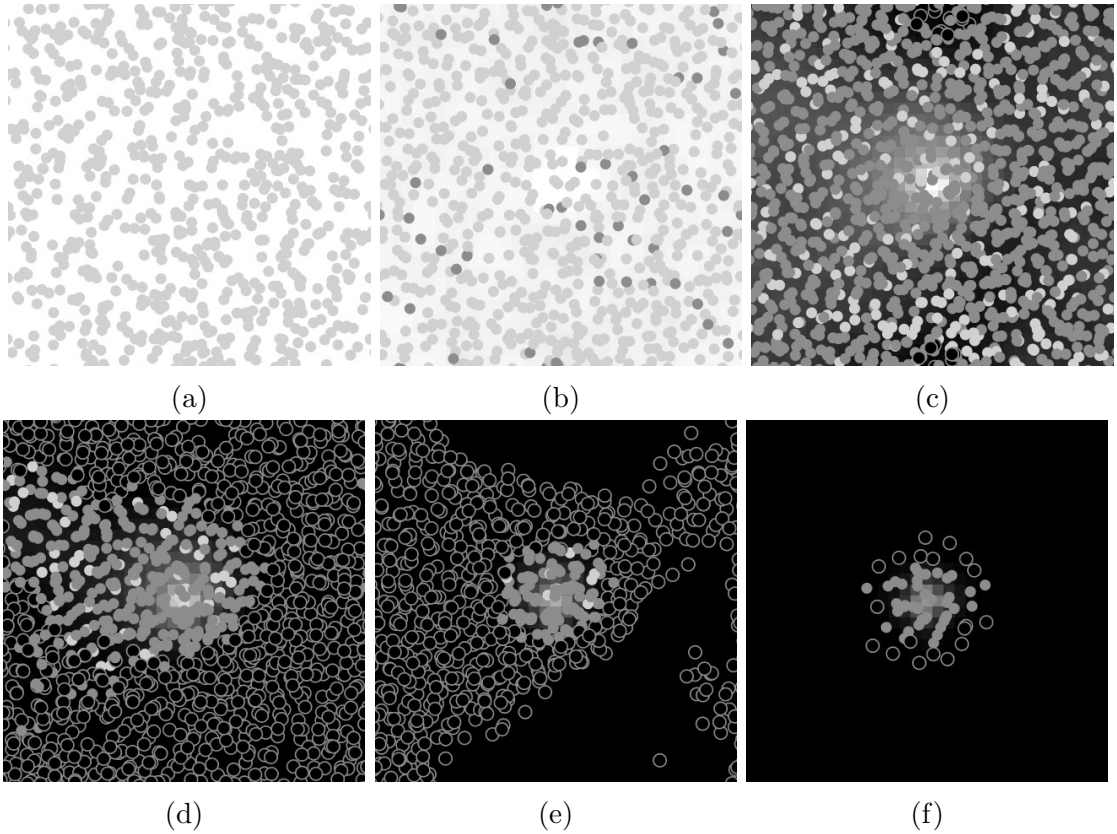

Figure 3.1: Tumor development using the hybrid model.

In Fig. 3.1(a), the population consists of healthy cells. The emergence of the proliferating cells is observed in Fig. 3.1(b). As the total number of cells increases, the background color of the patches begins to darken as the oxygen levels decreases. Quiescent cells therefore appear in the patches where the oxygen level is extremely low. The $Patch_B$ supplying the tumor with oxygen is then clearly visible on Fig. 3.1(c) with a white background color.
The quiescent cells die and are removed after being deprived of oxygen for too long as shown in Fig. 3.1(e).
Cancer cells gather around the oxygen source to survive and multiply Fig. 3.1(f). Those furthest from the oxygen source enter a quiescent state and will eventually die if the environment remains unfavorable.

To further analyze the tumor hybrid model's dynamics, a sensitivity analysis of the model is conducted in the following section.

3.3 Sensitivity analysis of the hybrid model

In this section, the sensitivity of the hybrid model to each of its parameters is discussed. For each parameter, three different scenarios are studied. The parameter of interest varies from one scenario to another while the other parameters remain unchanged. Each scenario represents the summary of 20 identical simulations.

First parameter: Initial number of cells

The first input of the model to be studied is the initial number of healthy cells introduced in the environment. The three scenarios are from different initial population of 700, 1000 and 2000 cells.
By increasing the initial number of cells, the decay of the oxygen supply in each patch is faster. The patches reach a level of oxygen insufficient to ensure the survival of the cells at a higher speed and necrosis of quiescent cells occur at an earlier stage of the simulation (see Fig. 3.2).
The tumor is faster to develop around the remaining source of oxygen and the shape of the tumor -as portrayed in Fig. 3.1(f) emerges faster.
As the number of initial cells increases:

- The emergence of quiescent cells occurs earlier: $t = 98$ iterations for the 700 initial-cells, $t = 81$ iterations for 1000 initial-cells and $t = 41$ iterations for 2000 initial-cells.
- The tumor reaches its final shape faster with fewer cells: After 160 iterations for the first scenario, 125 iterations for the second and 80 iterations for the last one.

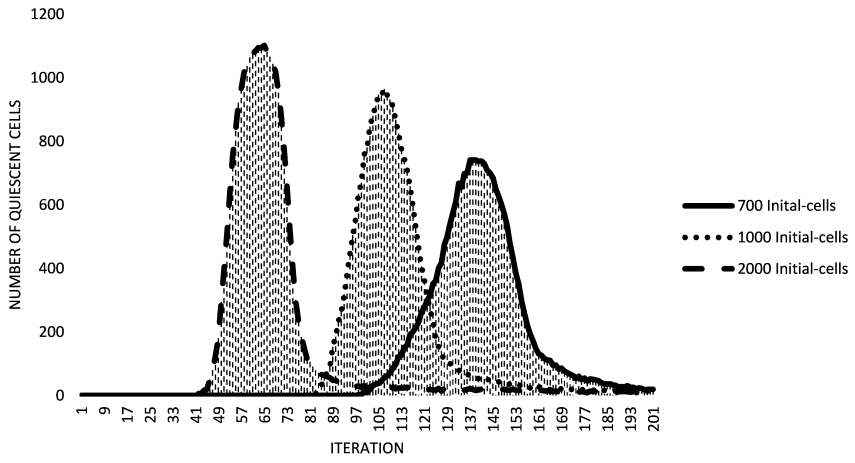

Figure 3.2: Time range of quiescent cells appearance and death.

Second parameter: Running time of the simulations T

The time range for each simulation is $[0, T]$. The first scenario summarizes the results of 20 simulations run with $T = 200$ iterations, the second with $T = 300$ iterations and the third $T = 400$ iterations.
By increasing the running time of the simulations, the surface area occupied by the tumor increases as well while the cell number does not vary as much (see Table 3.1.).

Table 3.1: Tumor surface area and number of cells for each scenario of T.

T (Iterations)	Tumor surface area (cm^2)	STD (cm^2)	Variation (%)	Cell Number	STD	Variation (%)
200	9.99	1.26	-	66	6	-
300	15.17	1.41	+51.8	59	4	-10.6
400	18.63	2	+22.8	62	5	+5.1

Since the other parameters, namely the initial number of cells, the mitosis propability and the mutation probability, remain the same for the three scenarios, the overall number of cells in the final volume of the tumor remain slightly unchanged, they rather tend to spread out more as the simulation time extends (see Fig. 3.3).
Therefore, in the absence of clinical treatment, the space occupied by the tumor increases over time.

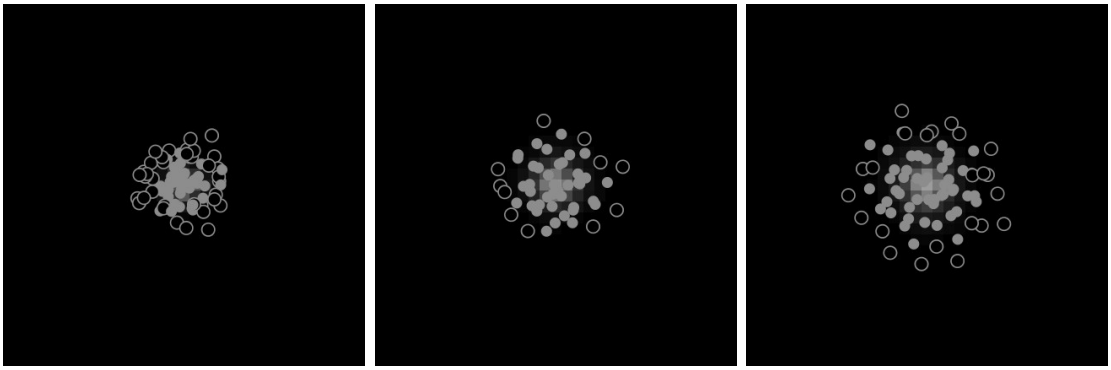

(a) T = 200 iterations (b) T = 300 iterations (c) T = 400 iterations

Figure 3.3: Evolution of the surface occupied by the tumor over time.

Third parameter: Mitosis propability λ_S

The mitosis propability λ_S controls how fast the cells can divide. In order to monitor its impact on the tumor growth, three scenarii with three different λ_S are considered.

Each scenario being the synthesis of 20 simulations with the same λ_S. $\lambda_S = 0.001$, $\lambda_S = 0.005$ and $\lambda_S = 0.01$.
By increasing λ_S, the cells divide more often, thus the tumor cell number increases as well. However, the surface area occupied by the tumor decreases in the same proportion (see Table 3.2.).

Table 3.2: Tumor occupied surface area and final number of cells for each scenario of λ_S.

λ_S	Tumor surface area (cm^2)	STD (cm^2)	Variation (%)	Cell Number	STD	Variation (%)
0.001	15.03	1.98	-	59	5	-
0.005	5.02	0.66	-66.6	96	6	+62.7
0.01	3.43	0.24	-31.6	127	11	+32.3

With a larger number of cells, the competition for the oxygen resource becomes stronger. Therefore, the cells cluster around the oxygen source and shape a thicker tumor (see Fig. 3.4.) which causes the tumor volume to shrink.

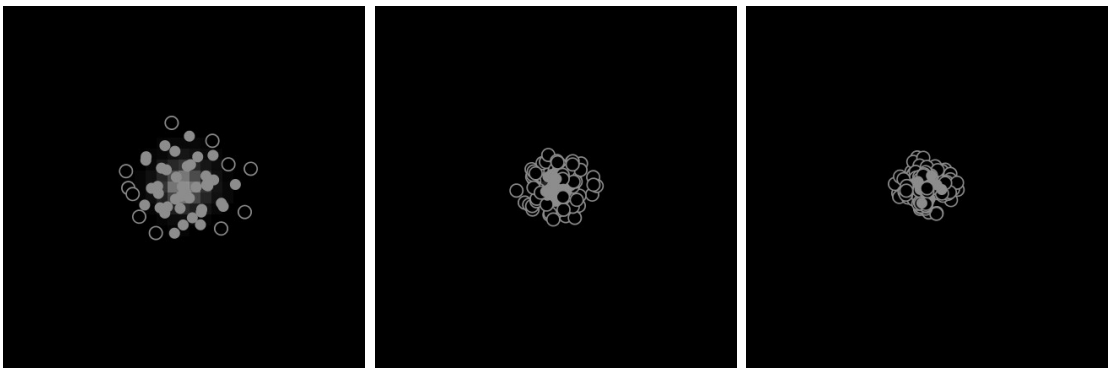

(a) $\lambda_S = 0.001$ (b) $\lambda_S = 0.005$ (c) $\lambda_S = 0.01$

Figure 3.4: Tumor final shape evolution with different mitosis probabilities.

Fourth parameter: Mutation Probability $P_{Mutation}$

The mutation probability $P_{Mutation}$ controls the inclination of the healthy cells to mutate into cancer cells. In order to focus primarily on the effect of the mutation probability on the tumor growth, the cells mitosis are neglected.
The first scenario consolidates the results of 20 simulations run with $P_{Mutation} = 0.001$, the second one using $P_{Mutation} = 0.005$ and the third one with $P_{Mutation} = 0.01$.

By increasing the mutation probability, the tumor volume decreases while the total cell number does not vary much (see Table 3.3.). However, the cell distribution among the different cell types differs from one scenario to another (see Table 3.4.).

Table 3.3: Tumor surface area and total cell number for each scenario of $P_{Mutation}$.

$P_{Mutation}$	Tumor Surface area (cm^2)	STD (cm^2)	Variation (%)	Cell Number	STD	Variation (%)
0.001	34.07	4.13	-	45	2	-
0.005	25.37	1.96	-25.5	48	2	+6.7
0.01	23.15	0.85	-8.8	47	1	-2.1

Table 3.4: Cell type distribution in (%) for each scenario of $P_{Mutation}$.

$P_{Mutation}$	S	STD	P	STD	Q	STD
0.001	50.7	5.1	32.7	4.2	16.6	4.7
0.005	13.8	4.8	64.1	6.1	22.1	4.1
0.01	2.6	1.7	76.6	5.1	20.8	4.5

As the mutation rate increases, the number of proliferating cells increases while the number of healthy cells decreases. With the highest $P_{Mutation}$ in the third scenario, the proliferating cells prevail in the tumor structure with 77% of the total number of cells, while the healthy cells predominate in the first scenario with 51% of the total number of cells (Table 3.4.).
As the proportion of proliferating cells increases in the tumor, the cancer cells tend to rally around the oxygen source causing the tumor to decrease in size (Fig. 3.5.).

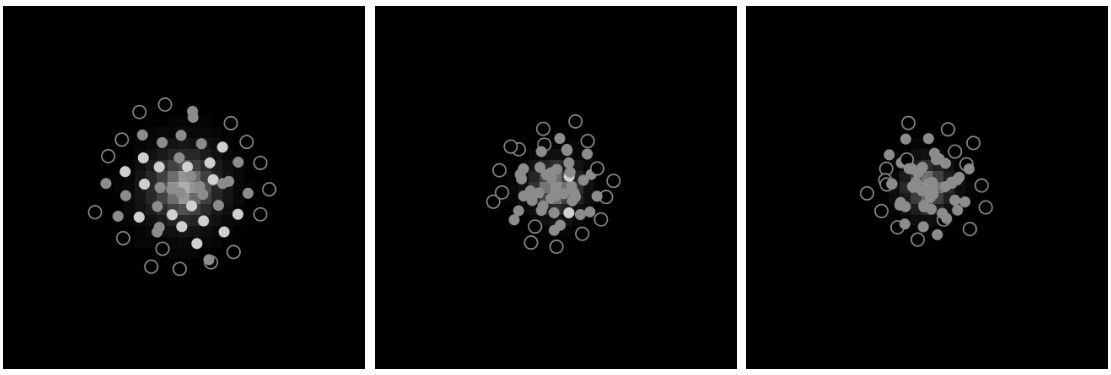

(a) $P_{Mutation} = 0.001$ (b) $P_{Mutation} = 0.005$ (c) $P_{Mutation} = 0.01$

Figure 3.5: Tumor final shape evolution with different mutation probabilities.

Conclusion of the sensitivity analysis

Cancer cells are characterized by an uncontrolled proliferation resulting from mutations occurring within the cell. The tumor density is greatly affected by the intensity of the proliferation: the greater the cell mitosis, the thicker the resulting tumor. Whereas, the tumor volume is affected by the occurrence of mutations as well as the passage of time for an untreated tumor.

3.4 Conclusion

The hybrid approach presented in this chapter allows a closer tumor growth monitoring and enables the tracking of the evolution of both the tumor shape and its components. The sensitivity analysis of the hybrid model allowed us to study the effect of the cell proliferation rate and mutation probability on the tumor development. The simulations showed that without treatment, the tumor expands over time and as the rate of cell divisions and mutations increase, the tumor's cancer cell population increases, resulting in a more compact tumor. By combining the oxygen diffusion equation with the agent-based model the resulting simulations are more easily assimilated by physicians, hence the interest of using hybrid modeling for biological phenomena.

Our hybrid model results compare to the paper by Yangjin Kim et al., referenced in [36], that also investigates the cellular component of a hybrid cell-based-PDE model for tumor growth. The necrotic cells are not removed compared to our model and the oxygen consumption is modeled differently (using Michaelis-Menten kinetics) but the results also show a similar tumor structure and clusters of proliferating cells in oxygen-rich regions.

Both the macroscopic and microscopic approaches show that without treatment the tumor volume increases with time. The purpose behind tumor growth research either by using continuous or discrete modeling, is to provide an improved theoretical basis for tumor growth control and therapeutic planning.
In the next chapter, we study the case of prostate cancer under combined treatments of hormone therapy and internal radiotherapy and investigate different therapeutical strategies for its treatment.

Chapter 4

Tumor growth modeling: Case of prostate cancer under treatment

Abstract

Prostate cancer is a hormone-dependent cancer characterized by two types of cancer cells, androgen-dependent cancer cells and androgen-resistant ones. The objective of this chapter is to present a novel mathematical model for the treatment of prostate cancer under combined hormone therapy and brachytherapy. Using a system of partial differential equations, we quantify and study the evolution of the different cell densities involved in prostate cancer and their responses to the two treatments. Numerical simulations of tumor growth under different therapeutic strategies are explored and presented. The numerical simulations are carried out on FreeFem++ using a 2D finite element method.

4.1 Introduction

The latest statistics published by the International Agency for Research on Cancer show that in 2018, 18.1 million new cancer cases have been identified and 9.6 million deaths have been recorded worldwide making it the second leading cause of death globally [45]. Prostate cancer ranks third in incidence with 1.28 million cases and represents the second most commonly diagnosed male cancer [45].

Prostate cells need the hormone androgen to survive and function properly. For this to happen, the androgens have to bind to a protein in the prostate cells called Androgen Receptor and activate it [74, 80–82, 84]. Since androgens act as a growth factor for the cells, one way of treating prostate cancer is through the antihormone therapy that hinder its activity. The Androgen Deprivation Therapy (ADT) aims to either reduce androgen production or to stop the androgens form working through the use of drugs. However, over time, castration-resistant cells that are able to sustain growth in a low androgen environment emerge. The castration-resistant cells can either be androgen independent or androgen repressed meaning that they have a negative growth rate when the androgen is abundant in the prostate [46, 75, 82, 94, 95]. In order to delay the development of castration-resistance and reduce its occurrence, the Intermittent Androgen Deprivation Therapy is used. In this case, the antihormone therapy is given in cycles by alternating drug administrations and rest periods. Switching between the different periods is done according to the level of the Prostate Specific Antigen (PSA), a protein produced by prostate cells and present in small quantities in the serum of men with healthy prostates [76, 82, 84] .

Several studies have compared the continuous ADT with the intermittent one, and all have concluded that with the continuous ADT, the patient will eventually relapse due to the emergence and proliferation of the castration-resistant prostate cancer cell. In [82], conditions that favor intermittent therapy over continuous treatment in terms of delaying the emergence of castration resistance or eventually achieving remission have been established. In [84], while continuous ADT leads to treatment failure in finite time, the effectiveness of the intermittent treatment depends on the characteristics of the castration-resistant cancer cells and the scheduling of the therapy with the possibility of a scenario where the tumor volume can be bounded. While in [74] the treatment response depends on the competitive interaction between the androgen-dependent and the castration-resistant cancer cells. In the case where the androgen-dependent cells had a competitive advantage over the castration-resistant ones, the intermittent scheduling yielded better results than the continuous treatment. Otherwise, the intermittent ADT resulted in an earlier treatment failure. In addition to the risk of relapse, the androgen deprivation therapy causes some side effects that affect greatly the quality of life of the patient [46, 79]. Combining the ADT with another type of treatment may prove to be more effective and less harmful to the patient.

The brachytherapy is an effective radiation therapy used in the treatment of prostate cancer by placing a sealed radiation source inside the prostate gland [77, 78, 87]. It can be delivered in high dose rates (HDR) or low dose rates (LDR) depending on the radioactive source used and the duration of treatment. In the HDR brachytherapy the source is placed temporarily in the prostate for a few minutes to deliver high dose radiation while for the LDR brachytherapy low radiations dose are delivered from radioactive sources permanently placed in the prostate. The radioactivity of the source decays over time, therefore its presence in the prostate does not cause any long-term concern as its ra-

dioactivity disappears eventually [83,86]. In the present chapter, the LDR brachytherapy is investigated for the treatment of prostate cancer using the Iodine-125 as a decaying radioactive source.
In practice, brachytherapy is prescribed either as monotherapy, often for localized tumors, or combined with another therapy such as external beam radiation therapy for which the total dose prescribed is divided between internal and external radiation. Brachytherapy can also be prescribed in combination with hormone therapy. However, in the existing literature there is currently no mathematical model that explores this combination of treatments. The objective of the current chapter is to develop a mathematical model to assess the effectiveness of combining androgen deprivation therapy with brachytherapy in the treatment of prostate cancer. The resulting simulations can be used to explore potential therapeutic strategies.
In the following section, we introduce the therapeutic protocols of the two treatments considered for prostate cancer from a biological point of view before moving on to their mathematical modeling.

4.2 Treatment protocol for prostate cancer

We present here some anatomical, biological and medical notions that are useful for the understanding of our model.

4.2.1 Hormone therapy

Hormone therapy is often prescribed for advanced metastatic cases of prostate cancer. It is a treatment used for cancers where hormones play an important role in the proliferation of cancer cells. In the case of prostate cancer, the hormone involved is androgen. Most androgens are made by the testicles, but the adrenal glands, located above the kidneys, are also responsible for producing some androgens. For androgens to act as a prostate cell growth factor, they need to bind to a protein in the cells called the androgen receptor and activate it. Therefore, there are two ways to prevent prostate cancer cells from accessing androgen: either by directly reducing androgen production or by preventing available androgens from binding to the androgen receptors and thus preventing them from functioning. Androgen deprivation therapy relies on these two principles to treat prostate cancer through the use of drugs. To better understand the mechanism of this therapy, it is necessary to first understand how androgens are produced.

Androgen production

The production of testosterone, the main androgen in the body, follows a complex process that involves several steps as well as other hormones. It is carried out in cascades. The first key element is the Luteinizing hormone-releasing hormone (LHRH), a hormone produced by neurons in the part of the brain called the hypothalamus. The LHRH stimulates the pituitary gland, a small gland of 7 to 8 mm in diameter that is located at the base of the brain. The pituitary gland in response secretes the Luteinizing Hormone (LH). The LH then stimulate the testicles which will then produce testosterone. The process of androgen production is illustrated in Fig. 4.1.

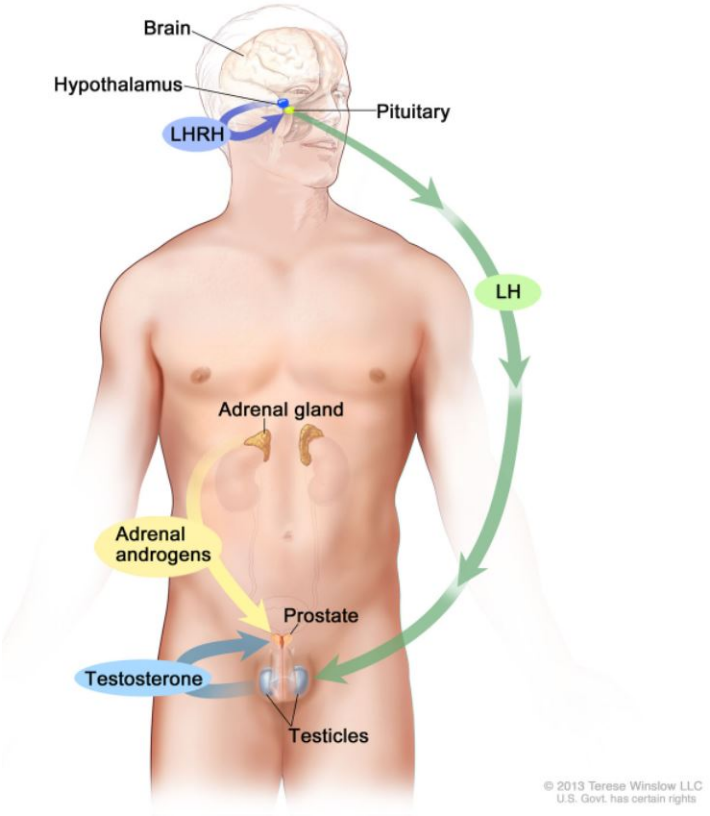

Figure 4.1: Androgen production process. Source: Terese Winslow LLC, Medical And Scientific Illustration.

Androgen deprivation therapy is based on the use of three types of drugs: LHRH agonists, LHRH antagonists and anti-androgens. The LHRH agonists and LHRH antagonists drugs aim to lower the amount of testosterone made by the testicles while the anti-androgens target the androgen receptors on the prostate cells [w1, w2, w3].

LHRH agonists

An agonist is a molecule that replicates the action of another molecule. The use of drugs based on LHRH agonists cause an increase of the LHRH dosage in the body. The hyperstimulation of the pituitary gland then induces a defensive reaction from the hypothalamus which blocks the synthesis of LHRH. The pituitary gland stops responding and therefore stops stimulating the testicles to produce testosterone. However, testosterone levels rise briefly due to the increase of LHRH levels in the beginning of the treatment before dropping to very low levels. This effect of the LHRH agonist is known as tumor flare. LHRH agonists drugs can either be injected or placed as small implants under the skin.

LHRH antagonists

An antagonist is a molecule that binds to a cell receptor and blocks or weakens the physiological effect of another molecule. LHRH antagonists directly inhibit the action of the LHRH by blocking the pituitary LHRH receptors thus stopping the pituitary gland from making the LH necessary for the production of testosterone. Testosterone levels

fall more rapidly than with LHRH agonists, and LHRH antagonists do not cause tumor flares. LHRH antagonists drugs can either be injected under the skin or taken as pills.

Anti-androgens

The anti-androgens stop androgens from working. In order for prostate cells to use androgen as a growth factor, androgen must bind to the prostate cell androgen receptor. Anti-androgens are drugs that connect to these receptors keeping the androgens from doing so. They are also sometimes called androgen antagonists. LHRH agonists drugs are prescribed together with anti-androgens drugs to avoid tumor flare.

Testosterone is the main male hormone responsible for regulating the development and maintenance of male features. Therefore, reducing androgen levels through androgen deprivation therapy leads to several side effects including reduced or absent sexual desire, erectile dysfunction, shrinkage of testicles and penis and growth of breast tissue (gynecomastia). Moreover, over time, prostate cancer cells adapt to the unfavorable environment by mutating from androgen-dependent cancer cells into androgen-resistant cancer cells and the hormone therapy is no longer effective. In addition, ADT helps to reduce tumor volume and slow tumor progression, but hormone therapy alone does not cure prostate cancer. In the next section, we present a second therapy for prostate cancer that we combine with hormone therapy later on.

4.2.2 Brachytherapy

Brachytherapy for prostate cancer is an internal radiation therapy where sealed radiation sources are placed inside the prostate gland. It is usually prescribed for localized tumors where the volume to be treated is limited. There are two types of brachytherapy. High dose rates (HDR) brachytherapy where the sources are placed temporarily in the prostate for a few minutes to deliver high dose radiation and low dose rates (LDR) brachytherapy where the sources are placed permanently in the prostate to deliver low dose radiation [w4]. The prostate is a gland that is surrounded by several sensitive organs such as the rectum and bladder. It is also crossed by the urethra as shown in Fig.4.2. Therefore, it is very important to spare the organs at risk from radiation as much as possible when placing the radioactive sources.

For the placement of the radiative source a general anesthesia or spinal anesthesia of the abdomen and legs is performed and catheters containing the sealed sources are placed into the prostate gland using a template grid. An endorectal ultrasound probe is inserted into the rectum to help visualize the prostate, the volume to be treated as well as the organs at risk and guide the physician in the placement of the catheters [w5, w6]. An example of the equipment used for the placement of the radioactive sources is shown in Fig.4.3.

For the LDR brachytherapy, three kinds of sources are usually used to deliver the low dose radiations: Iodine 125 (I-125), Palladium 103 (Pd-103) or Cesium-131 (Cs-131). The radioactive seeds are preloaded into the needles and placed into the prostate, either manually or automatically as shown in Fig. 4.5. For the HDR brachytherapy, either the iridium 192 (Ir-192) or the Cobalt 60 (Co-60) are used. The catheters are placed in the prostate and connected by tubes to a computer-controlled machine that injects the highly radioactive sources directly into the catheters. The procedure lasts a few minutes and once the catheters are removed, no radioactive substances are left in the prostate.

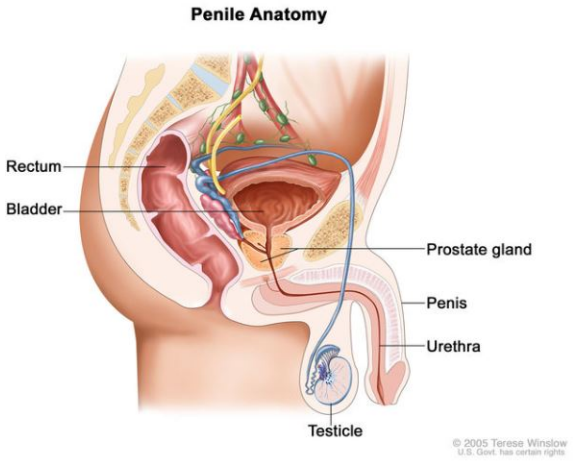

Figure 4.2: Penile anatomy. Source: Terese Winslow LLC, Medical And Scientific Illustration.

(a) Catheter

(b) Template grid for catheters

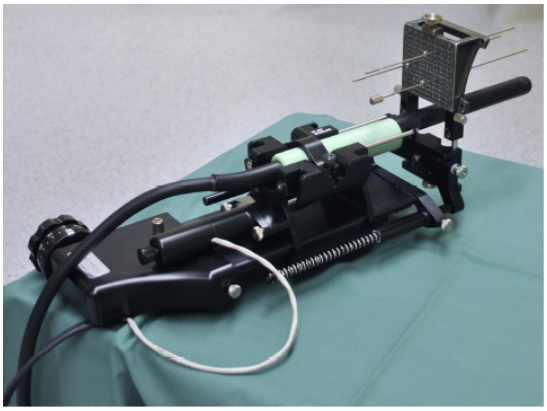

(c) Prostate brachytherapy setup

Figure 4.3: An example of prostate brachytherapy equipment [86].

An example of an ultrasound image obtained from the endorectal ultrasound probe used during prostate cancer brachytherapy is shown in Fig 4.4. As with androgen deprivation therapy, brachytherapy has its share of side effects including pain or discomfort when

urinating, blood in the urine, erectile dysfunction, bleeding from the rectum and even cancer in the bladder or rectum caused by their exposure to the radiation.

(a) Permanent implant size comparison [87].

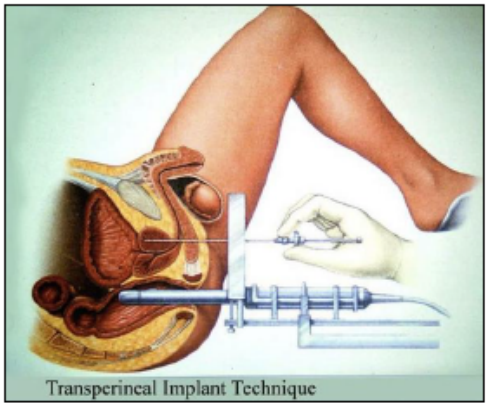

(b) LDR brachytherapy procedure [77].

Figure 4.4: Schematic of the implementation device of prostate LDR brachytherapy.

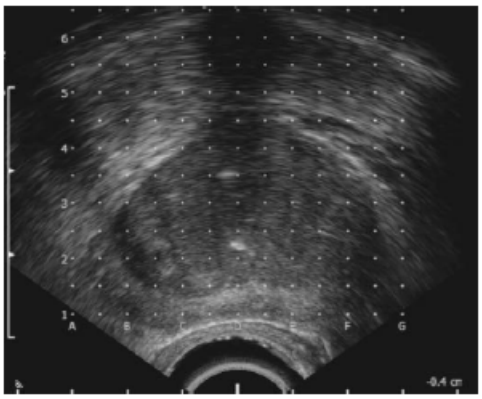

Figure 4.5: Ultrasound image of the treatment area for a prostate cancer patient [86].

In the next section, we use all the biological and medical information presented so far to formulate the mathematical model for the treatment of prostate cancer under combined hormone therapy and brachytherapy.

4.3 Mathematical modeling of prostate cancer under combined therapies

To model the growth and spread of cancer cells in a patient with prostate cancer, we propose a spatial model inspired by the one presented by Friedman A. et al. in [84]. To describe our model, we first note that the volume of the tumor changes with time. We, thus, assume that the tumor is occupying a region $\Sigma(t)$ at time t in a bounded domain Ω containing it.

The evolution of the prostate tumor is described through the evolution of the densities of the different cells composing it. The growth and spread of prostate cells are presented in the following section.

4.3.1 Dynamics of the prostate cells

In this section, the considered dynamics governing cell behavior are discussed and modeled. First regarding the movement of the cells and second regarding their growth.

Movements of the prostate cells

The cells are surrounded and supported by the extracellular matrix (ECM) which, as an adhesive substrate, plays an important role in cell adhesion, movement and motility [21, 89, 90].
In our work, we consider two different types of cell movement: a random movement of the cells and a directional cell movement induced by the adhesion gradient of the ECM. In this case the cells move in the direction of a positive gradient of the chemicals bound to the ECM. This directional motility, also known as haptotaxis is involved in several biological processes such as wound healing and tumor cell invasion [88].
Metastasis or tumor cell invasion is one of the most dangerous aspects of cancer, as the tumor is no longer localized but rather spreads to other locations. This phenomenon occurs due to the degradation of the ECM by cancer cells and was widely studied and taken into consideration while modeling tumor evolution [89–93].
By degrading their support, cancer cells are able to migrate and spread. To do so, they produce the matrix degradative enzymes (MDEs) that erode the ECM locally by altering cell adhesion. This also enables the cells to make a space where they can move by diffusion (random motility).
In the present work, we used the simplified method provided by Alina Toma et al. in [92] to model tumor growth which does not explicitly model the MDEs and where the degraded ECM can be simulated directly using the cancer cell distribution. The ECM f is, thus, directly degraded by cancer cells with a coefficient α_f and is regenerating with a rate β_f.

Growth of the prostate cells

Since androgen acts as a growth factor for the cells, the evolution of prostate cells depends on the level of androgen available in their environment. In the present work, we used the same growth rate profiles for androgen-dependent and castration-resistant cells as presented in [76, 84, 94, 95].
The growth rate K_{A_d} of the androgen dependent cells A_d is an increasing and saturating function of the androgen level A defined as follows:

$$K_{A_d}(A) = \underbrace{\lambda_{A_d}\left(\lambda_1 + (1-\lambda_1)\frac{A}{A+k_1}\right)}_{\text{Proliferation rate}} - \underbrace{\mu_{A_d}\left(\mu_1 + (1-\mu_1)\frac{A}{A+k_1}\right)}_{\text{Death rate}} \tag{4.1}$$

The growth rate K_{A_r} of castration-resistant cells A_r is a decreasing function of androgen defined as follows:

$$K_{A_r}(A) = \underbrace{\lambda_{A_r}}_{\text{Proliferation rate}} - \underbrace{\mu_{A_r}\left(\mu_2 + (1-\mu_2)\frac{A}{A+k_2}\right)}_{\text{Death rate}} \tag{4.2}$$

In an environment full of androgen the androgen dependent cells A_d proliferate at a maximum rate λ_{A_d} and die at a rate μ_{A_d} while castration-resistant cells are considered androgen-repressed and have a negative growth rate in the presence of androgen. As in [95], their proliferation rate is considered androgen independent and has a constant value of λ_{A_r} while their death rate is an increasing and saturating function of androgen. λ_1 quantifies the impact of androgen concentration on A_d proliferation. It represents the A_d proliferation rate in the absence of androgens compared to its value under abundant androgens. A value of 0 as in [76] means that A_d cells do not multiply without androgens while a value of 0.8 as in [95] means that A_d cells lose 20% of their maximum proliferation rate when there is no more androgen in the medium. Likewise, μ_1 and μ_2 quantify the impact of androgens concentration on A_d and A_r death respectively. They represent their death rate in the absence of androgens compared to its value under abundant androgens such that $\mu_1 > 1$ to increase A_d death in a low androgen environment and $\mu_2 < 1$ to lower A_r death in the unfavorable environment.
Moreover, in order to survive in an androgen-depleted environment, A_d cells mutate into A_r cells with a rate K_m. The more the environment is unfavorable for the A_d cells, the more likely they will mutate into A_r to survive [81]. The mutation rate K_m is therefore a decreasing function of androgen. The mutation is considered irreversible for simplicity [76, 84, 94] and the mutation rate is defined as:

$$K_m(A) = K_{max}\left(1 - \frac{A}{A_0}\right) \tag{4.3}$$

where A_0 is the normal level of androgen concentration in healthy condition and K_{max} is the maximum mutation rate.
Normal cell proliferation is regulated through contact inhibition. This process allows a healthy cell to stop its own proliferation when it comes into contact with another cell. Cancer cells do not have this characteristic, resulting in uncontrolled and excessive cancer cell proliferation and solid tumor development [96]. Compared to cancer cells, healthy cells H are assumed to multiply at a constant growth rate K_H while considering the maximum cell carrying capacity K_0 [84].

4.3.2 Mathematical modeling of both therapies

In this section, we are interested in modeling the effects of the hormone therapy and brachytherapy and the response of prostate cells to both therapies.

Hormone therapy

Androgen deprivation therapy (ADT) aims to deplete the prostate of androgens or to prevent them from getting into prostate cells in order to kill the cancer cells that rely on it to survive and multiply. We model the case of LHRH antagonists drugs that directly interfere with the production of androgens in the prostate.
Throughout the treatment period, the ADT can be delivered continuously or intermittently, alternating periods of treatment with periods of rest. The intermittent androgen suppression (IAS) method depends on the PSA levels to control the treatment schedule. The prostate-specific antigen (PSA) is a protein produced by prostate cells and is normally found at very low levels in the blood of men with healthy prostate and is used as a biomarker for monitoring prostate cancer [97].
The IAS is switched on when the PSA level is above a certain critical level P_0 and is switched off when the PSA level goes down below the critical level P_0. This results in depletion of androgen production and this decrease is modeled by reduction in the normal rate of androgen production by a factor of $1 + \lambda_u u(P)$. Here, $u(\cdot)$ is a smooth function and P represents the PSA level such that $u(P) = 1$ when the IAS is switched on and $u(P) = 0$ when the IAS is switched off. For simplicity, and as in [76, 80, 84], the PSA concentration P is considered proportional to the total number of cancer cells as follows:

$$P = P(t) = \int_\Omega \beta_{PSA}(A_d + A_r)\, dx \tag{4.4}$$

The diffusion of the androgen concentration A in the prostate under hormone therapy is therefore defined as follows:

$$\frac{\partial A}{\partial t} - D_A \Delta A = \underbrace{\frac{\lambda_A}{1 + \lambda_u u(P,t)}}_{\text{drug-inhibited production}} - \underbrace{\mu_A A}_{\text{natural decay}} - \underbrace{\lambda_0 (A_d + A_r) A}_{\text{consumption by } A_d \text{ and } A_r} \tag{4.5}$$

Eq.(4.5) can easily be adapted to model other types of drugs used in hormone therapy. LHRH agonists are always prescribed with anti-androgens to avoid tumor flare. In order to model this type of treatment, we would have to take into account, in addition to the decrease in androgen production, the direct effect of anti-androgens on the available androgens. This can be modeled by using an additional androgen decay rate. In the case where anti-androgens are used alone, we would have to take u = 0 and keep only the additional androgen decay rate.

Brachytherapy

In radiation therapy, X-rays or photons travel through the patient's tissue to reach the tumor. In brachytherapy the decaying radioactive sources are placed inside the organ and release energetic beams whose energy depends on the nature of the source used. As the photons travel through the medium, their energy decreases with an attenuation coefficient k [83]. k quantifies the energy loss caused by the distance between the irradiated area and the radioactive source. Its value depends on the energy of the photons and the medium crossed [98, 99]. Moreover, the radioactivity of the source declines over time with a decay constant λ.

The linear quadratic LQ model is generally used to evaluate the biological effect of a radiation dose D on the irradiated tissue [101–103]. The survival probability S of cells exposed to a radiation dose D is given by:

$$S = \exp(-(\alpha D + \beta G D^2)) \tag{4.6}$$

where α and β describe the radiosensitivity of the tissue. α is the yield rate for lethal lesions, and β for sublethal-reparable lesions. The parameter G is a dose-rate factor which depends on the radiation course.

We consider M radiative source locations and denote by x_m the locations of the sources, $1 \leq m \leq M$.

During the radiation course $[0, \tau]$, the irradiation by the source m is given at a dose rate $R_m(t) = \mathrm{d}D_m(t)/\mathrm{d}t$ such that :

$$R_m(t) = R_{m_0} \exp(-\lambda t)$$

where R_{m_0} is the source m initial dose rate and λ its radioactive decay constant.

The radiation dose rate $R_S(x,t)$ absorbed at a given $x \in \Omega$ at time t from the source m is given by :

$$R_S(x,t) = R_m(t) \exp(-k\|x - x_m\|)$$

where k is the attenuation factor.

The total absorbed dose rate R_T is given by :

$$R_T(x,t) = \sum_m R_m(t) \exp(-k\|x - x_m\|). \tag{4.7}$$

Radiotherapy does not distinguish between healthy and cancerous cells. The target cells in brachytherapy are therefore A_d, A_r and H. However, normal healthy cells are less sensitive to radiation than cancer cells. Their DNA repair capacity from sublethal lesions is generally greater. Therefore, we mitigate the brachytherapy killing rate of healthy cells by a factor ε compared to cancer cells.
The brachytherapy destroys the cells with a space and time dependent killing rate, $\mu_B(x,t)$ such that the death rate from a total dose rate delivered at time t is:

$$\mu_B(x,t) = 1\text{–}S = 1 - \exp(-(\alpha R_T(x,t) + \beta G R_T(x,t)^2)) \tag{4.8}$$

4.4 A PDE model for prostate cancer under combined treatment

We summarize the dynamics of cancer cells, healthy cells and androgens in the context of prostate cancer under hormone therapy and brachytherapy along with the different variables used in the following section.

4.4.1 Prostate cancer mathematical model

The variables used to describe the evolution of prostate cancer are listed as follows:

1. A_d = Density of androgen-dependent cancer cells,
2. A_r = Density of androgen-repressed cancer cells,
3. H = Density of healthy cells,
4. f = Density of the ECM,
5. A = Concentration of androgens,
6. P = Concentration of prostate-specific antigen (PSA).

We have the following system of partial differential equations modeling the dynamics of cells, ECM and the androgen concentration:

$$\begin{cases} \partial_t A_d + \chi \nabla \cdot (A_d \nabla f) - D\Delta A_d = K_{A_d}(A)A_d - K_m(A)A_d - \mu_B(x,t)A_d & on\ \Omega \times [0,T] \\ \partial_t A_r + \chi \nabla \cdot (A_r \nabla f) - D\Delta A_r = K_{A_r}(A)A_r + K_m(A)A_d - \mu_B(x,t)A_r & on\ \Omega \times [0,T] \\ \partial_t H + \chi \nabla \cdot (H \nabla f) - D\Delta H = K_H H \left(1 - \dfrac{A_d + A_r + H}{K_0}\right) - \varepsilon \mu_B(x,t)H & on\ \Omega \times [0,T] \\ \partial_t f = -\alpha_f (A_d + A_r) f + \beta_f f & on\ \Omega \times [0,T] \\ \partial_t A - D_A \Delta A = \dfrac{\lambda_A}{1 + \lambda_u u(P,t)} - \mu_A A - \lambda_0 (A_d + A_r) A & on\ \Omega \times [0,T] \\ \\ \text{with boundary conditions :} \\ A_d = 0 & on\ \partial\Omega \times [0,T] \\ A_r = 0 & on\ \partial\Omega \times [0,T] \\ H = 0 & on\ \partial\Omega \times [0,T] \\ f = f_0 & on\ \partial\Omega \times [0,T] \\ A = A_0. & on\ \partial\Omega \times [0,T] \end{cases} \tag{4.9}$$

Boundary equations for A_d, A_r, f and A are derived from the observation that the outer medium is assumed to be healthy, thus containing neither type of cancer cell, and with a constant androgen concentration and ECM density. The boundary condition on the healthy prostate cells H is derived from the prostate being enclosed in Ω. The known parameters in the above PDE model are described in Table.4.1.

4.4.2 Numerical evaluation of the PDE system parameters

In order to carry out the simulations, the numerical values listed in Table.4.2 were used. In addition, for the parameters related to the androgen evolution, the value of the production and natural decay rates of androgen are selected so as to respect the saturating level of androgens A_0 which represents the natural level of androgen in healthy conditions and is given by $A_0 = \lambda_A/\mu_A$ [84]. With μ_A being of about $10^{-2} day^{-1}$ [94] we used $\lambda_A = 0.2 nM day^{-1}$ and $\mu_A = 10^{-2} day^{-1}$. To have a reference value for λ_0 we took into consideration the carrying capacity K_0 ($\sim 10^7 \#cells/cm^3$) and the natural decay rate of androgen ($\sim 10^{-2} day^{-1}$). The lambda used in the simulations is therefore $\lambda_0 = 10^{-9} \#cells^{-1} cm^3 day^{-1}$.

Table 4.1: Parameters description

Parameter	Descritpion	Comment
χ	Haptotaxis coefficient	Constant related to cell-ECM adhesion
D	Cell diffusion coefficient	Responsible for the non motile part of the cell migration by inducing a progressive wavefront
K_{A_d}	A_d growth rate	Increasing and saturating function of A. Negative when A is small and tends to a positive constant when A is large.
K_{A_r}	A_r growth rate	Decreasing function of A. Negative when A is large.
K_m	A_d mutation rate	Irreversible change in genetic sequence.
μ_B	Brachytherapy killing rate	Biological effect of brachytherapy on prostate cells
K_0	Maximum cell carrying capacity	Capacity in number of cells per cm^3
K_H	H growth rate	Positive constant
α_f	ECM degradation coefficient	Quantifies the effect of cancer cells on ECM degradation
β_f	ECM remodeling rate	Natural regeneration of ECM
D_A	Androgen diffusion coefficient	Responsible for the diffusion of androgen in the cells environement
u	Hormone therapy switch	The function that activates/deactivates the hormone treatment in case of intermittent schedule
λ_u	Hormone therapy intensity	Coefficient to control the intensity of the androgen deprivation
λ_A	Androgens production rate	Normal androgen concentration for adult males
μ_A	Androgens natural decay rate	Androgen dynamics time constant
λ_0	Androgens consumption rate	Consumption rate by cancer cells
P	PSA concentration	Prostate Specific Antigen concentration in blood

To compute the rate of PSA production by cancer cells, we relied on the results in [105] who quantified the PSA production rate per tumor volume : $\beta_{PSA} = \beta_c * Volume_{cells}/Volume_{prostate}$ where $Volume_{cells} = 1.5\ 10^{-8} cm^3$ [89].

Normal prostate cells have a rate of division almost equal to their rate of apoptosis, so their growth rate is extremely low [106]. In this work we used $K_H = 0.003 day^{-1}$.
For the LDR brachytherapy, the source used in this work is the Iodine 125 (I−125). It has a half-life of ($\sim$ 60 days), which is the time the source needs to lose about half of its radioactive activity. The decay constant of I-125 is thus $\lambda = 0.011 day^{-1}$ [87].
In terms of photon absorption, the human tissues are comparable to the "water" medium and the I−125 source produces photons with a low energy of ($\sim 28 keV$), the attenuation coefficient k used is thus $k = 0.409 cm^{-1}$ [100]. The attenuation coefficient is a decreasing function of photon energy, the photons produced in low-dose brachytherapy therefore have a high attenuation coefficient which allows for a better preservation of the surrounding healthy tissues.

Table 4.2: Numerical values of the parameters and their sources

Parameter	Value	Unit	Source
χ	2600	$cm^2 M^{-1} s^{-1}$	[89]
D	10^{-9}	$cm^2 s^{-1}$	[89]
λ_{A_d}	0.4621	day^{-1}	[95]
λ_{A_r}	0.4621	day^{-1}	[95]
μ_{A_d}	0.3812	day^{-1}	[95]
μ_{A_r}	0.4765	day^{-1}	[95]
λ_1	$0 - 1$	$-$	[94]
μ_1	1.35	$-$	[95]
μ_2	$0.25 - 1.0$	$-$	[95]
K_{max}	5×10^{-5}	day^{-1}	[94]
A_0	20	nM	[94]
K_0	6.7×10^7	$\#cells/cm^3$	[89]
α_f	1.49×10^{-14}	$\#cells^{-1} cm^3 s^{-1}$	[92]
β_f	10^{-7}	s^{-1}	[92]
D_A	$10^{-11} - 10^{-13}$	$m^2 s^{-1}$	[104]
P_0	10	ng/ml	[94]
β_c	$1.7210 - 6.9722$	$ng/mm^3/day$	[105]
λ	0.011	day^{-1}	[103]
α	0.15	Gy^{-1}	[103]
β	0.048	Gy^{-2}	[103]

4.5 Numerical resolution of the PDE system

The PDE model (4.9) is solved using the general purpose finite element package FreeFem++ [70, 71].
To do so, we need to write the weak formulation for each variable. We consider the discretization in time:

$$t_0 = 0; t_1 = t_0 + dt = dt; ...; t_n = ndt; ...; t_N = Ndt = T.$$

We use an implicit scheme for the discretization in time of all the equations of except for the healthy cells PDE for which a semi-implicit scheme is used. The system (4.9) is therefore discretized in time as follows:

$$\begin{cases} \dfrac{A_d^{n+1}-A_d^n}{dt}+\chi\nabla\cdot(A_d^{n+1}\nabla f^n)-D\Delta A_d^{n+1}=K_{A_d}(A^n)A_d^{n+1}-K_m(A^n)A_d^{n+1} \\ -\mu_B A_d^{n+1}, \\ \dfrac{A_r^{n+1}-A_r^n}{dt}+\chi\nabla\cdot(A_r^{n+1}\nabla f^n)-D\Delta A_r^{n+1}=K_{A_r}(A^n)A_r^{n+1}+K_m(A^n)A_d^{n+1} \\ -\mu_B A_r^{n+1}, \\ \dfrac{H^{n+1}-H^n}{dt}+\chi\nabla\cdot(H^{n+1}\nabla f^n)-D\Delta H^{n+1}=K_H H^{n+1}\left(1-\dfrac{A_d^{n+1}+A_r^{n+1}+H^n}{K_0}\right) \\ -\varepsilon\mu_B(x,t)H^{n+1}, \\ \dfrac{f^{n+1}-f^n}{dt}=-\alpha_f(A_d^{n+1}+A_r^{n+1})f^{n+1}+\beta_f f^{n+1}, \\ \dfrac{A^{n+1}-A^n}{dt}-D_A\Delta A^{n+1}=\dfrac{\lambda_A}{1+\lambda_u u}-\mu_A A^{n+1}-\lambda_0(A_d^{n+1}+A_r^{n+1})A^{n+1}, \\ +B.C.+I.C. \end{cases} \tag{4.10}$$

In the brachytherapy killing rate expression Eq.(4.8) we recall that the parameter G represents the dose protraction factor. For the external-beam radiation therapy where the total radiation dose is split into n individual dose over the treatment period, $G=1/n$ [103]. In the present work, although permanent implants are used, the discretization in time leads to the splitting of the total dose into (T/dt) doses where dt is the time step chosen in the simulations. For this reason we used $G=1/(T/dt)$ in the simulations.
The weak formulations of the problem (4.10) are written as follows:

$$\begin{cases} \text{Find}\quad A_d^{n+1}\in H_0^1(\Omega)\quad\text{such that}\quad \forall\varphi\in H_0^1(\Omega) \\ \int_\Omega \dfrac{A_d^{n+1}-A_d^n}{dt}\varphi-\chi\int_\Omega A_d^{n+1}\nabla f^n\cdot\nabla\varphi+D\int_\Omega\nabla A_d^{n+1}\nabla\varphi-\int_\Omega K_{A_d}(A^n)A_d^{n+1}\varphi \\ +\int_\Omega K_m(A^n)A_d^{n+1}\varphi+\int_\Omega\mu_B A_d^{n+1}\varphi=0, \end{cases} \tag{4.11}$$

$$\begin{cases} \text{Find}\quad A_r^{n+1}\in H_0^1(\Omega)\quad\text{such that}\quad \forall\varphi\in H_0^1(\Omega) \\ \int_\Omega \dfrac{A_r^{n+1}-A_r^n}{dt}\varphi-\chi\int_\Omega A_r^{n+1}\nabla f^n\cdot\nabla\varphi+D\int_\Omega\nabla A_r^{n+1}\nabla\varphi-\int_\Omega K_{A_r}(A^n)A_r^{n+1}\varphi \\ -\int_\Omega K_m(A^n)A_d^{n+1}\varphi+\int_\Omega\mu_B A_r^{n+1}\varphi=0, \end{cases} \tag{4.12}$$

$$\begin{cases} \text{Find}\quad H^{n+1}\in H_0^1(\Omega)\quad\text{such that}\quad \forall\varphi\in H_0^1(\Omega) \\ \int_\Omega \dfrac{H^{n+1}-H^n}{dt}\varphi-\chi\int_\Omega H^{n+1}\nabla f^n\cdot\nabla\varphi+D\int_\Omega\nabla H^{n+1}\nabla\varphi \\ -\int_\Omega K_H H^{n+1}\left(1-\dfrac{A_d^{n+1}+A_r^{n+1}+H^n}{K_0}\right)+\varepsilon\int_\Omega\mu_B H^{n+1}\varphi=0, \end{cases} \tag{4.13}$$

$$\begin{cases} \text{Find} \quad A^{n+1} \in H^1(\Omega) \quad \text{such that} \quad \forall \varphi \in H_0^1(\Omega) \\ \int_\Omega \dfrac{A^{n+1}-A^n}{dt}\varphi + D_A \int_\Omega \nabla A^{n+1} \nabla \varphi - \int_\Omega \dfrac{\lambda_A}{1+\lambda_u u}\varphi + \mu_A \int_\Omega A^{n+1}\varphi \\ +\lambda_0 \int_\Omega (A_d^{n+1} + A_r^{n+1}) A^{n+1}\varphi = 0, \end{cases} \tag{4.14}$$

The computation of f^{n+1} is done as follows:

$$f^{n+1} = \frac{1}{1 + dt(\alpha_f(A_d^{n+1} + A_r^{n+1}) - \beta_f)} f^n \tag{4.15}$$

4.5.1 Simulation results of the prostate PDE system

Androgen deprivation results in side effects related to the male characteristics of the patients that greatly influence their quality of life. Therefore, the evolution of the androgen level during the treatment should be monitored. This is also one of the reasons why intermittent treatment may be considered. Discontinuous androgen deprivation not only delays the appearance of castration-resistant cancer cells and reduces their number, but might also help to preserve the body's androgen reserves.
With brachytherapy, the concern is the preservation of the organs near the prostate that will also be exposed to the radiation depending on their proximity to the radioactive sources. Particularly, the urethra, which crosses the prostate at its center. Therefore, the dose absorbed by the urethra needs to be monitored [77].
The outputs of our model are thus the evolution of the different cell densities and of the androgen concentration as well as the distributions of the isodose curves received by the prostate and the urethra.
For the simulations, we considered a transverse section of the prostate. The prostate appears as an ellipse with a semi-major axis of 4cm and semi-minor axis of 3cm and is crossed at it center by the urethra which is shaped as a circle with a diameter of 10mm. As initial conditions of our model, the tumor mass is considered localized on the left lobe of the prostate and the cancer cells represent 14% of the maximum cell carrying capacity K_0. The radioactive sources are placed inside the tumor mass. The objective is to explore different therapeutic strategies using the androgen deprivation therapy and the brachytherapy. The initial distributions of the prostate cells is shown in Figure 4.6.

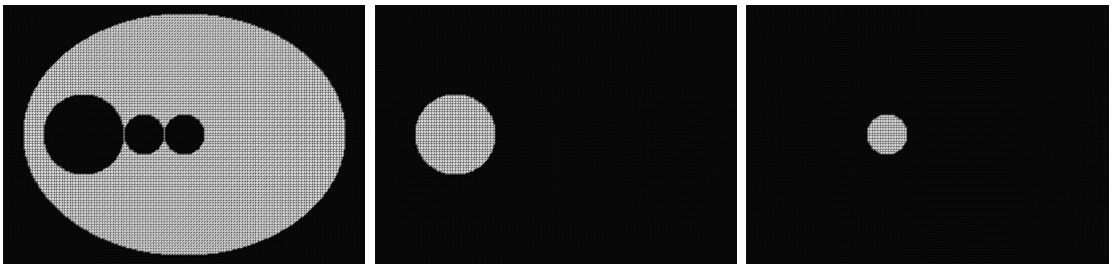

(a) (b) (c)

Figure 4.6: Initial cells distribution in black and white printing (black indicates areas with no cell density) for (a) Healthy prostate cells (b) Androgen dependent cancer cells (c) Androgen repressed cancer cells

We first consider the case of each therapy administered as a monotherapy before investigating the combination of the androgen deprivation therapy with the brachytherapy. The analysis of the results is supported, in each scenario, by clinical information obtained through discussions with oncologists.

Androgen deprivation therapy simulations

At first, we deactivate the brachytherapy and deliver only the androgen deprivation therapy. To compare the effect of using continuous androgen deprivation and an intermittent treatment schedule, we observe the results of six months of treatment over a one-year period. For the continuous androgen suppression therapy (CAS), the treatment is applied over the first six months while for the intermittent androgen suppresion therapy (IAS) the treatment is applied throughout the year depending on the PSA level for a maximum total duration of drug administration not exceeding six months. The numerical results are shown in Figure 4.7, Figure 4.8, Figure 4.9 and Figure 4.10.

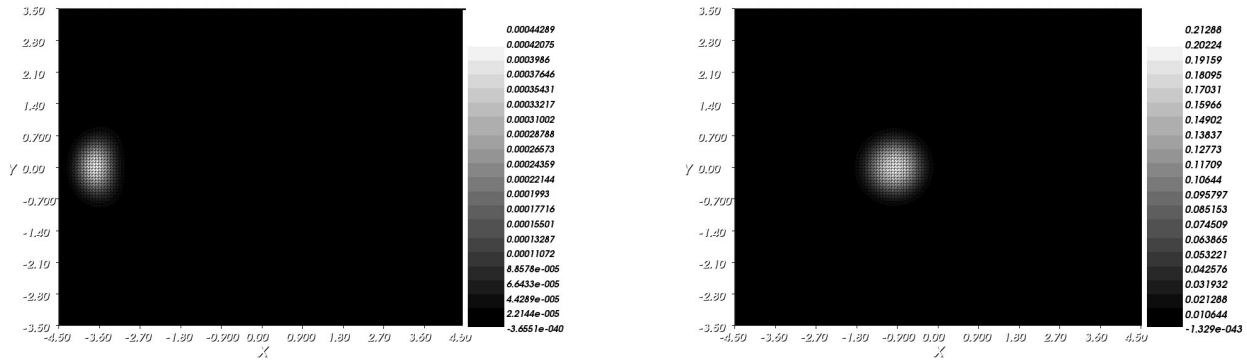

(a) A_d cancer cells

(b) A_r cancer cells

Figure 4.7: Prostate cancer cell distribution in percentage of the maximum cell carrying capacity of the prostate at $t = 364$ day after CAS monotherapy.

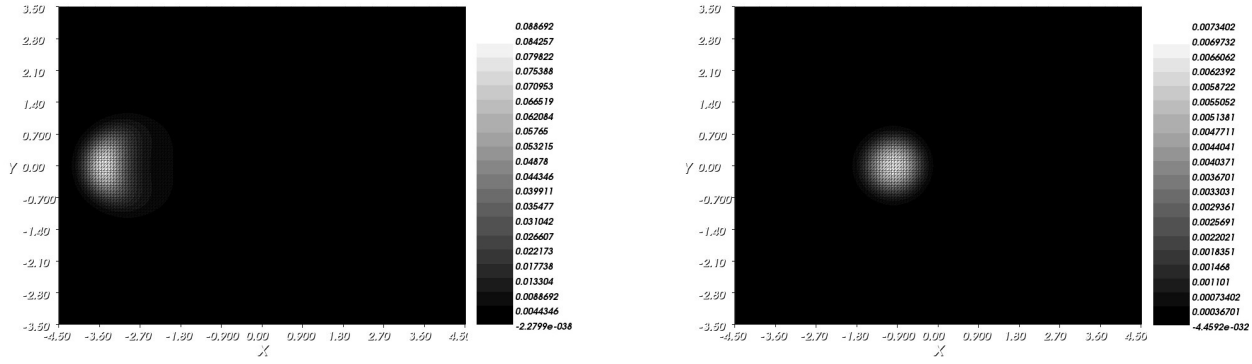

(a) A_d cancer cells

(b) A_r cancer cells

Figure 4.8: Prostate cancer cell distribution in percentage of the maximum cell carrying capacity of the prostate at $t = 364$ day after IAS monotherapy.

The prostate tumor is composed of androgen dependent and androgen resistant cancer cells. In Figure 4.9(a) where the CAS is administered over the first six month, the treatment is effective at first and the tumor volume comprising essentially of androgen-dependent cancer cells decreases quickly. However, the percentage of the androgen re-

pressed cells starts to rise steadily and the treatment is no longer effective.

From Figure 4.10 we notice that this happens when the environment is consistently depleted of androgen and the androgen concentration remains almost constant at a low level in the case of the CAS therapy. In Figure 4.10, at the end of the CAS therapy ($t = 182$ days) the androgen level starts to increase towards its saturation level causing the tumor volume composed mainly of the androgen-repressed cancer cells to start decreasing. However, the tumor had reached a percentage of almost 40% of the prostate volume which is a critical volume.
In the case of the IAS therapy, the evolution of the androgen-repressed cancer cells, which do not respond to the androgen deprivation therapy, is contained and the tumor volume is bounded as shown in Figure 4.9 (b). The androgen level does not drop below 60% of its saturation level upon restarting the intermittent treatment, unlike in the continuous treatment where the androgen level is kept at 45% throughout the six months of treatment. This could represent a significant benefit for patients who struggle with the side effects of androgen deprivation.

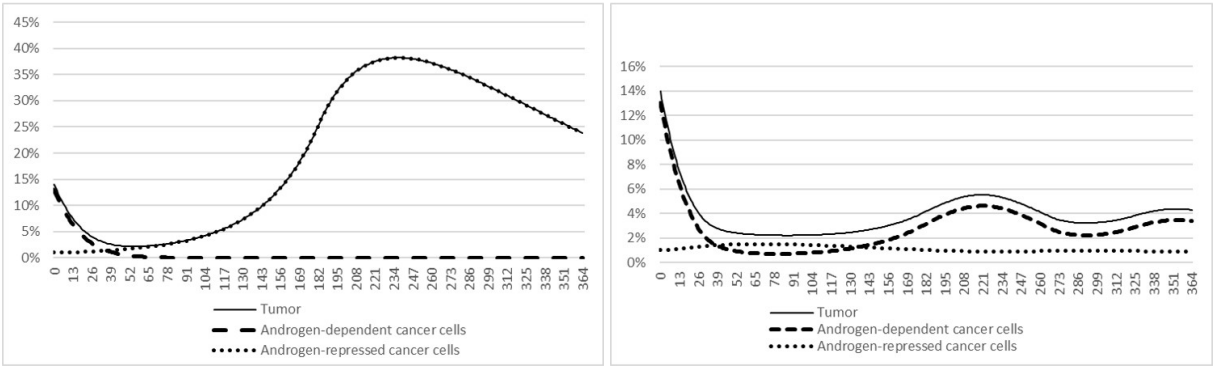

(a) (b)

Figure 4.9: Cancer cells and tumor evolution under androgen deprivation therapy in percentage of the maximum cell carrying capacity of the prostate: (a) Continuous deprivation, (b) Intermittent deprivation.

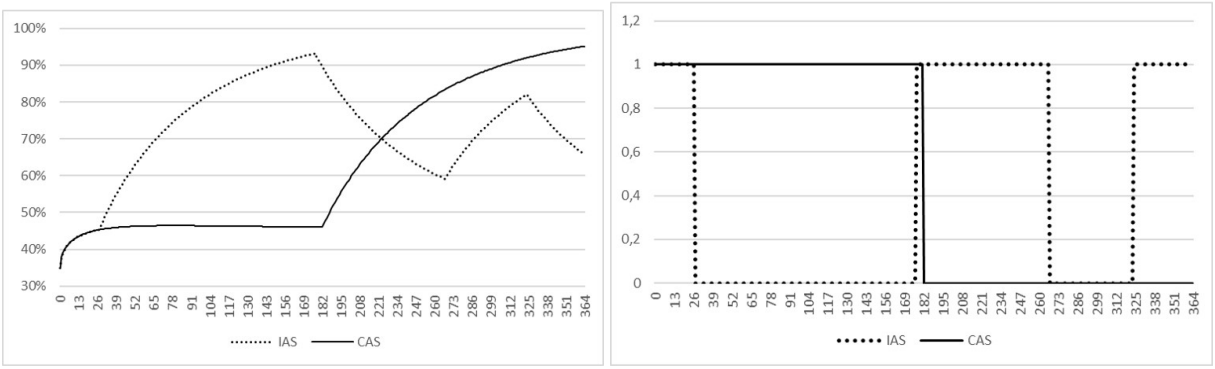

(a) (b)

Figure 4.10: Androgen deprivation therapy outputs: (a) Androgen concentration evolution in percentage of the androgen saturation level A_0, (b) ADT treatment schedule.

From a clinical point of view, continuous hormone therapy necessarily leads to treatment failure because of the loss of sensitivity of cancer cells to androgen. Moreover, hormone therapy does not cure prostate cancer, but at best stops the proliferation of cancer cells and reduces tumor volume. This supports the results we obtained using a monotherapy based on androgen deprivation therapy. Furthermore, intermittent hormone therapy on its own is used for advanced late-stage cancer patients who need lifelong treatment. In this case, IAS helps in controlling the tumor volume, but most importantly, it offers the patient the opportunity to rest during the treatment breaks.

Brachytherapy simulations

In order to observe the impact of brachytherapy on the different cell densities, we deactivate the hormone therapy to keep only the brachytherapy. Brachytherapy aims to kill cells through radiation emitted from a radioactive source placed inside the tumor mass. I−125 with its half-life of $\sim$ 60 days retains only 50% of its radioactivity after 60 days, 12.5% after 180 days and $< 2\%$ after 360 days. The intensity of the treatment therefore gradually decreases until it disappears. Radiation does not distinguish between healthy and cancerous tissues. It is therefore necessary to monitor the dose absorbed by the organs at risk surrounding the prostate. The minimum dose to treat the tumor initially considered by brachytherapy alone for our model is 120Gy. We are interested in combining brachytherapy with another therapy to decrease the radiation dose while still curing the tumor. This way we can better protect the patients from the side effects of radiation. For a dose of $120Gy$, the isodose curves at the beginning of the treatment when the radioactivity is at its maximum are shown in Figure 4.11.

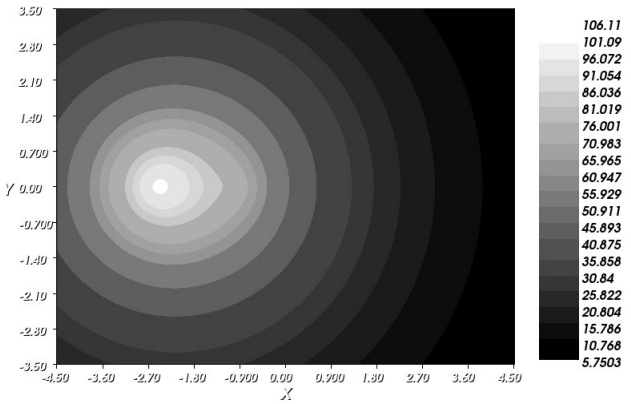

Figure 4.11: Isodose curves at $t = 0$ for a dose of $120Gy$.

The difference between the dose of $120Gy$ and the maximum absorbed dose of $106.11Gy$ in Figure 4.11 is due to the distance between the radioactive sources. The distribution of the absorbed doses in the prostate and urethra are shown in Figure 4.12 and the biological effect of these doses on the cancer cells is shown in Figure 4.13.

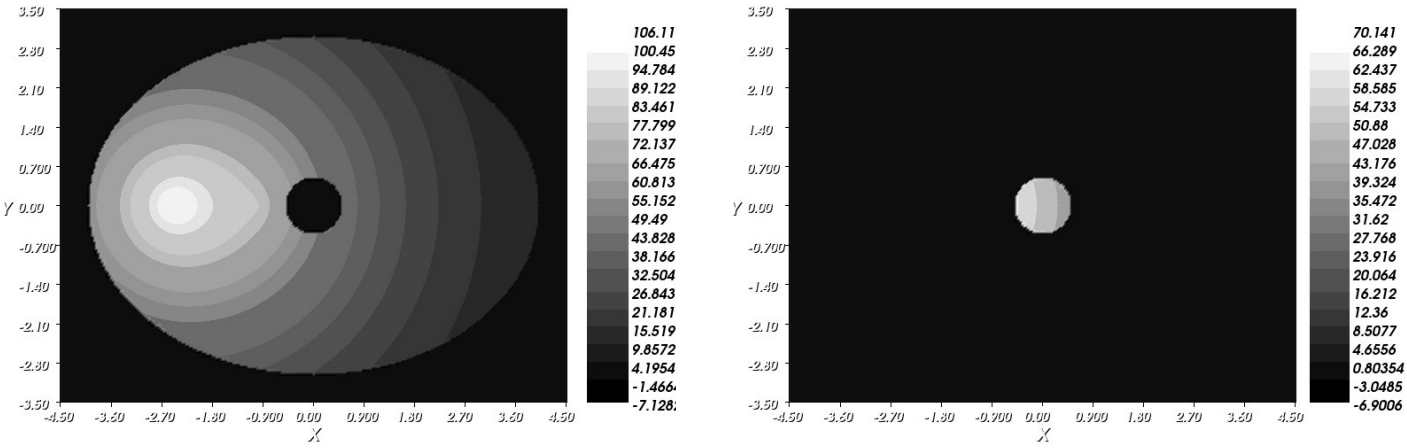

(a) The prostate (b) The urethra

Figure 4.12: Organ absorbed doses at $t = 0$ for a dose of $120Gy$.

The results of a treatment with a total dose of $120Gy$ and $80Gy$ are presented. The dose of $120Gy$ represents the minimum dose necessary to fully treat the initial considered tumor. The $80Gy$ dose represents a dose at which we can clearly observe a cancer relapse and therefore the dose to which we combine hormone therapy afterwards.

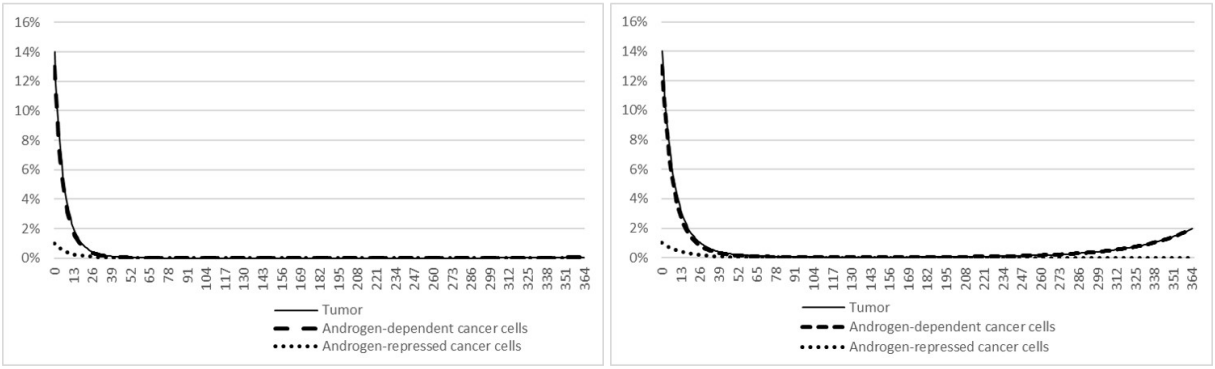

(a) Total dose of $120Gy$ (b) Total dose of $80Gy$

Figure 4.13: Cancer cells evolution under brachytherapy in percentage of the maximum cell carrying capacity of the prostate.

When comparing Figure 4.13 and Figure 4.9, brachytherapy is more effective than hormonal therapy since it allows to treat the tumor unlike hormonal therapy which, in the same time frame, allows at best to bound the tumor volume. And even in that case the bounded tumor volume is more important than that of the relapsed tumor with brachytherapy. However, brachytherapy does not spare healthy tissue as shown in Figure 4.14.

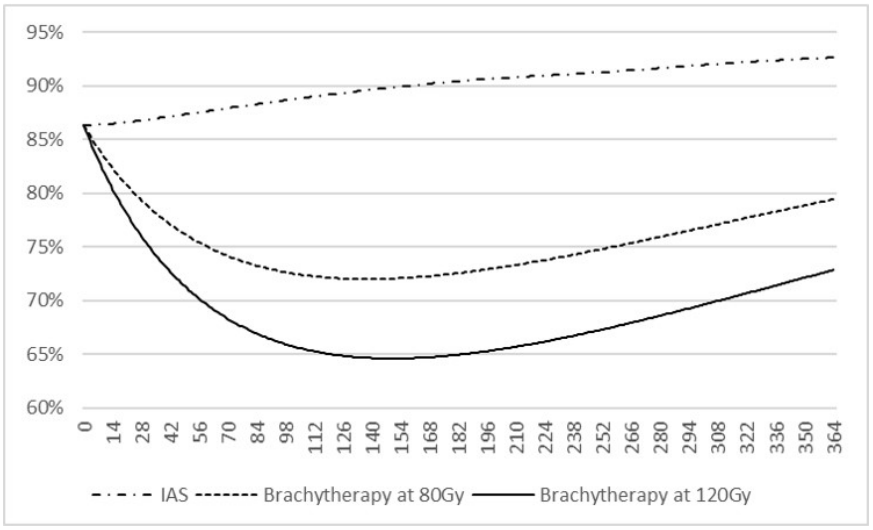

Figure 4.14: Evolution of healthy prostate cells in percentage of the maximum cell carrying capacity of the prostate in the case of different treatments.

During brachytherapy treatment, the loss in healthy tissue is more important than in hormone therapy. We notice the positive growth of the healthy cells when the radioactivity of the sources has almost disappeared and the tumor has been treated. By reducing the administered dose from $120Gy$ to $80Gy$, we can better preserve healthy cells. Nevertheless, the damage to healthy tissue remains significant compared to hormone therapy.

From a clinical point of view, brachytherapy is recommended when the tumor is localized. In this case, it treats fully the tumor. It represents the equivalent of surgery since it kills the cells, unlike hormone therapy which stops their proliferation and aims to control their growth. In our case, given the considered initial conditions, the results obtained are in good accordance with the reality.

Combined treatment simulations

In order to find the best way to combine hormone therapy with brachytherapy we investigate two aspects. First, the timetable of the combination, either by initiating both treatments simultaneously or by delaying the start of one therapy compared to the other. Second, the impact of the intensity of each treatment on the effectiveness of the combination, by using continuous or intermittent for hormone therapy and and by varying the dosage for brachytherapy.

Treatment schedule

The dose considered for brachytherapy is $80Gy$ for which we try to prevent the relapse or at least delay it by using a combined treatment. As hormone therapy has given better results in its intermittent version, we consider, at first, the combination of intermittent androgen deprivation therapy with a brachytherapy of $80Gy$.

In the first scenario, both therapies start simultaneously at ($t = 0$). As shown in Figure 4.15(a), the tumor relapse is delayed compared to the case where only $80Gy$ brachytherapy is used along with a much slower tumor regrowth. However, it is not enough to prevent the relapse of the disease. This is explained by the fact that the hormone therapy switched off at an early stage (after 13 days of treatment according to Figure 4.15(b)) and did not reactivate afterwards. In fact, at the beginning of the treatment, the curves for brachytherapy alone and in combination almost overlap except for a slightly more rapid decrease in tumor volume in the case of combined treatment, the brachytherapy dominates the hormone therapy and the resulting tumor volume does not allow the IAS to resume. To remedy this, a second scenario where the start of brachytherapy is delayed compared to that of hormone therapy was studied. In the case where only IAS was administered, the hormone therapy needed 26 days for the PSA level to fall below the PSA threshold to switch off the treatment (see Figure 4.10(b)). Therefore, for the second scenario, initially only the IAS is delivered at (t=0). Brachytherapy is then activated after 26 days at $80Gy$. In this case the treatments are not simultaneous but occur one after the other: androgen deprivation therapy first then brachytherapy. Figure 4.15(a) shows that this combination leads to a slower decrease of the tumor volume at the begining but better result in fine.

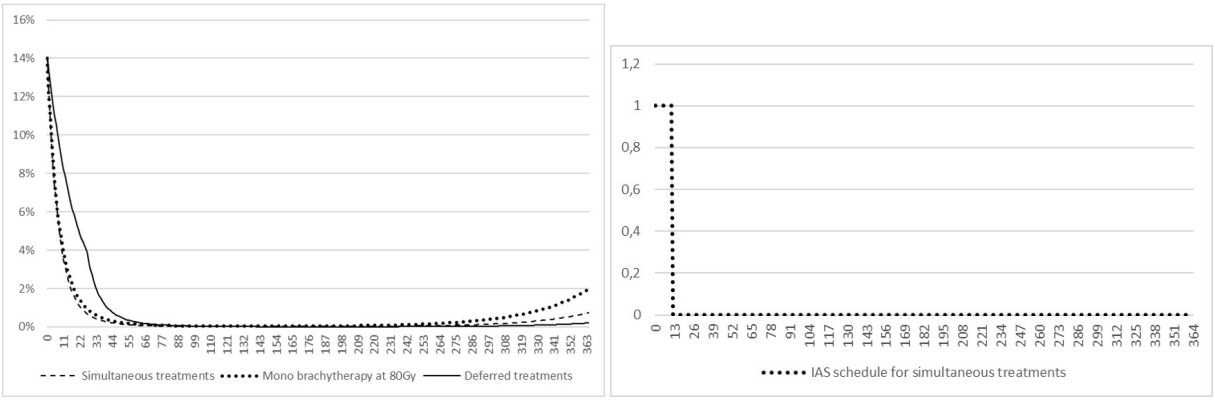

(a) (b)

Figure 4.15: Different combining schedules: (a) Tumor evolution in percentage of the maximum cell carrying capacity under different combining protocols of androgen deprivation therapy and brachytherapy, (b) IAS schedule in the simultaneous combined treatment.

Treatment intensity

To study the impact of the intensity of each therapy on the combination of treatments, we first replace the intermittent hormone therapy with its continuous version and combine it with brachytherapy to assess the impact of hormone therapy on the treatment combination. As shown in Figure 4.16, at the beginning of treatment, the two curves for brachytherapy with intermittent deprivation therapy and brachytherapy with continuous androgen deprivation overlap. At the end of the observation period, we note a slight reduction of the tumor volume due to the use of continuous deprivation instead of the intermittent one.

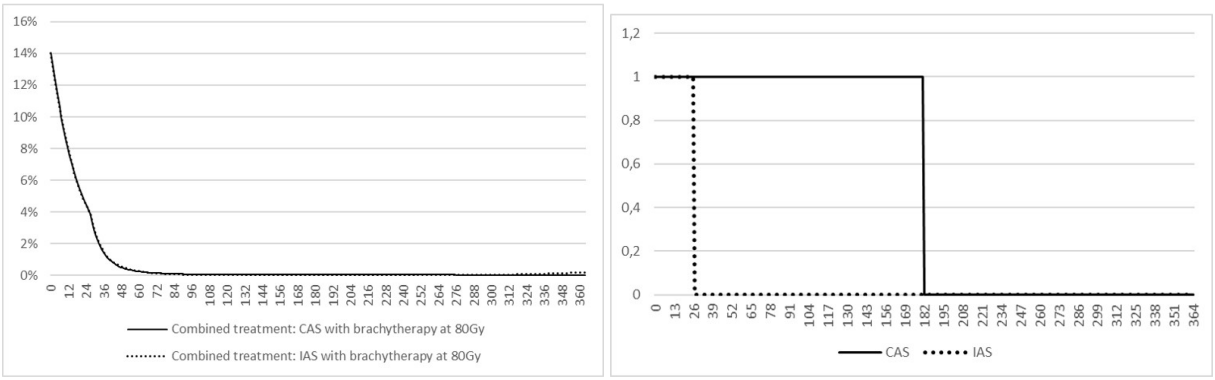

(a) (b)

Figure 4.16: Combined brachytherapy with both forms of hormone therapy: (a) Tumor evolution under brachytherapy at $80Gy$ combined with both forms of hormonal therapy in percentage of the maximum cell carrying capacity, (b) Androgen deprivation schedule in the case of a combined treatment of ADT therapy with brachytherapy at $80Gy$.

However, Figure 4.17 shows a significant loss in androgen due to CAS compared to the slight gain in tumor volume reduction. Using hormone therapy for nearly a month before stopping it and then switching to brachytherapy seems to be the best alternative.

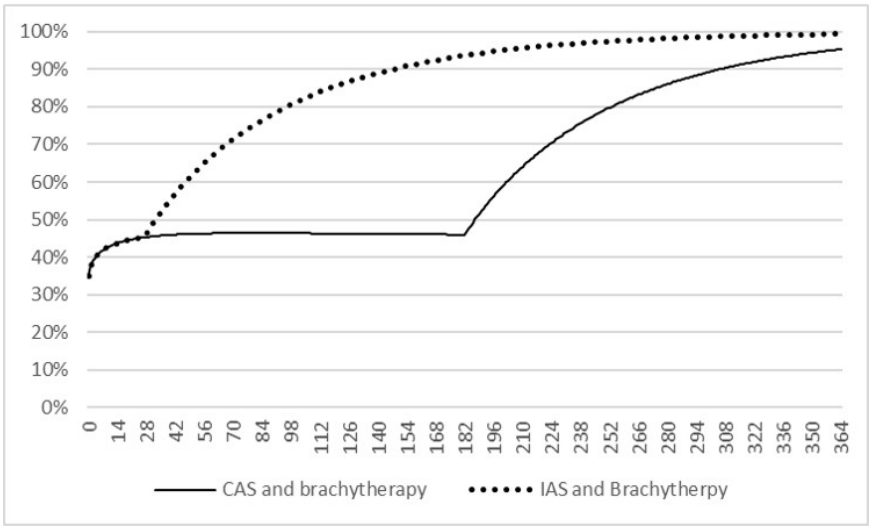

Figure 4.17: Androgen concentration evolution in percentage of the androgen saturation level A_0 for a combined treatment of brachytherapy at $80Gy$ with both hormonal therapy.

Secondly, we evaluate the impact of the dose used in brachytherapy on the effectiveness of the treatment. We first activate only the androgen deprivation therapy for 26 days before switching to brachytherapy at $80Gy$ for the first scenario and $70Gy$ for the second.

As shown in Figure 4.18, the graphs of the two scenarii are identical for the first 26 days when only hormone therapy is activated. Thereafter, a slightly slower decrease in tumor volume is observed for the scenario with a dose of $70Gy$. Furthermore, tumor relapse occurs earlier with a lower dose of brachytherapy. The radiation dose therefore plays an important role in the remission of the tumor.

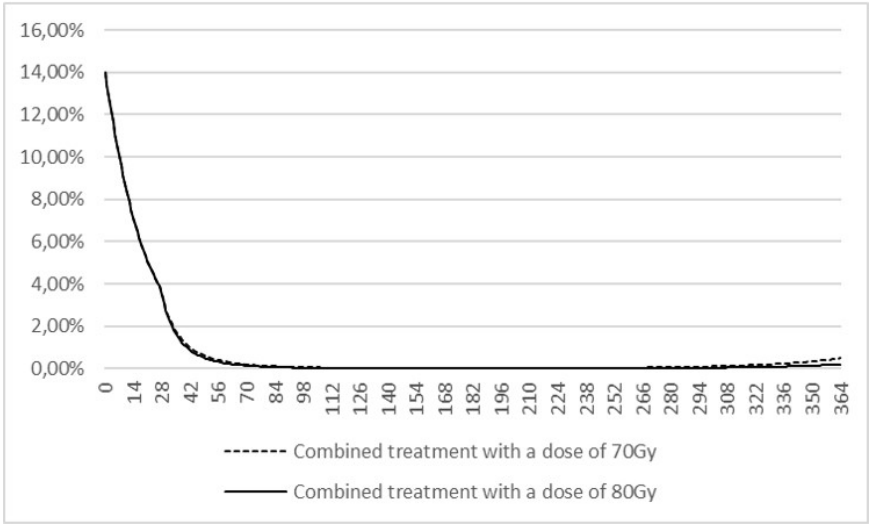

Figure 4.18: Tumor evolution in percentage of the maximum cell carrying capacity of the prostate under combined androgen deprivation therapy and brachytherapy.

Clinically, hormone therapy is combined with brachytherapy for advanced and metastatic cancers. Hormone therapy is then administered either at the same time than radiation therapy as initial treatment or before radiation therapy to reduce tumor volume and make the radiation treatment more effective. In our case, even if the tumor initially considered does not necessarily require a combined treatment, the latter allowed us to reduce the radiation dose as well as the androgen deprivation time and thus preserve the androgen level in the prostate.

4.6 Conclusion

Prostate cancer is a heterogeneous cancer with a good prognosis. The treatment is multimodal, most often combining radiotherapy and hormone therapy. Clinically, brachytherapy finds its interest in the localized stages and its role in the advanced stages remains complementary. Whereas, hormone therapy is of interest in the advanced stages. Hence the interest in developing new therapeutic strategies with the help of mathematical modeling to explore the role of hormone therapy in the early stages but also to improve its combination with brachytherapy depending on the progress of the disease. The most relevant strategies are: neoadjuvant hormone therapy to brachytherapy and the combination of hormone therapy and brachytherapy.
In this chapter, we developed a novel mathematical model for prostate cancer under hormone therapy and brachytherapy. The dynamics of the prostate cells helped us to write the partial differential equations describing the evolution of the different cell densities composing the prostate. Androgens are diffused in the prostate and act as a growth factor for androgen-dependent cancer cell. The first treatment implemented is the hormone therapy that affects the production of androgens in order to reduce the proliferation of the cells that depend on it. When we used continuous androgen suppression, the treatment became ineffective when the androgen-repressed cancer cells started proliferating and led to treatment failure. However, its intermittent form has given better results. While it did not treat the tumor, intermittent androgen suppression managed to control its volume. The second treatment implemented is internal radiotherapy for which we studied

the effect of different doses on the tumor. The effect of radiation on the healthy tissue of the prostate and on the organ at risk, the urethra, was also assessed. Our results show that, unlike hormone therapy, brachytherapy was able to treat the tumor.
Combining hormone therapy with brachytherapy allowed us to reduce the dose used from 120Gy to 80Gy. When the treatments are given at the same time, the final tumor volume is significantly reduced compared to using each therapy separately. However, starting with hormone therapy gave better results. When using intermittent hormone therapy combined with brachytherapy, we found that once the PSA level drops below the critical level, it stays at reasonable levels and therefore the hormone therapy does not reactivate. When we use continuous hormone therapy instead, the prostate is unnecessarily deprived of androgen for an almost non-existent reduction in tumor volume compared to intermittent deprivation. The use of hormone therapy over a short period of time is therefore sufficient to give good results. The results also showed that the dose used in the combined treatments affects the tumor relapse. The model we presented in this chapter is a first attempt to model and study the combination of hormone therapy with brachytherapy for prostate cancer. As discussed with clinicians, it would be interesting to investigate different initial tumor conditions.

In the next chapter, we discuss a second biomathematical problem that arose from the global context faced in 2019. The pandemic due to the coronavirus 2019 disease led scientists and especially biomathematicians to research this disease in order to better understand it and assist governments in controlling its spread. As a PhD student in biomathematics I had the opportunity to work on the subject and include it in my thesis work.

Chapter 5

Coronavirus ABM modeling and simulation

Abstract

In this chapter we implement an epidemiological model using agent-based modeling to simulate the spread of the corona virus diseases that appeared in 2019 (Covid-19). The model discussed in this chapter is based on the compartmental SLIAR model. The main goal is to study the impact and relevance of different sanitary measures taken by the Moroccan authorities to contain the pandemic and reduce its spread. The agent-based numerical simulations a carried out in Netlogo and several scenarios on the spread of the virus are presented.

5.1 Introduction

A virus, which means "poison" in Latin, is a biological agent incapable of multiplying on its own and depends on a host cell to do so. The virion is the infectious particle of the virus. The coronaviruses are a group of RNA viruses that can cause symptoms ranging from mild (as common colds) to lethal (as acute respiratory tract infections). Their virions have a spherical form with club-shaped spikes projecting from their surface shaping them as a solar corona (Latin word for "crown") earning them the name of coronavirus see Figure 5.1. The coronaviruses (CoV) infect mammals and birds and have a high mutation rate. Tyrell and Bynoe described the first human coronavirus cultivated from patients with common colds in 1966 [107], but the first coronavirus described was cultivated from chicken embryos in 1937 [108]. Since then several coronaviruses have been discovered in different animals and were divided in four categories: $\alpha-$, $\beta-$,$\gamma-$ and $\delta-$CoV. The first two gather the coronaviruses of mammalian origin and the other two the coronaviruses of avian origin [107, 108].

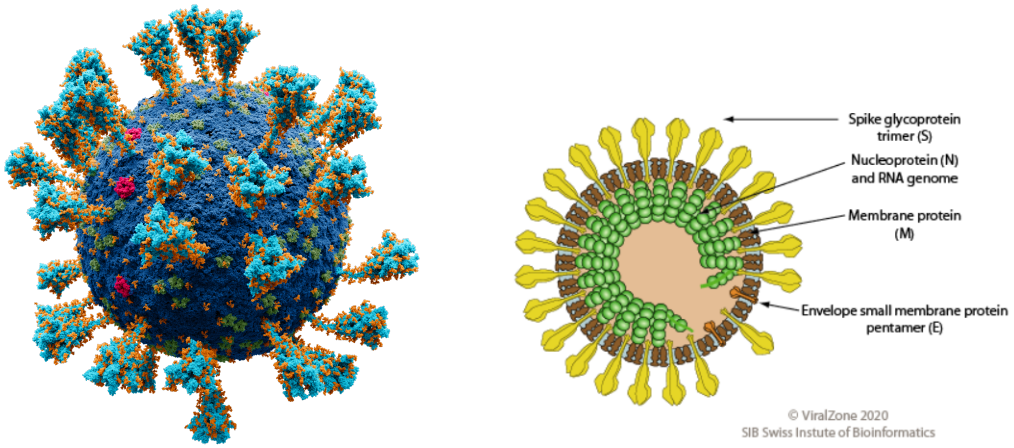

(a) Covid-19 virion by Solodovnikov A., Arkhipova V. et al. published in (https://nplus1.ru/).

(b) Covid-19 virion components by ViralZone, SIB Swiss Institute of Bioinformatics.

Figure 5.1: Coronavirus virion.

The largest variety of mutations of this virus originated in bats and spread to an intermediate animal like the himalayan palm civet for Severe Acute Respiratory Syndrome Coronavirus (SARS-CoV) and the dromedary camel for the Middle East respiratory syndrome Coronavirus (MERS-CoV), before spreading to humans [108].
On December 2019, China reported a cluster of patients with pneumonia in Wuhan hospitals. A new variant of the $\beta-$CoV was then identified and named "Severe Acute Respiratory Syndrome Coronavirus 2" (SARS-CoV-2) or "Coronavirus disease 2019" (Covid-19) [109]. This new virus shares 96.2% of the properties of bat CoV RaTG13 and 79.5% of the properties of the SARS-CoV responsible for the 2002-2003 epidemic [108]. It is characterized by a high transmission rate and a relatively low lethal rate of 1.2% of the total discovered cases as of May 2022, which is a lower rate than the MERS-CoV lethal rate of 34.4% and the SARS-CoV death rate of 9.19% [109]. Covid-19 can be transmitted by direct contact with an infected person in the vicinity or by indirect contact with objects or surfaces previously contaminated by an infected person.

Symptoms due to Covid-19 may differ from one individual to another. The most common ones according to WHO are fever, cough, fatigue and loss of taste or smell but also sore throat and/or headache, body aches and diarrhea. The most severe symptoms observed include difficulty breathing or shortness of breath, loss of speech, difficulty moving or confusion and thoracic pain.

The high transmission rate of this new virus made the WHO classify Covid-19 disease as a pandemic in March 2020 and the governments of different countries adopted several sanitary measures in order to contain its spread. The mathematical modeling of this novel coronavirus provides, with the help of compartmental models and different simulated scenarios, a basis for reflection on the different measures taken by authorities and, eventually, an epidemiological surveillance tool for the monitoring of the sanitary crisis caused by Covid-19.
In the next section, we describe and implement a variation of the SLIAR agent-based model for the modeling and simulation of Covid-19 developed within the CNRST research project entitled "Mathematical Modeling and Artificial Intelligence for the Analysis of the evolution of the Coronavirus pandemic in Morocco".

5.2 SLIAR model for Covid-19 spread

Mathematical modeling of infectious diseases is a valuable decision-support tool in handling an epidemic outbreak. It allows the analysis and monitoring of the epidemic spread according to the sanitary actions undertaken (quarantine, screening, vaccination etc.) in order to establish the appropriate measures to be taken for a better management of the epidemic. The modeling process is achieved by using compartmental models which are based on two key elements:

- The compartments that represent the different states of the population where individuals from the same compartment share the same behavior.
- The rules that govern the crossing from one compartment to another. They define the rate at which each state ends and thus allow to evaluate the fraction of each compartment that will proceed to the next one (that is: the next state).

The disease caused by Covid-19 is characterized by an incubation period where the individual infected by the virus does not show any symptoms. In addition, Covid-19 symptoms may not occur throughout the course of the infection. An individual contaminated by the virus therefore goes through an incubation period after which he or she will either develop the symptoms of the disease or remain a healthy but infectious carrier of the virus. The compartmental model SLIAR allows to take into account all those states through which an individual infected by the Covid-19 goes.
The population is compartmentalized into five states of individuals: The Susceptible compartement (S) gathers the individuals at risk of contracting the disease, the Latent compartement (L) contains the individuals in incubation period, the Infected one (I) the symptomatic individuals who have developed Covid-19 symptoms, the Asymptomatic one (A) the healthy but infectious carriers of the virus and the Removed compartment (R) accounts for the dead and the recovered individuals.

In [63] Julien Arino and Stéphanie Portet proposed a modified SLIAR model better suited to diseases with a latent period and symptomatic and asymptomatic outbreaks. In fact, since the time horizon of the simulations is quite short compared to the incubation and infection periods estimations, a better modeling of the sojourn times in those critical compartments is essential. In this case, the Erlang distribution better describes the transmission rates from one compartment to another than the exponential distribution usually used in epidemiology. It "allows both a less pronounced early end and a less extended duration of the incubation period" as explained by Arino and Portet in [63]. Given that the Erlang distribution is the distribution of the sum of $(k > 1)$ independent exponential variables, Arino and Portet proposed in [63] a modified SLIAR model. Choosing $(k = 2)$, they replaced the L, I and A compartments, each, by two compartments for a better modeling of the Covid-19 compartmental model transition rates and therefore a better modeling of the incubation and infection periods characterizing this disease. Figure 5.2 illustrates the diagram of the resulting $SL_1L_2I_1I_2A_1A_2R$ model from which the ODE system governing the propagation of Covid-19 in [63] is obtained.

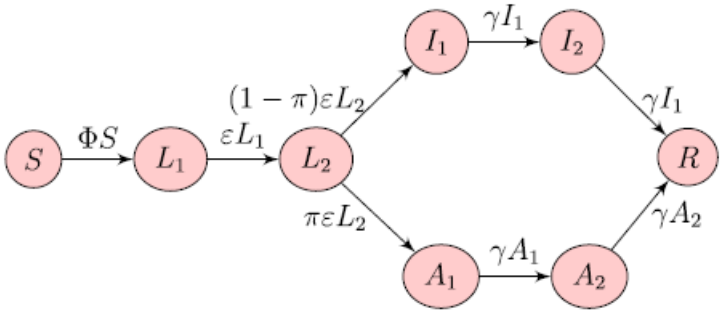

Figure 5.2: $SL_1L_2I_1I_2A_1A_2R$ compartmental model flowchart [63].

where:

- Φ is the force of infection that measures the infection probability.
- ε is the rate at which incubation ends such as by properties of Erlang distributions, the average incubation period is $2/\varepsilon$ time unit.
- π is the fraction of the infected who are asymptomatic.
- γ is the rate at which the infection period ends such as by properties of Erlang distributions, the average infectious time is $2/\gamma$.

As part of the CNRST research program, we used the modified SLIAR model to simulate the spread of Covid-19 in Morocco using a multi-agent approach. The simulated results were compared to the ODE approach presented by Arino and Portet and applied to the Moroccan case study.

5.3 Agent-based model

Agent-based models are used to simulate the actions and interactions of different agents in order to recreate and predict the evolution of complex phenomena. The behavior of the agents is governed by a set of rules derived from the phenomenon characteristics. Agent-based models are thus based on populations and rules, two key elements that also describe the compartmental models. Hence the relevance of using an agent-based approach for epidemic and pandemic modeling.

The model features all the states an individual infected with Covid-19 can go through as illustrated in Figure 5.2 such as each individual is represented by an agent. To calculate the fraction of individuals that transits at each moment from one compartment to another, the ODE approach requires the transition rates (ε and γ) computed from the average times spent in the latent and infectious (symptomatic or asymptomatic) states. In our model, the incubation and infection periods are used directly as input parameters to define the time spent by each agent in each state. In addition, statistical analysis showed that incubation and infection times due to Covid-19 follow a log-normal distribution [50, 110, 111]. Therefore, instead of using the average value of incubation and infection times for the whole population, each agent has its own characteristic times calculated from log-normal distributions.
The infectiousness of a person contaminated with Covid-19 can start before the end of his incubation period [63,112]. As a result, the L_1-state gathers the infected agents in incubation still not infectious while the L_2-state gathers the infectious agents in incubation with an attenuated but not neglected pathogenicity. Moreover, according to epidemiological and clinical data [113,114], the pathogenicity of an asymptomatic Covid-19 infected person is lower than that of a symptomatic one therefore the infectiousness of the asymptomatic agents is also attenuated. The developed agent-based model runs thus as follows.

Each agent has an incubation period $t_L \sim Log\mathcal{N}(\frac{2}{\varepsilon}, \sigma_L^2)$ and an infection period $t_I \sim Log\mathcal{N}(\frac{2}{\gamma}, \sigma_I^2)$ and at each time iteration:

- When there are no restrictions on their mobility, the agents move so as not to collide with other agents. Each agent inspects its surrounding to assess the distance between him and the other agents. If there is a risk of contact with another individual, the agent moves in the opposite direction of the individual he is likely to collide with. If not, the agent moves with a random direction.

- The infectious agents are those of the latent-infectious, symptomatic and asymptomatic compartments.

- A susceptible agent has a probability β of being contaminated upon contact with an infectious agent.

  a) In the case of contact with a latent-infectious agent, β is attenuated with a coefficient η.

  b) In the case of contact with an asymptomatic agent, β is attenuated with a coefficient ξ.

- Upon infection, a susceptible agent enters the latent-non-infectious state for a period of $(t_L/2)$ before reaching the latent-infectious state.

- After $(t_L/2)$ in the latent-infectious state, the agent becomes :
  a) a symptomatic agent with a probability $(1 - \pi)$
  b) an asymptomatic agent with a probability π
- A symptomatic (respectively asymptomatic) agent spends a period of t_I in the symptomatic (respectively asymptomatic) compartments before reaching the R-compartment.

In epidemiology, the main indicator of the dynamics of the spread of an epidemic is its reproduction rate. The basic reproduction number R_0 measures the potential for transmission of a disease in a population where all individuals are susceptible to infection. It represents the average expected number of secondary infections an infectious person would cause in the population. A basic reproduction number of θ means that we expect each new infection to cause θ cases of secondary infections.
In our model, at each iteration, we calculate the effective reproduction number R_t which is the average number of secondary cases per infectious agent in the population made up of both susceptible and non-susceptible agents.

$$R_t = \frac{\text{Number of new infections at iteration t}}{\text{Total number of infectious agents at iteration (t - 1)}} \tag{5.1}$$

Such that $R_t > 1$ indicates that the number of cases are on the rise and that the disease will spread quickly in the population and reciprocally. The higher the value of R_t, the more difficult it is to control the disease.

Our goal, through this model, is to evaluate the impact of different sanitary measures taken by governments to control Covid-19 spread, namely :

- **Preventive measures** like social distancing, mouth and nose covering, hand washing and surface cleaning.
- **Partial lockdown** of population where only a small percentage of the population was allowed to circulate through derogatory authorizations.
- **Restrictions on travel** and migration where flows of individuals can enter the population through migration rates "b_L", "b_A" and "b_I" that are explained and justified further on.

The outputs of our model to assess the dynamic of the spread are the following curves:

- The "**Active cases**" curve for the total number of infection cases at each time step.
- The "**Cumulative infected and recovered**" curve for the total percentage of infected and recovered.
- The "**Daily-new-cases-vs-Daily-new-recoveries**" curve for the number of daily new infected people and the number of daily recovered people.
- The "$\mathbf{R}_t$" curve for the estimation of the effective reproduction number at each time step.

The user interface on Netlogo for our model is shown in Figure 5.3.

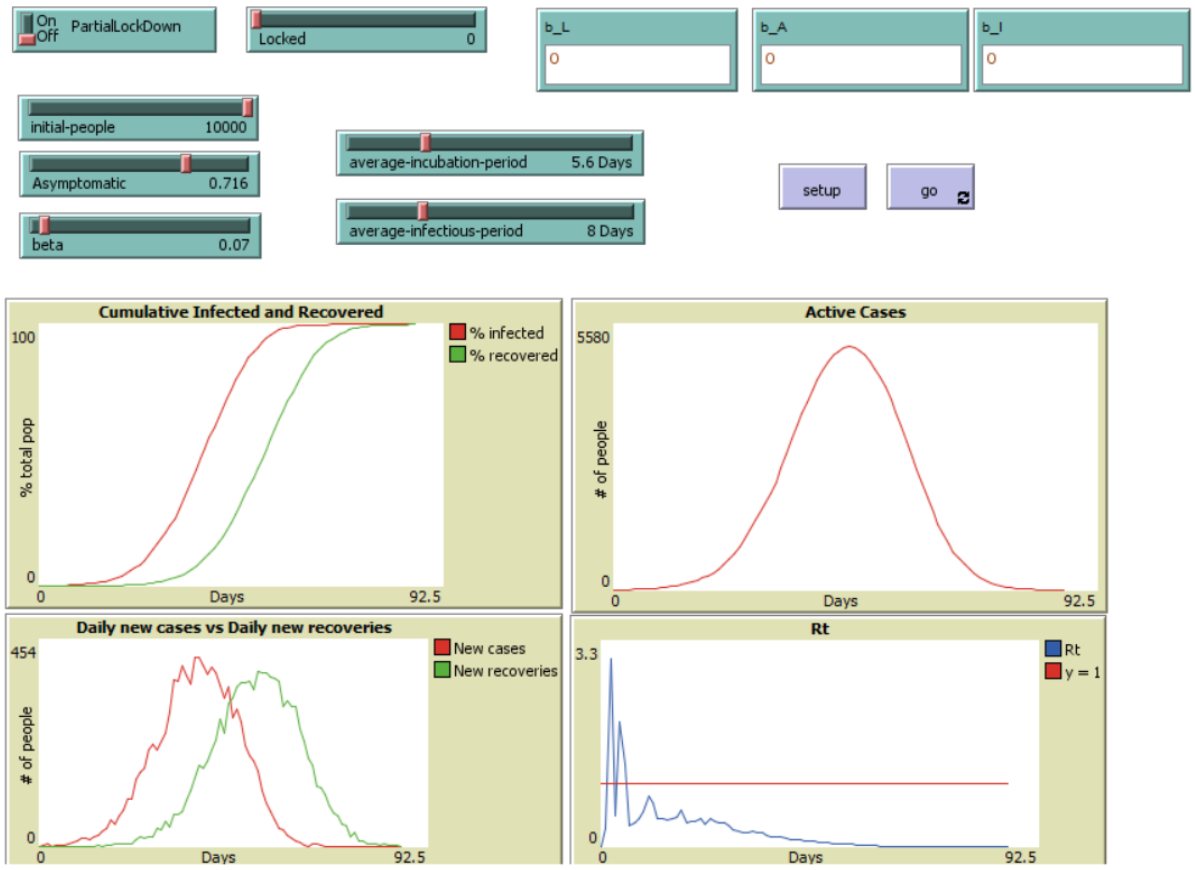

Figure 5.3: User interface on Netlogo for the Covid-19 agent-based model. The "Partial-LockDown" switch enables to activate the lockdown of the population with a fraction of "Locked" individuals. The slider "initial-people" sets the sample size of the population. The slider "Asymptomatic" sets the fraction of asymptomatic cases in the population. The slider "beta" sets the probability of infection β upon contact with the virus. The slider "average-incubation-period" sets the mean value of the incubation period distribution. The slider "average-infectious-period" sets the mean value of the infection period distribution. The inputs "b_L", "b_A" and "b_I" sets the migration rates into the latent, asymptomatic and symptomatic compartments respectively. The button "setup" sets up the model. The button "go" launches the simulation and the different outputs curves are progressively drawn throughout the simulation.

5.4 Numerical simulations: Moroccan case

In order to contain the Covid-19 spread in Morocco, the government set up a variety of policies, as did other governments. In this section, we investigate the relevance and the impact of some of those policies with the help of different scenarios.
In the first three scenarios, the population is considered closed and migration rates are equal to zero ($b_L = b_A = b_I = 0$). The first scenario represents the theoretical case in which Morocco would not have initiated any measures at the onset of Covid-19 cases in its territory and the disease followed its natural course in the population sample under study. The second scenario consolidates the effect of the preventive measures (social distancing, mask wearing, hand washing and surface cleaning) on Covid-19 spread. The third scenario, the effect of partial lockdown and the fourth one the impact of the travel and migration ban. The size of the sample population is 10^4 agents of which two are from the I_1 compartment and the rest susceptibles. The mean and standard deviation of the distribution of the incubation and infection periods are derived from statistical studies and given in Table 5.1.
For the Moroccan data, the Directorate of Epidemiology and Control of Diseases of the Moroccan Ministry of Health reported, in its "Epidemiological Bulletin COVID-19 $N°7$ of 17/06/2020", that the proportion of asymptomatic forms in Morocco is at ($\pi = 71.6\%$). Also, the Moroccan High Commission for Planning estimated, in its report "Covid-19 pandemic in a national context", that thanks to the preventive measures swiftly put in place by the government shortly after the first Covid-19 cases were identified in Morocco in March 2020, the probability of being infected upon contact with a Covid-19 infected person in Morocco is ($\beta = 0.04$). It also estimated that without the preventive measures this probability would have been of ($\beta = 0.05$).

Table 5.1: Incubation and infection periods distributions for Covid-19 outbreak.

Parameter	*Distribution*	*Mean* (*days*)	*STD* (*days*)	*Source*
t_L	Log-normal	5.6	2.8	[110]
t_I	Log-normal	8.0	2.0	[111]

Scenario 1: Covid-19 natural evolution $\beta = 0.05$

In this scenario, we consider that no restrictions are put in place to prevent the propagation of Covid-19 in Morocco. The simulations outputs are presented in Figure 5.4.
In this scenario, R_t reaches a maximum of 2 which means that the disease is spreading very quickly. The epidemic ends after 111 days with 100% of the sample population infected and a peak of 4188 active cases after 60 days. In addition, there is a time delay between infection and recovered curves that disadvantages the health sector and may cause its overload.

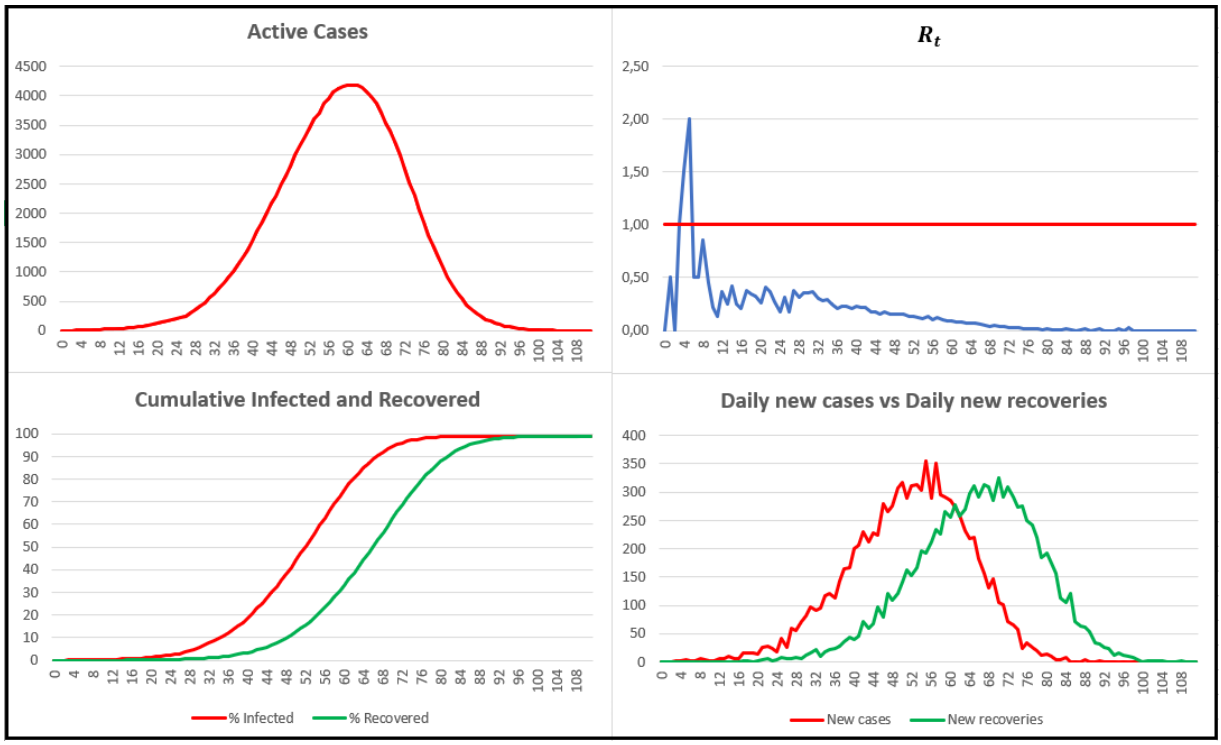

Figure 5.4: First scenario "Covid-19 natural evolution" outputs.

Scenario 2: Preventive measures $\beta = 0.04$

In this scenario, we simulate the preventive mesures impact on Covid-19 spread in Morocco. The probability of infection upon contact with the virus is reduced by 20% thanks to these measures. The simulations outputs are presented in Figure 5.5.
In this scenario, R_t reaches a maximum of 1.5 which means that the preventive measures have reduced the spread of the disease but not enough to slow down its progression. The epidemic ends after 139 days with 97.3% of the sample population infected and a peak of 3606 active cases after 60 days. Preventive measures have reduced the peak of infections, which should alleviate the burden on the health care system. We also note that the gap between the curves for the recovered and the infected is reduced compared to the first scenario. The evolution of the recovered individuals is more in line with that of the infected individuals, which will allow the hospitals to better manage their resources.
In the following, the preventive measures are maintained in the next scenarios.

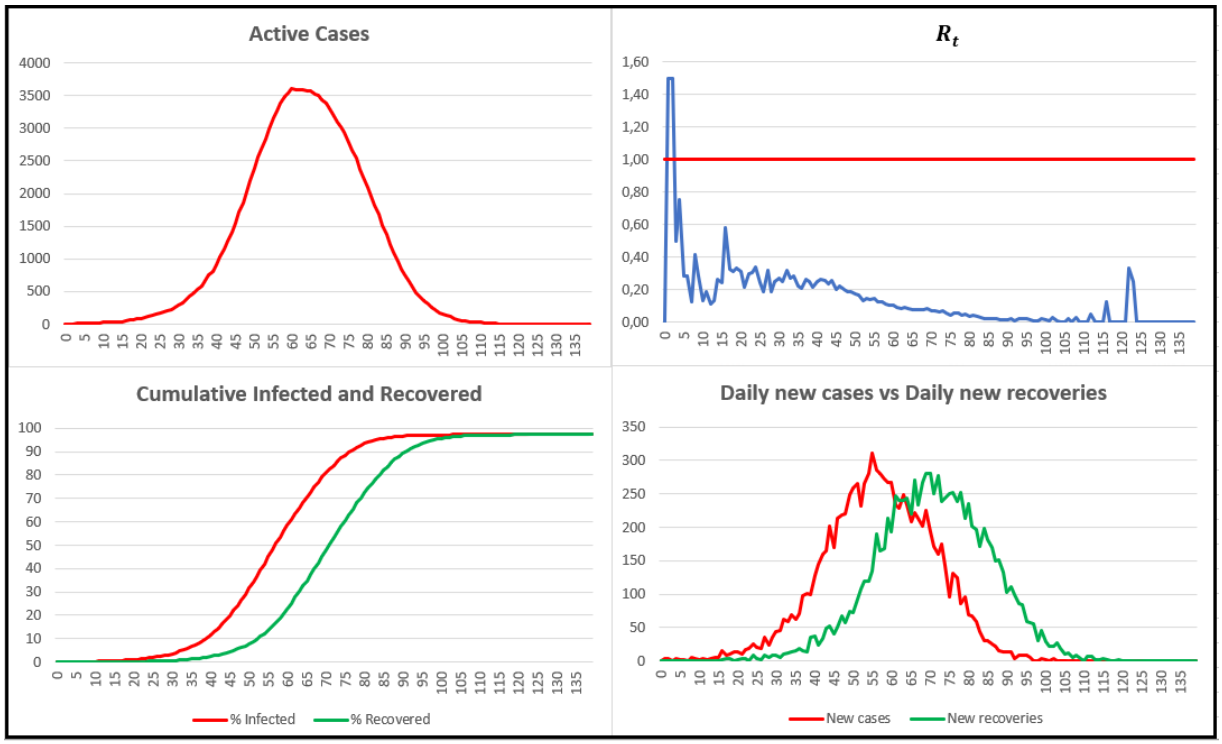

Figure 5.5: Second scenario "Preventive measures" outputs.

Scenario 3: Partial lockdown with preventive measures

In this scenario, we suppose that only 20% of the population is allowed to circulate because of the government enforced lockdown. This percentage represents the different cases where an exceptional exemption has been issued. The simulations outputs are presented in Figure 5.6. In this scenario, R_t reaches a maximum of 1 which means that the partial lockdown with preventive measures have slowed down significantly the spread of the disease. The maximum number of active cases has decreased considerably. The epidemic ends after 373 days with 96.7% of the population infected and reaches a maximum of 687 active cases after 181 days. The distribution of active cases is no longer bell-shaped. The incidences are more distributed in time and the curves of the infected and recovered are almost overlapped.

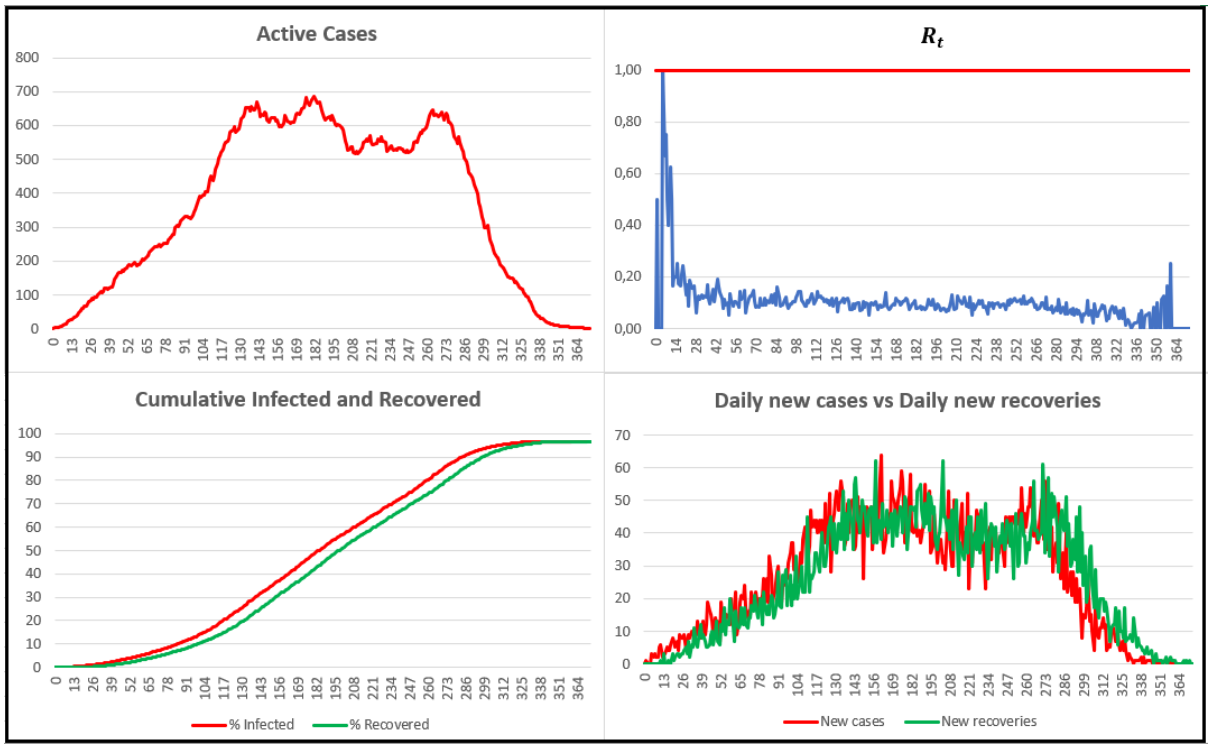

Figure 5.6: Third scenario "Partial lockdown with preventive measures" outputs.

Scenario 4: Restrictions on travel

During the Covid-19 health crisis, Morocco as well as several countries decided to close their borders to travelers and/or ban inter-city travel to limit the spread of the virus. The scenarios studied above fall into this case where the population is closed. These travel restrictions are starting to get relaxed. In this fourth scenario, we study the case of an opened population where migration of individuals is allowed. We are interested in modeling the migration of infected individuals into the population. Although Morocco imposes screening tests on travelers to enter its territory, the test may give a false negative result either because the viral load is not yet detectable or because the test was performed incorrectly. We therefore assume that each compartment of infected individuals has a positive migration rate: b_L for latents compartments, b_I for symptomatic ones and b_A for asymptomatic ones. Since symptomatic individuals are easier to detect than asymptomatic and incubating cases, we consider that $b_I < b_L$ and $b_I < b_A$. The flowchart of the model incorporating migration is presented in Figure 5.7. The outputs of this scenario where migration is allowed while maintaining the preventive measures are presented in Figure 5.8. The simulations are run with $b_I = 0.001$ and $b_L = b_A = 0.005$.

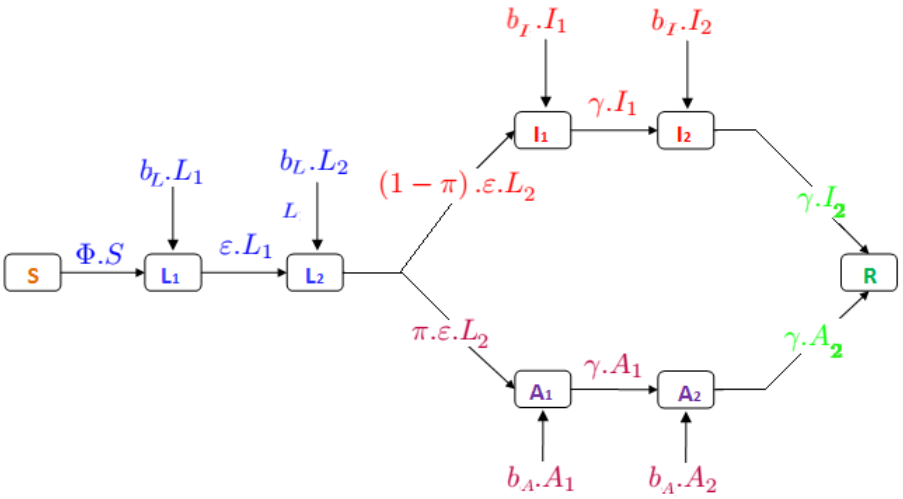

Figure 5.7: Model flowchart including migration.

In this scenario, R_t reaches a maximum of 2 which means that the disease is spreading rapidly. The maximum number of active cases reaches its highest value amongst the four scenarios studied. The epidemic ends after 116 days with 100% of the opened population infected and a peak of 4596 active cases after 64 days. Even if the preventive measures are in place, the effective reproduction number reaches a higher level than in the second scenario, which means that the epidemiological situation has deteriorated compared to the scenario with the preventive measures. Figure 5.9 and Table 5.2 summarize a comparison of the results of the different scenarios.

Table 5.2: Summary of some results of the different Covid-19 scenarios.

Scenario	Natural evolution	Preventive measures	Partial lockdown	Migration
R_t peak	2	1.5	1	2
Max active cases	4188	3606	687	4596
Outbreak duration	111 days	139 days	373 days	116 days

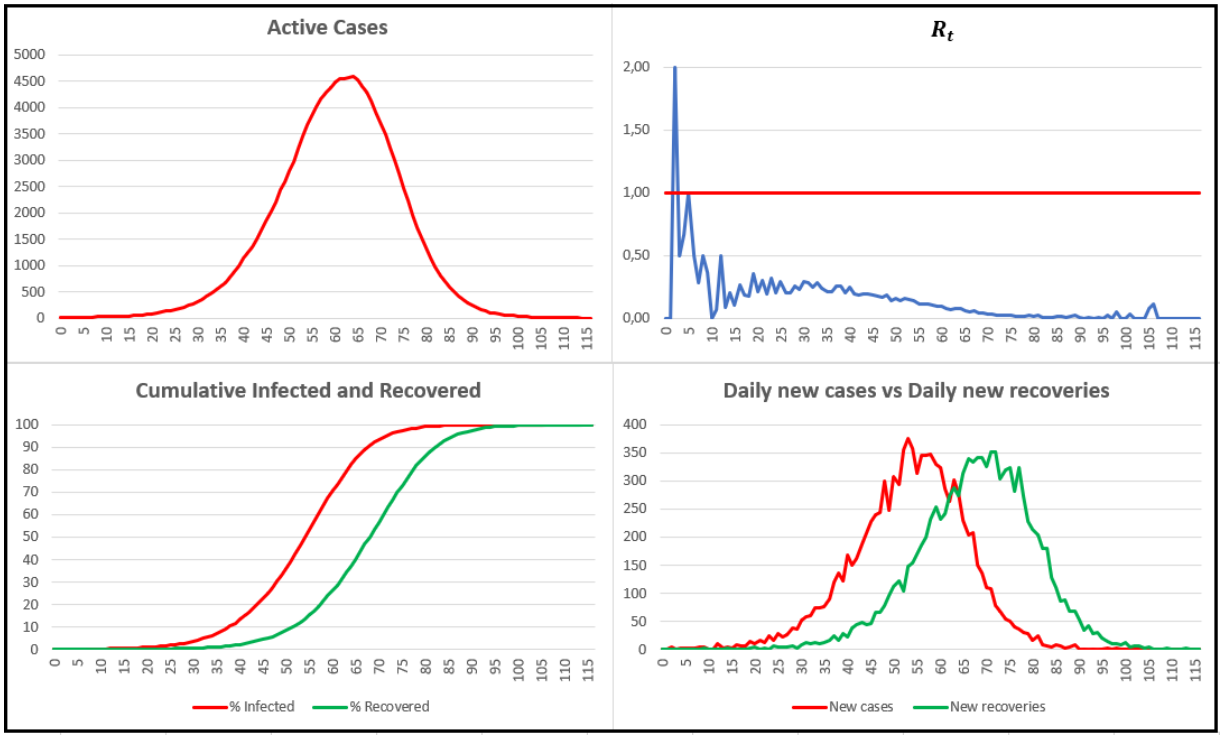

Figure 5.8: Fourth scenario "Migration allowed" outputs.

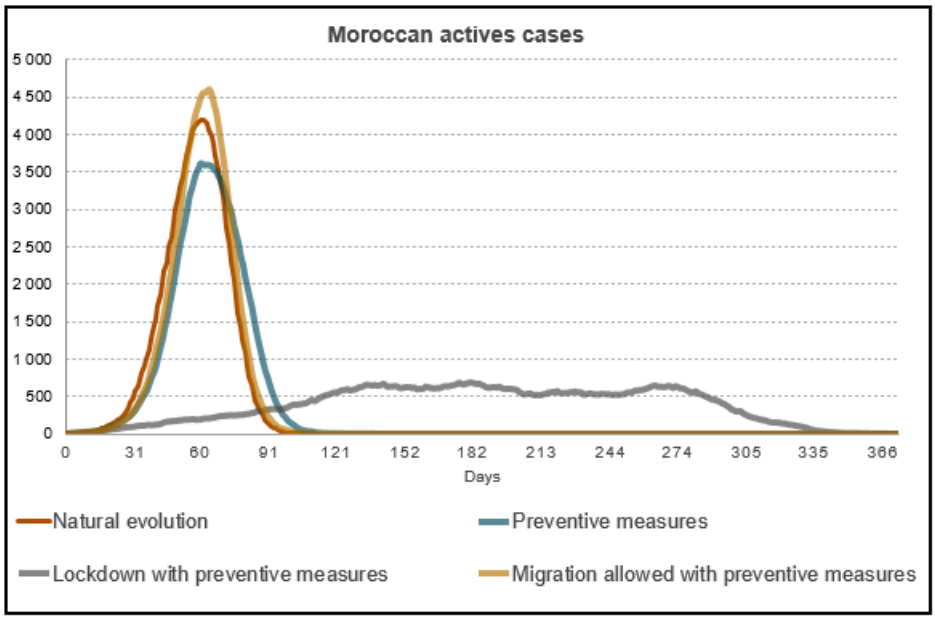

Figure 5.9: Summary of the evolution of active cases under different policies.

5.5 Conclusion

In this chapter, we developed a decision support tool for monitoring and controlling an epidemic outbreak. The model implemented allows to simulate the spread of infectious diseases characterized by an incubation period and the emergence of asymptomatic cases. The proposed tool allows to study the effect of three sanitary measures on the spread of the virus: the preventive measures, population lockdown (partial or total) and the restrictions on people migration. Furthermore, the user interface is intuitive and offers the possibility to combine different sanitary measures and to adjust their parameters such as the fraction of the population confined or the migration rates. It can also be used for other infectious diseases by adjusting the incubation and infection periods. In order to validate our agent-based model, we compared the results of the natural evolution scenario and the migration scenario with those of the ODE approach developed within the CNRST project and presented in [115] and [116] respectively. The output curves of the two approaches have the same shape and the simulations results in both cases led to the same analysis and conclusions. The agent-based approach enables to follow the evolution of the infection at the individual level as opposed to the ODE approach that allows to understand how the epidemic evolves in the whole population. Moreover, multi-agent modeling takes into account the mobility of individuals within the compartments, and illustrates it quantitatively, which allowed us to implement the lockdown measure and evaluate its impact on the epidemic.
The analysis of the different scenarios showed that sanitary measures slowed down the spread of the virus, with varying degrees of efficiency from one measure to another. Population lockdown gave the best result in terms of epidemic peaks and propagation pace, but the time required to reach the collective immunity in this scenario is very long. In addition, because Covid-19 is a new disease, information about this virus is constantly changing. Therefore, with new informations, partial lockdown may not be the best scenario to control the disease.

Chapter 6

Conclusion and perspectives

The different models developed in this thesis aim to provide specialists and decision-makers with decision support tools in the health field. The first topic we discussed in this work is cancer. Cancer is a complex disease that involves a large number of parameters. The models published in the literature aim to simulate tumor growth each by emphasizing some of these parameters or a specific tumor-related mechanism. The bibliography in this field is therefore vast and diversified and mathematical modeling using partial differential equations takes the lead in terms of published papers. We were especially interested in the work of Sethian J. A. [66, 67, 117] who used the level-set method in different PDE approaches to simulate the shape of a cancerous tumor. In [117], the PDE model is more complex and models the vascularization of the tumor as well. In [67], the model is simplified and tumor growth is modeled according to the evolution of the nutrient concentration inside the tumor as well as the pressure inside the domain occupied by the tumor. The level-set method in both approaches relied on Darcy's law to compute the normal velocity of the tumor deformation. We were interested in using the level-set method with Darcy's velocity to simulate the shape of a tumor modeled with a different PDE system. We based our PDE model on that of Lagaert J. B. in [2], where a standard mass balance law leads to the reaction-convection equation for each of the tumoral tissue cell densities namely the proliferative cells, the healthy cells and the necrotic ones. We then modeled the diffusion of the oxygen concentration in the tumor tissue as the nutrient that defines the cell densities dynamics and used Sethian's level-set method with Darcy's velocity to simulate the tumor shape. This first approach led to our first results in tumor modeling. We next sought to calculate the normal velocity of the level-set function by a second method to have a basis for comparison with Darcy's approach. The paper by Allaire G. et al. provides in [68] an implementation of the level-set method where the front velocity is computed using the shape derivative of the classical shape optimization method. To our knowledge, there were no publications that used that methodology in tumor growth modeling. We have therefore adapted the shape optimization approach to fit our model and used it as a second approach for the macroscopic modeling of tumor growth. Starting from an initial spherical shape, Darcy velocity gave a distorted tumor shape evolution while the shape optimization kept the tumor in its spherical form. The final tumor size was also different between the two approaches, that of the shape optimization was more important. In terms of computational time, the shape optimization approach costs three times more in CPU time. We discussed the achieved results with clinicians, but from a medical standpoint the model parameters, namely the cells proliferative and death rates, that define the dynamics of the cells don't

have a straightforward equivalence in the clinical field and the results of both approaches could be a possible evolution of an untreated tumor. The PDE linear model in chapter 2 could be extended in many directions: taking into account non-linearities (such as logistic growth models) or mechanobiological processes (such as viscoelastic behavior of cells). However, while there is no difficulty in extending theoretically the PDE approach, this would tremendously increase the computational costs. The PDE model can also be extended to take into account the effect of medical treatment on the tumor development. Two approaches can be considered, either by adding a PDE that describes the diffusion of the drug concentration to the the PDE system "Eq. (2.11)", or by adjusting the proliferative cell PDE "Eq. (2.4)" to take into account the cell death due to the treatment [43].

We wanted to explore different ways of modeling tumor growth. The second type of tumor growth models found in the literature is based on agent-based simulations for a microscopic approach at the cellular level. A hybrid model combining agent-based modeling for the cell's behavior and a PDE for the diffusion of the oxygen in the cell's environment is an approach that is not as widespread as the macroscopic approach or the purely agent-based approach. Besides, it provides a more easily assimilated tool for clinicians. Agent-based models also provide an easier way to model cell behavior. For that, we just need to describe the different cell behaviors in the instructions given to the agents. The more detailed the description, the more realistic the model is while still maintaining the same computational time. Which is not the case for the PDE approach used in chapter 2. The hybrid model presented in chapter 3, like the two approaches from chapter 2, illustrated an increasing size over time for an untreated tumor. The sensitivity analysis of the hybrid model allowed a more thorough investigation of the model's behavior. The simulations showed that without treatment, the tumor expands over time and as the divisions and mutation rates of the cells increase, the tumor's cancer cell population increases as well leading to a more compact tumor. The hybrid model can be extended by adding new biological rules to the agents to enrich their behavior with additional characteristics of the cancer disease, adding a treatment for the tumor can also be considered. For example, we can include the cell's biological aging and division mode and use them as a guideline for applying the treatment or we can add an additional PDE to describe the diffusion of the treatment in the tumor environment. The hybrid model can also be extended to simulate angiogenesis by adding blood vessels as a new type of agent and use them to determine the location and timing of the treatment depending on the tumor vasculature.

The goal behind modeling and numerical simulation, whether through mathematical or agent-based models, is on the one hand to better understand complex problems and on the other hand to provide a solution to these problems. As previously explained, both the macroscopic and microscopic approaches presented in chapter 2 and 3, can be extended to take into account therapeutical strategies. However, both models cover the case of cancer globally. Depending on where the cancer develops, certain treatments may be more appropriate than others. In addition, each type of cancer has its own characteristics. It would therefore be interesting to study a specific type of cancer and investigate its therapeutic strategies. We chose prostate cancer because, to our knowledge, there is no published mathematical study on the combination of hormone therapy and brachytherapy for prostate cancer although this combination of treatments is used in the clinical setting. We discussed the protocols of the two treatments, the requirements for their pre-

scription and their clinical results with oncologists and in chapter 3, we confirmed using mathematical modeling, that hormone therapy helps at best to control the tumor volume and alone it does not cure prostate cancer. We also confirmed that brachytherapy alone is enough to cure a localized prostate tumor and that in combination, brachytherapy dominates hormone therapy. In the initial setting presented in chapter 3, the best way to combine hormone therapy with brachytherapy is to start with hormonotherapy first for almost a month then switch to brachytherapy. This combination allows to reduce the radiation dose used and also helps to preserve the prostate androgen supply that hormone therapy would normally deplete leading to some side effects that are difficult to accept by patients. Clinicians were initially skeptical about using hormone therapy for a localized tumor. But, as discussed, the initial conditions can be adapted to study more developed tumors and we first wanted to validate our model with a simple initial tumor setting. Moreover, the role of mathematical modeling is to explore new therapeutic strategies. Since the model yielded good initial results, we can now consider more complex initial conditions and seek to optimize the combination of the two treatments. The initial conditions considered in chapter 3, represent the case where brachytherapy alone can treat the tumor and hormone therapy alone is not routinely used. The placement of the radioactive sources is therefore intuitive and simple since the tumor is located on one lobe of the prostate. The model could be extended to take into consideration the optimization of the seeds locations in order to minimize the dose absorbed by the organs at risk while minimizing the tumor volume. In the case presented here, we found that we do not need to optimize the treatment schedule of hormone therapy when used in combination. However, by changing the initial conditions and considering a more advanced stage of the tumor, hormone therapy could play a more important role and therefore also require an optimization of its parameters.

The second topic we studied emerged naturally in the global context experienced since the end of 2019. The Covid-19 caused a pandemic that urged governments to try their best in containing its spread. The decision support tool presented in chapter 5 allows to study the impact of the sanitary measures taken by governments on the outbreak. We used the developed tool to study the case of Morocco. We found that partial lockdown of the population gave the best results. It has significantly slowed down the rate of progression of the virus as well as reduced the number of active cases on a daily basis. However, when we developed the model, the immunity acquired after a Covid-19 infection was presumed definitive. It turns out that the infection only confers a temporary immunity of a few months. In this new setting, the partial lockdown of the population may not be the best way to control the disease. The model can therefore be extended to take into account all new findings related to this new virus. In particular, the fact that the immunity acquired in the R-compartment after a contamination is temporary. An agent recovered from Covid-19 therefore re-enters the susceptible compartment after a certain period of time. The model can also be extended to take into account the development of vaccines that also confer temporary immunity to a susceptible individual without having to go through an infection.

Bibliography

[1] Weinberg R. A., How cancer arises, *Scientific American.* **275**:62–70, 1996.

[2] Lagaert J. B., Modélisation de la croissance tumorale: Estimation de paramètres d'un modèle de croissance et introduction d'un modèle spécifique aux gliomes de tout grade,*Thèse de doctorat. Université Sciences et Technologies-Bordeaux I.*pp. 15–62, 2011.

[3] Roose T., Chapman S. J., Maini P. K., Mathematical models of avascular tumor growth, *SIAM review.* **49**:179–208, 2007.

[4] Sleeman B. D., Levine H. A., Partial differential equations of chemotaxis and angiogenesis, *Mathematical methods in the applied sciences.* **24**:405–426, 2001.

[5] Chaplain M. A. J., McDougall S. R., Anderson A. R. A., Mathematical modeling of tumor-induced angiogenesis, *Annual Review of Biomedical Engineering.* **8**:233–257, 2006.

[6] Orme M. E., Chaplain M. A. J, A mathematical model of vascular tumour growth and invasion, *Mathematical and Computer Modelling.* **23**:43–60, 1996.

[7] Breward C. J. W., Byrne H. M., Lewis C. E., A multiphase model describing vascular tumour growth, *Bulletin of mathematical biology.* **65**:609–640, 2003.

[8] Wise S. M., Lowengrub J. S., Frieboes H. B. et al., Three-dimensional multispecies nonlinear tumor growth—I: model and numerical method, *Journal of theoretical biology.* **253**:524–543, 2008.

[9] Xu J., Vilanova G., Gomez H., A mathematical model coupling tumor growth and angiogenesis, *Plos One.* Vol. 11, 2016.

[10] Frieboes H. B., Jin F., Chuang Y. L. et al., Three-dimensional multispecies nonlinear tumor growth—II: tumor invasion and angiogenesis, *Journal of theoretical biology.* **264**:1254–1278, 2010.

[11] Macklin P., McDougall S., Anderson A. R. A. et al., Multiscale modelling and nonlinear simulation of vascular tumour growth, *Journal of mathematical biology.* **58**:765–798, 2009.

[12] Folkman J., The role of angiogenesis in tumor growth, *Seminars in cancer biology*, Vol. 3, pp. 65–71, 1992.

[13] Folkman J., Angiogenesis, *Biology of endothelial cells*, pp. 412—428, Springer, 1984.

[14] McDougall S. R., Anderson A. R. A., Chaplain M. A. J. et al., Mathematical modelling of flow through vascular networks: implications for tumour-induced angiogenesis and chemotherapy strategies, *Bulletin of mathematical biology.* **64**:673–702, 2002.

[15] McDougall S. R., Anderson A. R. A., Chaplain M. A. J., Mathematical modelling of dynamic adaptive tumour-induced angiogenesis: clinical implications and therapeutic targeting strategies, *Journal of theoretical biology.* **241**:564–589, 2006.

[16] Billy F., Ribba B., Saut O. et al., A pharmacologically based multiscale mathematical model of angiogenesis and its use in investigating the efficacy of a new cancer treatment strategy, *Journal of theoretical biology.* **260**:545–562, 2009.

[17] Folkman J., Angiogenesis, *Annual Review of Medicine.* **57**:1–18, 2006.

[18] Michel T., Fehrenbach J., Lobjois V. et al., Mathematical modeling of the proliferation gradient in multicellular tumor spheroids, *Journal of Theoretical Biology.* **458**:133–147, 2018.

[19] Knopoff D. A., Fernández D. R., Torres G. A. et al., Adjoint method for a tumor growth PDE-constrained optimization problem, *Computers and Mathematics with Applications.* **66**:1104–1119, 2013.

[20] De Angelis E., Preziosi L., Advection-diffusion models for solid tumour evolution in vivo and related free boundary problem, *Mathematical Models and Methods in Applied Sciences.* **10**:379–407, 2000.

[21] Friedman A., Cancer as Multifaceted Disease, *Mathematical Modelling of Natural Phenomena.* **7**: 3–28, 2012.

[22] Zhang Y., He Y., Chen H., Boundary element method for a free boundary problem modeling three dimensional tumor growth, *Computers & Mathematics with Applications.* **73**:1627–1641, 2017.

[23] Friedman A., Reitich F., Symmetry-breaking bifurcation of analytic solutions to free boundary problems: an application to a model of tumor growth, *Transactions of the American Mathematical Society.* **353**:1587–1634, 2001.

[24] Friedman A., Reitich F., Analysis of a mathematical model for the growth of tumors, *Journal of mathematical biology.* **38**:262–284, 1999.

[25] Huang Y., Zhang Z., Hu B., Bifurcation for a free-boundary tumor model with angiogenesis, *Nonlinear Analysis: Real World Applications.* **35**:483–502, 2017.

[26] Friedman A., Lam K. Y., Analysis of a free-boundary tumor model with angiogenesis, *Journal of Differential Equations.* **259**:7636–7661, 2015.

[27] Friedman A., Hu B., Asymptotic stability for a free boundary problem arising in a tumor model, *Journal of Differential Equations.* **227**:598–639, 2006.

[28] Knopoff D. A., Fernández D. R., Torres G. A. et al., Adjoint method for a tumor growth PDE-constrained optimization problem, *Computers & Mathematics with Applications.* **66**:1104–1119, 2013.

[29] Agnelli J. P., Padra C., Turner C. V., Shape optimization for tumor location, *Computers & Mathematics with Applications.* **62**:4068–4081, 2011.

[30] Konukoglu E., Clatz O., Menze B. H. et al., Image guided personalization of reaction-diffusion type tumor growth models using modified anisotropic eikonal equations, *IEEE transactions on medical imaging.* **29**:77–95, 2009.

[31] Olsen M., Siegelmann H. T., Multiscale agent-based model of tumor angiogenesis, *Procedia Computer Science.* **18**:1016–1025, 2013.

[32] Zhang L., Wang Z., Sagotsky J. A. et al., Multiscale agent-based cancer modeling, *Journal of mathematical biology.* **58**:545–559, 2009.

[33] Sabzpoushan S. H., Pourhasanzade F., A new method for shrinking tumor based on microenvironmental factors: Introducing a stochastic agent-based model of avascular tumor growth, *Physica A: Statistical Mechanics and its Applications.* **508**:771–787, 2018.

[34] Rejniak K. A., Anderson A. R. A., Hybrid models of tumor growth, *Wiley Interdisciplinary Reviews: Systems Biology and Medicine.* **3**:115–125, 2011.

[35] Ribba B., Alarcón T., Marron K. et al., The use of hybrid cellular automaton models for improving cancer therapy, *International Conference on Cellular Automata* , pp. 444–453, Springer, 2004.

[36] Kim Y., Stolarska M. A., Othmer H. G., A hybrid model for tumor spheroid growth in vitro I: theoretical development and early results, *Mathematical Models and Methods in Applied Sciences.* **17**:1773–1798, 2007.

[37] Alarcón T., Byrne H. M., Maini P. K., A cellular automaton model for tumour growth in inhomogeneous environment, *Journal of theoretical biology.* **225**:257–274, 2003.

[38] Mallet D. G., De Pillis L. G., A cellular automata model of tumor–immune system interactions, *Journal of theoretical biology.* **239**:334–350, 2006.

[39] Schaller G., Meyer-Hermann M., Multicellular tumor spheroid in an off-lattice Voronoi-Delaunay cell model, *Physical Review E.* **71**.051910, 2005.

[40] Benzekry S., Lamont C., Barbolosi D. et al., Mathematical modeling of tumor–tumor distant interactions supports a systemic control of tumor growth, *Cancer research.* **77**:5183–5193, 2017.

[41] Pouchol C., Clairambault J., Lorz A. et al., Asymptotic analysis and optimal control of an integro-differential system modelling healthy and cancer cells exposed to chemotherapy, *Journal de Mathématiques Pures et Appliquées.* **116**:268–308, 2018.

[42] Liu J.un, Wang X. S., Numerical optimal control of a size-structured PDE model for metastatic cancer treatment, *Mathematical biosciences.* **314**:28–42, 2019.

[43] Elazab A., Anter A. M., Bai H. et al., An optimized generic cerebral tumor growth modeling framework by coupling biomechanical and diffusive models with treatment effects, *Applied Soft Computing.* **80**:617–627, 2019.

[44] Sachs R. K., Hlatky L. R., Hahnfeldt P., Simple ODE models of tumor growth and anti-angiogenic or radiation treatment, *Mathematical and Computer Modelling.* **33**:1297–1305, 2001.

[45] Bray F., Ferlay J., Soerjomataram I. et al., Global cancer statistics 2018: GLOBOCAN estimates of incidence and mortality worldwide for 36 cancers in 185 countries, *CA: a cancer journal for clinicians.* **68**:394–424, 2018.

[46] Miyamoto H., Messing E. M, Chang C., Androgen deprivation therapy for prostate cancer: current status and future prospects, *The Prostate.* **61**:332–353, 2004.

[47] Petronio C. L. S., Paulo V. C. B., Helder S. L. et all., COVID-ABS: An agent-based model of COVID-19 epidemic to simulate health and economic effects of social distancing interventions, *Chaos Solitons & Fractals.* **139**:110088, 2020.

[48] Efthimios K., Georgios N., Multiple Epidemic Wave Model of the COVID-19 Pandemic: Modeling Study, *Journal of medical Internet research.* **22**,7 ,2020.

[49] Yaroslav V., Mykhailo M., Miroslav S. et all., Modeling and analysis of different scenarios for the spread of COVID-19 by using the modified multi-agent systems – Evidence from the selected countries, *Results in Physics.* **20**, 2021.

[50] Bouchnita A., Jebrane A., A hybrid multi-scale model of COVID-19 transmission dynamics to assess the potential of non-pharmaceutical interventions, *Chaos Solitons & Fractals.* **138**, 2020.

[51] Cooper I., Mondal A., Antonopoulos C. G., A SIR model assumption for the spread of COVID-19 in different communities, *Chaos, Solitons & Fractals.* **139**:110057, 2020.

[52] Calafiore G. C., Novara C., and Corrado P., A modified SIR model for the COVID-19 contagion in Italy, *59th IEEE Conference on Decision and Control (CDC).* 2020.

[53] Chen Y. C., Lu P. E., Chang C. S. et al., A time-dependent SIR model for COVID-19 with undetectable infected persons, *IEEE Transactions on Network Science and Engineering.* **7**:3279–3294, 2020.

[54] Sharov K. S., Creating and applying SIR modified compartmental model for calculation of COVID-19 lockdown efficiency, *Chaos, Solitons & Fractals.* **141**, 2020.

[55] Moein S., Nickaeen N., Roointa, A. et al., Inefficiency of SIR models in forecasting COVID-19 epidemic: a case study of Isfahan, *Scientific Reports.* **11**:1–9, 2021.

[56] Sharma S., Volpert V., Banerjee M., Extended SEIQR type model for COVID-19 epidemic and data analysis, *medRxiv.* 2020.

[57] Dashtbali M., Mirzaie M., A compartmental model that predicts the effect of social distancing and vaccination on controlling COVID-19, *Scientific Reports.* **11**:1–11, 2021.

[58] Arino J., Portet S., A simple model for COVID-19, *Infectious Disease Modelling.* **5**:309–315, 2020.

[59] Niu R., Wong E. W., Chan Y. C. et al., Modeling the COVID-19 pandemic using an SEIHR model with human migration, *IEEE Access.* **8**:195503–195514, 2020.

[60] Batistela C. M., Correa D. P., Bueno A. M. et al., SIRSi compartmental model for COVID-19 pandemic with immunity loss, *Chaos, Solitons & Fractals.* **142**:110388, 2021.

[61] Chen M., Li M., Hao Y. et al., The introduction of population migration to SEIAR for COVID-19 epidemic modeling with an efficient intervention strategy, *Information Fusion.* **64**:252–258, 2020.

[62] Sirkeci I., and Yucesahin M. M., Coronavirus and migration: analysis of human mobility and the spread of Covid-19, *Migration Letters.* **17**:379–398, 2020.

[63] Arino J., Portet S., A simple model for COVID-19, *Infectious Disease Modelling.* **5**:309–315, 2020.

[64] Meijer L., Le cycle de division cellulaire et sa régulation, *Oncologie.* **5**:311–326, 2003.

[65] Ambrosi D., Preziosi L., On the closure of mass balance models for tumor growth, *Mathematical Models and Methods in Applied Sciences.* **12**:737–754, 2002.

[66] Sethian J. A., Weigmann A., Structural boundary design via level set and immersed interface methods, *Journal of Computational Physics.* **163**:489–528, 2000.

[67] Cosmina S. H., Bruce T. M., Sethian J. A., Implementation of the level set method for continuum mechanics based tumor growth models, *Fluid Dynamics & Materials Processing.* **1**:109–130, 2005.

[68] Allaire G., Jouve F., Toader A. M., Structural optimization using sensitivity analysis and a level-set method, *Journal of Computational Physics.* **194**:363–393, 2004.

[69] Bouchon F., Peichl G. H., Sayeh M. et al., A free boundary problem for the Stokes equations,*ESAIM: Control, Optimisation and Calculus of Variations.* **23**:195–215, 2017.

[70] Hecht F., New development in FreeFem++,*Journal of numerical mathematics.* **20**:251–265, 2012.

[71] Hecht F., Freefem++ manual (version 3.58-1), 2018. `http://www3.freefem.org/`.

[72] Brown M., Bowring E., Epstein S. et al., Applying multi-agent techniques to cancer modeling, *Proceedings of the 6th annual workshop on multiagent sequential decision making in uncertain domains (MSDM)*, pp. 8–15, 2011.

[73] Gerlee P., Anderson A. R. A., Modelling evolutionary cell behaviour using neural networks: application to tumour growth, *Biosystems.* **95**:166–174, 2009.

[74] Jain H. V., Clinton S. K., Bhinder A. et al., Mathematical modeling of prostate cancer progression in response to androgen ablation therapy, *Proceedings of the National Academy of Sciences.* **108**:19701–19706, 2011.

[75] Jackson T. L., A mathematical investigation of the multiple pathways to recurrent prostate cancer: comparison with experimental data, *Neoplasia.* **6**:697–704, 2004.

[76] Ideta A. M., Tanaka G., Takeuchi T. et al., A mathematical model of intermittent androgen suppression for prostate cancer, *Journal of nonlinear science.* **18**:593–614, 2008.

[77] Verry C., Traitement du cancer localisé de la prostate par curiethérapie: à propos de 200 patients traités de juillet 2001 à janvier 2011 au CHU de Grenoble, *Thèse de doctorat.* 2011.

[78] King M. T., Keyes M., Frank S. et al., Low dose rate brachytherapy for primary treatment of localized prostate cancer: A systemic review and executive summary of an evidence-based consensus statement, *Brachytherapy.* **20**:1114–1129, 2021.

[79] Sharifi N., Gulley J. L., Dahut W. L., Androgen deprivation therapy for prostate cancer, *Jama.* **294**:238–244, 2005.

[80] Portz T., Kuang Y., Nagy J. D., A clinical data validated mathematical model of prostate cancer growth under intermittent androgen suppression therapy, *Aip Advances.* **2**:011002, 2012.

[81] Eikenberry S. E., Nagy J. D., Kuang Y., The evolutionary impact of androgen levels on prostate cancer in a multi-scale mathematical model, *Biology direct.* **5**:1–28, 2010.

[82] Jain H. V., Friedman A., Modeling prostate cancer response to continuous versus intermittent androgen ablation therapy, *Discrete & Continuous Dynamical Systems-B.* **18**:945, 2013.

[83] Jones B., Dale R. G., Bleasdale C. et al., A mathematical model of intraluminal and intracavitary brachytherapy, *The British journal of radiology.* **67**:805–812, 1994.

[84] Friedman A., Jain H. V., A partial differential equation model of metastasized prostatic cancer, *Mathematical biosciences and engineering: MBE.* **10**:591–608, 2013.

[85] Wang J. Z., Huang Z., Lo S. S. et al., A generalized linear-quadratic model for radiosurgery, stereotactic body radiation therapy, and high–dose rate brachytherapy, *Science translational medicine.* **2**, 2010.

[86] Holm, A., Mathematical optimization of HDR brachytherapy, *PhD. Thesis.* 2013.

[87] Kanikowski M., Skowronek J., Kubaszewska M. et al., Permanent implants in treatment of prostate cancer, *Reports of Practical Oncology & Radiotherapy.* **13**:150–167, 2008.

[88] Yoshiyuki R., Yoshimi T., Chapter three - Directional Cell Migration: Regulation by Small G Proteins, Nectin-like Molecule-5, and Afadin, *International Review of Cell and Molecular Biology.* **287**:97–143, 2011.

[89] Anderson A. R. A., A hybrid mathematical model of solid tumour invasion: the importance of cell adhesion *Mathematical medicine and biology: a journal of the IMA.* **22**:163–186, 2005.

[90] Nguyen E., Yen T., Ford V. et al., Mathematical modeling of metastatic cancer migration through a remodeling extracellular matrix, *Processes.* **6**:58, 2018.

[91] Fritz M., Lima E. A., Nikolić V. et al., Local and nonlocal phase-field models of tumor growth and invasion due to ECM degradation, *Mathematical Models and Methods in Applied Sciences.* **29**: 2433–2468, 2019.

[92] Toma A., Mang A., Schuetz T. A. et al., A novel method for simulating the extracellular matrix in models of tumour growth, *Computational and mathematical methods in medicine.* 2012.

[93] Wong H. C., Tang W. C., Effects of ECM Degradation Rate, Adhesion, and Drag on Cell Migration in 3D, *5th Kuala Lumpur International Conference on Biomedical Engineering 2011.* pp:428–431, 2011.

[94] Tanaka G., Hirata Y., Goldenberg S. L. et al., Mathematical modelling of prostate cancer growth and its application to hormone therapy, *Philosophical Transactions of the Royal Society A: Mathematical, Physical and Engineering Sciences.* **368**:5029–5044, 2010.

[95] Jackson T. L., A mathematical model of prostate tumor growth and androgen-independent relapse, *Discrete & Continuous Dynamical Systems-B.* **4**:187, 2004.

[96] Pavel M., Renna M., Park S. J. et al., Contact inhibition controls cell survival and proliferation via YAP/TAZ-autophagy axis, *Nature communications.* **9**:1–18, 2018.

[97] Adhyam M., Gupta A. K., A review on the clinical utility of PSA in cancer prostate, *Indian journal of surgical oncology.* **3**:120–129, 2012.

[98] Attix F. H., Introduction to radiological physics and radiation dosimetry. 2008.

[99] Podgorsak E. B., Basic radiation physics, *Radiation oncology physics: a handbook for teachers and students. Vienna: IAEA.* **7**. 2005.

[100] Deloule S., Développement d'une méthode de caractérisation spectrale des faisceaux de photons d'énergies inférieures à 150 keV utilisés en dosimétrie, *Thèse de doctorat.* 2014.

[101] Dale R. G., The application of the linear-quadratic dose-effect equation to fractionated and protracted radiotherapy, *The British journal of radiology.* **58**:515–528, 1985.

[102] Mi H., Petitjean C., Dubray B. et al., Prediction of lung tumor evolution during radiotherapy in individual patients with PET, *IEEE transactions on medical imaging.* **33**:995–1003, 2014.

[103] Wang J. Z., Guerrero M. L., Allen X., How low is the α/β ratio for prostate cancer?, *International Journal of Radiation Oncology* Biology* Physics.* **55**:194–203, 2003.

[104] Sieminska L., Ferguson M., Zerda T. W. et al., Diffusion of steroids in porous sol-gel glass: application in slow drug delivery, *Journal of Sol-Gel Science and Technology.* **8**:1105–1109, 1997.

[105] Swanson K. R., True L. D., Lin D. W., A quantitative model for the dynamics of serum prostate-specific antigen as a marker for cancerous growth: an explanation for a medical anomaly, *The American journal of pathology.* **158**:2195–2199, 2001.

[106] Berges R. R., Vukanovic J., Epstein J. I. et al., Implication of cell kinetic changes during the progression of human prostatic cancer, *Clinical cancer research.* **1**:473–480, 1995.

[107] Velavan T. P., Meyer C. G., The COVID-19 epidemic, *Tropical medicine & international health.* **25**: 278, 2020.

[108] Ludwig S., Zarbock A., Coronaviruses and SARS-CoV-2: A Brief Overview, *Anesthesia and analgesia.* **131**: 93–96, 2020.

[109] Khanna R. C., Cicinelli M. V., Gilbert S. S. et al., COVID-19 pandemic: Lessons learned and future directions, *Indian journal of ophthalmology.* **68**: 703–710, 2020.

[110] Linton N. M., Kobayashi T., Yang Y. et al., Incubation period and other epidemiological characteristics of 2019 novel coronavirus infections with right truncation: a statistical analysis of publicly available case data, *Journal of clinical medicine.* **9**: 538, 2020.

[111] Kerr C. C., Stuart R. M., Mistry D. et al., Covasim: an agent-based model of COVID-19 dynamics and interventions, *PLOS Computational Biology.* **17**,2021.

[112] Tong Z. D., Tang A., Li K. F. et al., Potential presymptomatic transmission of SARS-CoV-2, zhejiang province, China, *Emerging Infectious Diseases.* **26**, 2020.

[113] Kawasuji H., Takegoshi Y., Kaneda M. et al., Transmissibility of COVID-19 depends on the viral load around onset in adult and symptomatic patients, *PloS one.* **15** 2020.

[114] Han M. S., Seong M. W., Kim N. et al., Viral RNA Load in Mildly Symptomatic and Asymptomatic Children with COVID-19, Seoul, South Korea, *Emerging infectious diseases.* **26**: 2497–2499, 2020.

[115] Aboulaich R., Bensaid K., Chabbar S. et al., Mathematical modeling and multiagents approach for the evolution of the Coronavirus pandemic, *IEEE International Conference on Technology Management.* pp:1–6, 2020.

[116] Chabbar S., Benmir M., EL Karkri J. et al., Modeling and simulation of the evolution of the corona virus pandemic in a context of migration, *Journal of Theoretical and Applied Information Technology.* **99** 2021.

[117] Hogea C. S., Murray B. T., Sethian J. A, Simulating complex tumor dynamics from avascular to vascular growth using a general level-set method, *Journal of mathematical biology.* **53**:86–134, 2006.

Webography

[w1] https://cancer.org/cancer/prostate-cancer/treating/hormone-therapy.html

[w2] https://arcagy.org/infocancer/localisations/cancers-masculins/cancer-prostate/traitements/le-traitement-hormonal.html/

[w3] https://pharmacomedicale.org/medicaments/par-specialites/item/agonistes-et-antagonistes-de-la-lh-rh

[w4] https://mayoclinic.org/tests-procedures/prostate-brachytherapy/about/pac-20384949

[w5] https://e-cancer.fr/Patients-et-proches/Les-cancers/Cancer-de-la-prostate/Curietherapie/Quel-deroulement

[w6] https://bkmedical.com/applications/prostate-brachytherapy-ultrasound/